T.R.
ONDOKUZ MAYIS UNIVERSITY
INSTITUTE OF GRADUATE STUDIES
DEPARTMENT OF NANOSCIENCE AND NANOTECHNOLOGY

SYNTHESIS AND PROPERTIES OF POLY(ETHYLENE OXIDE) BASED NANOCOMPOSITE ELECTROLYTES CONSISTING OF NANO-SIZED Mg-BDC METAL ORGANIC FRAMEWORK

Ph.D. Thesis

Ayşe ERCİYES

Chair of Department

Prof. Dr. Müberra ANDAÇ

SAMSUN

2021

THESIS APPROVAL

This doctoral thesis study under the name of "**Synthesis and Properties of Poly(Ethylene Oxide) Based Nanocomposite Electrolytes Consisting of Nano-Sized Mg-BDC Metal Organic Framework**" which is prepared and presented by **Ayşe ERCİYES** under the consultancy of **Prof. Dr. Müberra ANDAÇ**, is approved by unanimously vote / by a majority vote as Doctoral Thesis in Nanoscience and Nanotechnology Department at Ondokuz Mayıs University by beloved committee members on 13.7.2021.

	Title, Name/Surname University Department	**Signature**	**Conclusion**
Committee Chair	Prof. Dr. Engin BURGAZ Ondokuz Mayıs University Department of Metallurgy and Materials Engineering		☒Acceptance ☐Rejection
Committee Member	Prof. Dr. Müberra ANDAÇ Ondokuz Mayıs University Department of Chemistry		☒ Acceptance ☐ Rejection
Committee Member	Asst. Prof. Dr. Aydemir Güralp URAL Samsun University Department of Aerospace Engineering		☒ Acceptance ☐ Rejection
Committee Member	Assoc. Prof. Dr. Bekir DIZMAN Sabancı University, Faculty of Engineering and Natural Sciences		☒ Acceptance ☐ Rejection
Committee Member	Prof. Dr. Mehmet ASLANOĞLU Harran University Deparment of Chemistry		☒ Acceptance ☐ Rejection

This thesis was approved by the committee members whose names are written above and determined by the Institute Administrative Board.

APPROVAL

…/…/2021

Prof. Dr. Ali BOLAT

Director of Institute

DECLARATION OF COMPLIANCE WITH SCIENTIFIC ETHIC

I hereby declare and undertake that all the information given in this thesis is true and absolute which is prepared in conformity with the regulations for Ondokuz Mayıs University Institution of Science and Technology thesis writing rules, all instructions were referred to and kept on the right side of the laws according to scientific ethic during in the stage of production of information.

Signature

July 2021

Ayşe ERCİYES

DECLARATION OF THESIS ORIGINALITY REPORT

Thesis Title: Synthesis and Properties of Poly(Ethylene Oxide) based Nanocomposite Electrolytes Consisting of Nano-Sized Mg-BDC Metal Organic Framework

As a result of the originality report taken by me from the plagiarism detection program on 28/05/2021 for the thesis whose title is mentioned above, it was found as follows;

Similarity rate: 8%

Single resource rate: 1%

28/5/2021

Prof. Dr. Müberra ANDAÇ

ÖZET

NANO-BOYUTLU Mg-BDC METAL ORGANİK KAFES YAPI İÇEREN POLİ(ETİLEN OKSİT) NANOKOMPOZİT ELEKTROLİTLERİN SENTEZİ VE ÖZELLİKLERİ

Ayşe ERCİYES
Ondokuz Mayıs Üniversitesi
Lisansütü Eğitim Enstitüsü
Nanobilim ve Nanoteknoloji Anabilim Dalı
Doktora, Temmuz, 2021
Anabilim Dalı Başkanı: Prof. Dr. Müberra ANDAÇ

Lityum (Li) pil teknolojisindeki en son gelişmelere bakıldığında, geleneksel sıvı elektrolitin yerini katı polimer elektrolitler (SPE) almaya başlamıştır. Bu nedenle, SPE'lerin modern enerji teknolojisinde önemli bir yeri vardır. Bu tez çalışmasında, nano boyutlu magnezyum benzen dikarboksilik asit metal organik kafes yapı (MgBDC MOF), metal tuzlara ihtiyaç duymadan elektrokimyasal (EC) yöntem ile başarıyla sentezlenmiştir. Nano boyuttaki MgBDC'nin oluşumu yüksek derecede kristal fazı ve karakteristik yansıma pikleri ile X-ışını kırınımı (XRD) sonuçlarına göre doğrulanmıştır. Nanoboyutlu MgBDC kafes yapıların büyüklüğü-küresel şekli-pürüzsüz yapısı, bölgesel haritalama-spektrum analizi ve yüzey topografisi sırasıyla taramalı elektron mikroskobu (SEM), taramalı tünel elektron mikroskobu (STEM), enerji dağıtıcı x-ışını spektroskopisi (EDS) ve atomik kuvvet mikroskobu (AFM) ile belirlenmiştir. Nanoyapıların termal özellikleri, kimyasal yapıları ve yüzey alanı (m^2/g) sırasıyla termogravimetrik analiz (TGA), zayıflatılmış toplam reflektans fourier dönüşümlü-kızıl ötesi (ATR FT-IR) spektroskopisi ve brunauer emmett teller (BET) analizleri ile belirlenmiştir. MgBDC MOF'tan oluşan nanokompozit polimer elektrolitler (NCPE'ler) çözelti döküm yöntemiyle başarıyla hazırlanmıştır. Polietilen oksit-lityum bis (triflorometan) sülfonimid (PEO-LiTFSI) elektrolit matrisi içerisinde nanoboyutlu MgBDC MOF'un homojen dağılımı ve kimyasal elementlerinin varlığı SEM/EDS ile incelenmiştir. XRD ve diferansiyel taramalı kalorimetri (DSC) verilerine dayanarak, nano boyutlu MgBDC MOF'un PEO-LiTFSI tuz sistemine dahil edilmesine bağlı olarak PEO'nun yüzde kristallik derecesi ve kristal faz yapısını %70'ten yaklaşık %20'ye düşürmüştür. Ayrıca polimer elektrolitlerde kristal yapı oluşumları polarize optik mikroskopi (POM) ile belirlenmiştir. Lityum tuzundaki katyonlar ile PEO zincirlerindeki eter-oksijen molekülleri arasındaki etkileşimler ATR FT-IR spektroskopi çalışmaları ile doğrulanmıştır. TGA sonuçlarına göre, NCPE'lerin termal dayanımı iyileştirilmiştir. NCPE membranların iyonik iletkenlikleri, çeşitli sıcaklık aralıklarında elektrokimyasal empedans spektroskopisi (EIS) kullanılarak ölçülmüştür. PEO esaslı % 5 MgBDC MOF ve % 20 LiTFSI içeren NCPE' nin iyonik iletkenliği diğerlerine kıyasla olağanüstü şekilde iyileştirilmiştir ve iyonik iletkenlik değeri 3.26×10^{-4} S/cm bulunmuştur. Bu sonuçlara göre; MgBDC MOF içeren katı NCPE'ler; yüksek sıcaklığa dayanıklı katı polimer elektrolit lityum pillerin üretiminde nano ölçekli MOF içermesi açısından nanokompozit polimer elektrolitler arasında yeni bir aday olarak yerini alabilir.

Anahtar Kelimeler: Lityum pil, Katı polimer elektrolit, MOF, İyonik iletkenlik.

ABSTRACT

SYNTHESIS AND PROPERTIES OF POLY(ETHYLENE OXIDE) BASED NANOCOMPOSITE ELECTROLYTES CONSISTING OF NANO-SIZED Mg-BDC METAL ORGANIC FRAMEWORK

Ayşe ERCİYES
Ondokuz Mayıs University
Institute of Graduate Studies
Department of Nanoscience and Nanotechnology
Ph.D., July 2021
Chair of Department: Prof. Dr. Müberra ANDAÇ

Looking at the latest developments in lithium (Li) battery technology, solid polymer electrolytes (SPE) have begun to substitute the traditional liquid electrolyte. So, SPEs have an important place in modern energy technology. In this thesis, nanosized magnesium benzene dicarboxylic acid metal-organic frameworks (MgBDC MOFs) were successfully synthesized via the electrochemical (EC) method without metal salts. The highly crystalline phase and the characteristic reflection peaks of nanosized MgBDC MOFs were confirmed based on x-ray diffraction (XRD) results. Their dimensions-spherical shape-smooth structure, regional-mapping-spectrum analysis, and surface topography of nanosized MgBDC MOFs were determined by scanning electron microscopy (SEM), scanning tunneling electron microscopy (STEM), energy dispersive x-ray spectroscopy (EDS), and atomic force microscopy (AFM) techniques, respectively. Thermogravimetric analysis (TGA), attenuated total reflectance fourier transform-infrared spectroscopy (ATR FT-IR), and brunauer–emmett–teller (BET) analyzes were performed to investigate the thermal stability-degradation, organic bond structures, and surface area (m^2/g) of them, respectively. Nanocomposite polymer electrolytes (NCPEs) consisting of MgBDC MOF were successfully produced by using the method of solution casting. Homogeneous distribution and of nanosized MgBDC MOF structures and the presence of chemical elements within polyethylene oxide-lithium bis(trifluoromethanesulfonyl)imide (PEO-LiTFSI) electrolyte matrix was examined by SEM/EDS. Based on XRD and differential scanning calorimetry (DSC) data, the crystal phase structure and the percent crystallinity of PEO decreased dramatically from 70% to ~20% because of the combination of nanosized MgBDC MOF to PEO-LiTFSI salt system. In addition, crystal formations of polymer electrolytes were researched by polarized optical microscopy (POM) analysis. The interactions between cations in the lithium salt and the ether-oxygen molecules in the PEO chains were confirmed with the help of the ATR FT-IR spectroscopy device. Based on TGA results, the thermal stability of NCPEs improved. The ionic conductivities of NCPEs were measured using electrochemical impedance spectroscopy (EIS) analysis in various temperature ranges. Ionic conductivity of PEO-based NCPE containing 5 wt. % MgBDC MOF and 20 wt. % LiTFSI was outstandingly improved in comparison to the other samples and ionic conductivity value was found to be 3.26×10^{-4} S/cm. According to these results, MgBDC MOF-based solid NCPEs can take their place as a new candidate among nanocomposite polymer electrolytes in terms of containing nanoscale MOF in the production of solid polymer electrolyte lithium batteries that are resistant to high temperature and safe.

Key Words: Lithium battery, Solid polymer electrolytes, MOFs, Ionic conductivity.

ACKNOWLEDGMENTS

I would like to thank Prof. Dr. Engin Burgaz, who was my doctoral thesis advisor for a while, for sharing all of my knowledge and experiences with me.

Later, this doctorate thesis study was carried on under the control of Prof. Dr. Müberra ANDAÇ, who is Head of the Department of Nanoscience and Nanotechnology. That's why, I would thank sincerely Prof. Dr. Müberra ANDAÇ for her knowledge, moral support, and all efforts during my doctorate study.

I am so grateful to Prof. Dr. Engin BURGAZ and Asst. Prof. Dr. Aydemir Güralp URAL for reading this thesis, listening to my presentations, giving positive critical comments, fruitful discussion, and adjustments.

During our 24-month work together in the TÜBİTAK 1001 project, I owe a lot to my esteemed professors, Müberra ANDAC, Ömer ANDAÇ, and Engin BURGAZ for giving me all kinds of knowledge and motivation (laboratory experiments, collective work, inter-active work, manuscripts, etc.) and for maturing me both academically and in my normal life.

I would like to thank my friend, Engineer Msc., Caner KENDİRLİOĞLU, for his serious assistance in the project.

Thank my friends, Res. Asst. Merve YİĞİTER and Dr. Suna AVCIOĞLU from Ondokuz Mayıs University, Nanoscience and Nanotechnology Department, for their moral and material support during my doctoral studies and these difficult times.

I am indebted to my friends Res. Asst. Tuğba MUTUK, Asst. Prof. Dr. Sinem ÇEVİK, Res. Asst. Mehmet KURU and Dr. Mehmet YAZICI from Ondokuz Mayıs University, Metallurgy and Materials Engineering Department, for giving me positive energy and high motivation during these difficult years.

I would like to thank Teaching Asst. Kübra YONTAR for her moral and material support.

A special thank her to my close and dear friend for encouraging me to work constantly, for never leaving me alone in my difficult times.

Finally, I heartily thank my dear parents and the whole family who always stood by me in this very difficult and intense process. This thesis has not have been possible without their strong support.

Ayşe ERCİYES

TABLE OF CONTENTS

LIST OF SYMBOLS

SYMBOLS

Symbol	Explanation	Unit
Li^+	Lithium cation	-
σ	Ionic conductivity	S/cm, Scm^{-1}
$LiN(SO_2CF_3)_2$	Lithium bis(trifluoromethanesulfonyl)imide	-
ε	dielectric constant	-
t_{Li}^+	Lithium-ion transference number	-
υ	Stretching vibrational	-
υ_a	Asymmetric stretching vibrational	-
υ_s	Symmetrical stretching vibrational	-
υ_{as}	Asymmetric-symmetrical stretching vibrational	-
δ	Bending vibrational mode	-
δ_a	Asymmetric bending vibrational	-
δ_s	Symmetric bending vibrational	-
δ_{as}	Asymmetric-symmetric bending vibrational	-
θ	Theta angle	-
X_c %	Percent crystallinity	-
X_c	Degree of crystallinity	-
T_g	Glass transition	-
T_m	Melting temperature	-
T_b	Boiling point	-
Tf	Flashpoint	-
q	Heat flow rate	W/g
ΔH	Enthalpy	J/g
ΔH_m	Melting enthalpy	J/g
Z	Impedance	Ω
t	Thickness of material	cm
R_b	Bulk resistance	Ω
A	Area of SPE film	cm^2
d	Distance of two electrode	cm
w	Width of film	cm
E_a	Activation energy	J/mol
k	Boltzmann constant	-
S_{BET}	Total surface area	m^2/g
V_{pore}	Pore volume	cm^3
M_w	Molecular weight	g/mol
V	Volt	J/C
mA	Milliampere	Coulomb/second
DC	Direct Current	Hertz, Hz -
AC	Alternative Current	Hertz, Hz
mV	Millivolt	Ω
E_a	Thermal Activation Energy	Joule/mol, eV

LIST OF ABBREVIATIONS

Abbreviation	Explanation
LIBs	Lithium-Ion Batteries
PEO	Poly(Ethylene Oxide)
SPEs	Solid Polymer Electrolytes
MOFs	Metal Organic Frameworks
EO	Ethylene Oxide
$TFSI^-$	bis(trifluoromethanesulfonyl)imide anion
LiTFSI	Lithium bis(trifluoromethanesulfonyl)imide
EO/Li^+	Ethylene oxide-Lithium cation complexation
MgBDC MOF	Magnesium Benzene Dicarboxylic Acid Metal-Organic Frameworks
CPE	Composite Polymer Electrolyte
NCPEs	Nanocomposite Polymer Electrolytes
XRD	X-Ray Diffractometer
SEM	Scanning Electron Microscopy
STEM	Scanning Tunelling Electron Microscopy
EDS	Energy Dispersive X-Ray Spectroscopy
AFM	Atomic Force Microscopy
TGA	Thermogravimetric Analysis
ATR FT-IR	Attenuated Total Reflectance Fourier Transform-Infrared
BET	Brunauer–Emmett–Teller
DSC	Differential Scanning Calorimetry
POM	Polarized Optical Microscopy
EIS	Electrochemical Impedance Spectroscopy
3D	three-dimensional
RT	Room Temperature
ST	Solvothermal
HT	Hydrothermal
US	Ultrasound
MW	Microwave
EC	Electrochemical
BTC	1,3,5-Benzene tricarboxylic
$LiClO_4$	Lithium perchlorate
$LiBF_4$	Lithium borate
$LiAsF_6$	Lithium arsenate
$LiPF_6$	Lithium phosphate
$LiSbF_6$	Lithium antimonates
DMF	N,N-dimethylformamide
OH^-	Hydroxyl functional group
COO	Carboxyl functional group
$Mg(OH)_2$	Brucite phase
eV	Electronvolt

LIST OF FIGURES

LIST OF TABLES

1. INTRODUCTION

1.1. The Aim and Scope of This Study

Lithium-ion batteries (LIBs) were successfully made commercial for the first time in the world in 1991 by Sony and Asahi Kasei corporations. LIBs of these electronic devices, which are widely used by consumers, is still required improvement in the way of performance such as riskless, power density, and exposure time (Mathew et al, 2019; Smith, 2010; Goodenough and Kim, 2010). The state-of-the-art technology of LIBs is used in the batteries of electrical devices such as mobile phones, computers, video cameras, notebook computers, portable mini-disk players, and others that have become a part of our daily life. Highly risky, volatile, and a flammable carbonate-based organic liquid electrolyte-containing material is used in these LIBs (Yuan et al., 2013; Tarascon and Armand, 2001). New types of electrolytes have been studied to figure out these problems such as low thermal stability and serious safety (Yuan et al., 2013; Mathew et al., 2019; Tarascon and Armand, 2001; Tang et al., 2012).

Yuan et al. (2013) stated that the complexations of alkali metal salts in the PEO matrix and their effect on ionic conductivity were firstly performed by Wright (1976). Also, these researchers reported that Armand et al. (2011) preferred these materials as solid electrolytes in batteries. PEO-based SPEs have become the center of attention of researchers, and many studies have been conducted on solid polymer electrolytes (SPEs) in terms of replacing the liquid organic electrolyte in LIBs (Yuan et al., 2013; Mathew et al, 2019; Tang et al., 2012). SPEs exhibit high mechanical flexibility and thermal stability. These materials can be used instead of inflammable liquid electrolytes due to their higher energy density, improved safety, and reduced weight (Tarascon and Armand, 2001; Tang et al., 2012; Armand et al., 2011).

PEO which is one of the most important polyether compounds has been mostly preferred in SPEs as the matrix material since it can dissolve many different salts (Burgaz, 2011; Burgaz et al., 2014; Lightfoo et al., 1993) and it can also provide fast ion transport (Labrèche et al., 1996; Abraham et al., 1997; Burgaz, 2011; Burgaz et al., 2014). This useful structure of PEO is mainly coming from its ethylene oxide-lithium (EO/Li^+) complexes which are formed *via* the coordination of ether oxygen with lithium ions (Wang et al., 2017). The mechanism of lithium cation (Li^+) transport

in PEO electrolytes is related to the diffusion of cations throughout the amorphous region where local relaxivity and sectional movement of PEO chains are triggered by actual ether-oxygen linkages at favorable interatomic separations (Prasanth et al., 2014; Jinisha et al., 2017). However, Stoeva et al. (2003) reported in a solid lithium-ion battery study that all-solid-state PEO lithium salt complexes generally are of very low ionic conductivity between 10^{-6} and 10^{-7} S/cm and exhibit weak mechanical properties. Although the inorganic solid electrolyte shows good thermal stability, the ionic conductivity is low in applications due to the poor electrode-electrolyte connection (Kato et al., 2016; Kataoka et al., 2018). PEO exhibits low ionic conductivity at room temperature due to its highly crystalline morphology (Burgaz, 2011).

To overcome these difficulties, different techniques such as increasing the amount of lithium salt and mixing a low molecular weight plasticizer are comprehensively studied to decrease the high proportion of crystal phase while increasing the amorphous structure (Tang et al., 2012; Sheldon et al., 1989; Yang et al., 1995; Lee et al., 1994). These methods usually improve the ionic conductivity of PEO, however, the physical strength and thermal stability of polymer membrane decrease because of the flexible and amorphous structure of plasticized polymer chains. Another technique is the adding of inorganic fillers into the polymer materials to build a composite polymer electrolyte (CPE) (Jiang et al., 2008; Chung et al., 2001; Kumar et al., 2013). When inorganic agents are used as solid plasticizers, the readjustment of polymer chains can be kinetically blocked in virtue of Lewis acid-base interactions such as filler, polymer, and ionic species. Thus, Li salts more easily decompose and the mobility of Li ions is improved. Also, mechanical features of the inorganic-organic hybrid electrolyte system can be changed through the choice and design of inorganic fillers (Fu et al., 2016). Nanoscale inorganic filler materials have been usually incorporated into PEO electrolytes (Burgaz, 2011; Tang et al., 2012; Wang et al., 2017). Thereby, they have improved their high ionic refractivity, electronic insulation, the mechanical, chemical, and thermal stability of SPE (Tang et al., 2012; Wang et al., 2017; Lee et al., 1994; Coleman et al., 2006; Scrosati et al., 2000; Pitawal et al., 2007; Xiong et al., 2001).

Metal-organic framework structures are briefly referred to as MOFs. They are also known as porous inorganic materials and have metal ions and organic ligands.

The metal-ligand networks are infinitely extendable with metal nodes and bridging the organic functional ligands, which form network frame-like structures. These are called porous coordination polymers or coordination polymer networks. The coordination polymer network forms have one-dimension (1D), two-dimension (2D), and three-dimension (3D) structures as demonstrated in Figure 2.7 **(**Kitagawa et al., 2004; Batten et al., 2012; Park et al., 2006). The structure of MOFs is similar to that of zeolites or aminophosphates, but MOFs consist of hybrid materials. Also, there are many advantages of MOFs compare to the well-known nanoporous zeolites due to their specific properties such as structural and functional group tunability (Sel et al., 2015; Chen et al., 2011; Janiak et al., 2010). MOFs have specific properties such as high porosity, high surface area (500-6500 m^2/g), high thermal stability, three-dimensional (3D) structures, low density (0.2-1 g/cm^3), elasticity, variability of their pore size (0.3-3.5 nm), surface polarity through a proper option of organic linker tunable chemical functionality (Yang et al., 2010; Eddaoudi et al., 1999; Furukawa et al., 2010). MOFs can be synthesized by using various types of benzene derived organic linkers such as 1,4-benzene dicarboxylic acid (H_2BDC or terephthalic acid), naphthalene dicarboxylic acid, and 1,3,5-benzene tricarboxylic acid (H_3BTC or trimesic acid) (Chen et al., 2011; Rowsell et al., 2005; Ma et al., 2010; Eddaoudi et al., 2002; Rosi et al., 2003; Gascon et al., 2009; Zhang et al., 2012). The organic ligands consisting of carboxylate groups can make many different and strong bonds with metal cations. MOFs consisting of carboxylate ligands have better catalytic performance, higher surface area, and larger pore size (Gascon et al., 2009) The geometry of BDC is very close to a rod-like structure (Chen et al., 2011; Rowsell et al., 2005). Since conjugated carboxylate groups with aromatic rings consist of strong π-π interactions, they are straightforwardly bonded with metal ions and form MOF structures with high strength (Rowsell et al., 2005; Horike et al., 2013). MOF structure can be obtained using diverse benzene organic ligands with different ring numbers. Different techniques such as room temperature (RT), solvothermal (ST), hydrothermal (HT), ultrasound (US), electrochemical (EC), and microwave (MW) can be used to synthesize (Burgaz et al., 2019).

Joaristi and co-workers (2012), synthesized Cu–BTC-based MOF and Al–BDC MOF materials *via* the electrochemical method using different organic linkers. They

reported that MOFs were synthesized *via* faster reactions at lower temperatures without using metal salts.

In a previous study, zirconium-based MOF (Zr(IV)–BDC MOF) was synthesized *via* the electrochemical method by using zirconium foil with a BDC linker. It was reported that Zr–BDC-based MOF film has improved mechanical properties, a very stable structure, and good performance characteristics (Stassen et al., 2015).

Angulakshmi et al. (2014) synthesized Mg–BTC MOFs *via* the electrochemical method and they added Mg–BTC-based MOF into PEO-based SPE containing Li salt. The adding of Mg–BTC-based MOF into the PEO electrolyte significantly enhanced the ionic conductivity up to two orders of magnitude.

Yuan et al., (2013) produced nanosized Zn–BDC-based MOF-5 *via* the solvothermal method, and MOF-5 was successfully incorporated into PEO–LiTFSI electrolyte. It was also shown that electrochemical features of PEO-based SPE consisting of Zn–BDC-based MOF-5 enhanced in the lithium-ion battery. The highest ionic conductivity of the PEO-based composite polymer film was reported to be 3.16×10^{-5} S/cm at 25 °C.

Previously, Ni-BTC-based MOF was synthesized by using the solvothermal method, and it was integrated with a polymer electrolyte consisting of LiTFSI. It was reported that the included Ni-BTC-based MOF made a tremendous contribution in improving mechanical, thermal, and ionic conductivity features of polymer electrolytes (Suriyakumar et al., 2016).

In another work, Mg–BDC-based MOFs were synthesized by using poly(vinylpyrrolidone)-assisted solvothermal method and they were used in the generation of Mg/MgO-containing mesoporous carbon which was utilized like the cathode electrolyte support in lithium batteries. Mg–BDC MOF-derived cathode exhibited good electrochemical stability and it was concluded that MOF-derived strategy has a high potential in designing new carbon materials for Li-S battery applications (Dhawa et al., 2017).

Mathew et al., (2019) were synthesized micro-sized Mg–BDC and Mg–BTC MOFs at room temperature using the dropwise method. After the synthesis, various amounts of these micro-sized MOFs material and LiTFSI salt were mixed into the

polymer substance and polymer-based micro composite films were prepared. CPEs had an ionic conductivity value of 7.02×10^{-4} S cm^{-1} at 70 ºC temperature.

In this study, high efficiency nanosized magnesium-1,4-benzene dicarboxylic acid (MgBDC) MOF is produced by using BDC organic ligand and magnesium ribbons. Also, it is preferred to use PEO material and LiTFSI salt as the matrix. The first aim of the thesis study is to reveal that homogeneous MgBDC based MOF nanoparticles can be manufactured in high yields (81%) *via* the electrochemical (EC) method at ambient temperature. Morphology/chemical compounds, crystal structure, thermal stability, molecular interactions, surface topography, and total surface area of MgBDC MOF nanostructures were determined by SEM/EDS, XRD, TGA, ATR FT-IR, AFM, BET analyses, respectively in detail.

The second aim of this research work is to incorporate these synthesized homogeneous MgBDC based MOF nanoparticles with different concentrations into PEO–LiTFSI matrix. In this context, PEO-based nanocomposite polymer electrolytes (PEO-based NCPEs) containing different lithium salt and nanosized MgBDC MOF amounts are intended to prepare by casting method. The morphology/chemical compounds, crystalline phase structure, thermal stability, crystallinity, molecular interactions, and spherulitic morphology properties of PEO based NCPE membranes were determined by SEM/EDS, XRD, TGA, differential scanning calorimeter (DSC), ATR FT-IR, polarized optical microscopy (POM) and analyses, respectively in detail. After these prepared PEO-based NCPE membranes are successfully characterized, it is aimed to enhance the ionic conductivity performance of these membranes. For this reason, ionic conductivity measurements were analyzed using impedance spectroscopy at different temperature ranges.

1.2. The Originality of The Work

There have been a few studies in the literature on PEO-based nanocomposite polymer electrolytes and polymer electrolytes obtained with nanosized MOF-containing fillers. Therefore, the synthesis of MgBDC MOF particles with very low nanosize by electrochemical method and the production of PEO-based nanocomposite polymer electrolytes by dispersing these nanoparticles homogeneously in the polymer reveals the unique aspect of this study.

In nanocomposite polymer electrolyte production, it is important that nanoparticles are well dispersed in the polymer matrix and there is no agglomeration. For this reason, it is desirable to obtain nanocomposite polymer electrolytes that are smooth and advanced performances. In this context, the use of nano-sized MOF crystals as nanofillers in polymer nanocomposites can be among the ambitious and strong candidates due to their wide range of applications and specific properties.

On the other hand, the scale-up procedures of NCPEs are substantial in terms of superior ionic conductivity and durable Li-ion battery electrolyte researches. So, there may be some problems in the scale-up of nano-sized MOFs. The sudden and uncontrolled chemical events can lead to the scale-up of MOF nanoparticles. Therefore, the electrochemical method is preferred to synthesize MgBDC MOF with high efficiency and uniform nanoparticles. The manufacturing of high efficiency and uniform MgBDC MOF nanoparticles without the need to use any surface-active agents, metal salts, coating materials, or a dangerous crystal formation blocking agent is highly required in different fields of application.

Based on previous studies in the literature, uniform MgBDC based metal-organic frameworks nanostructures were not manufactured *via* the EC method by using magnesium ribbons as an anode and cathode in a solution. Also, these uniform nanosized MOF structures were not homogeneously and well distributed in the polymer matrix. In this respect, this study is of the very original value.

2. LITERATURE RESEARCH

2.1. Liquid electrolytes

It may be interesting that nanomaterials used in rechargeable lithium batteries can be improved the features of classic liquid electrolytes, but there is currently good proof for such an improvement. By adding powder materials in nanoparticle forms such as aluminum oxide (Al_2O_3), silica (SiO_2), and zirconium oxide (ZrO_2) to anhydrous electrolytes the conductivity value can be increased by a factor of six (Bruce et al., 2008; Bhattacharyya and Maier, 2004). Anisotropic powers forces at the liquid or solid phase interface differ when compared to the isotropic forces acting in the mass of both media. Due to the equilibrium changing among free ion and ion pairs, the vacancy load and bipolar at the interface are affected. So, the conductivity is exposed to change.

Besides, these changes also cause separation of the ion pair, and in this case, the particles are strengthened with the help of certain adsorption such as anions on the surface. Also, the activity can be increased along the surface. This situation concerns the expansion of the surface/volume. The greater the surface/volume, the less the impact per unit mass of bulk. A sufficient amount of powder material is needed to make it infiltrate from one surface to another. In this way, advanced regional conductivity may provide longtime transmission by the membrane. These materials are referred to as "soggy sands" due to the amount of powder desired and the resulting physical features (Bruce et al., 2008).

Liquid electrolytes contain organic solvents like propylene carbonate (PC), ether, ethylene carbonate (EC), and linear dialkyl carbonate such as dimethyl carbonate (DMC). The suitable electrolyte solvent required for liquid electrolytes should provide the following properties:

1- Salts should be easily soluble in certain concentrations by the electrolyte. That is, it must have an ideal dielectric constant (ε).

2- It must be liquidity and low viscosity (η) for easy ion movement.

3- It must not react with charged surfaces when cell work is done.

4- It must be in a liquid phase in a large temperature range.

5- It must be risk-free, harmless, and cheap (Xu, 2004).

Although active protons have superior powers in solvent salts, the reduction of active protons and or oxidation of anions usually takes place between 2.0 - 4.0 V against lithium material (Fry, 1989). As for the current rechargeable lithium devices, the average charged potentials of the anode 0.0-0.2 V and that of the cathode is 3.0-4.5 V. Due to the natural structure of powerful reductive anodes and oxidative cathodes, no solvent is needed in lithium-based batteries (Xu, 2004).

2.2. Solid Polymer Electrolytes (SPEs)

Polymer electrolytes consist of the most important and oldest classes of polymer electrolytes to this day. These are formed by dissolving the salt in a macromolecular weight polymer (Armand et al., 2011). The coordinating salt cations must be able to act as ligands and also contain donor atoms that can provide dissolution enthalpy to improve polymer electrolyte formation (Armand et al., 2011; Gray, 1997; Bruce, 1995). Polymer electrolytes are known as SPEs, and poly(ethylene oxide) (PEO) is the most common among them, on the other hand, there are some advantages that polymers are in terms of cost, production, and process (Fu et al., 2016). Polymer electrolytes have two general types that are polymer–salt complex and polyelectrolytes. Polymer–salt complex is a coordination polymer such PEO–LiTFSI, poly(ethylene oxide)–lithium perchlorate (PEO–$LiClO_4$), etc. Polyelectrolytes are covalently attached charged groups. The improvement of polymer electrolytes has attracted considerable attention in point of their potential applications such as electrochemical apparatus, rechargeable lithium batteries (Persi et al., 2002). They possess numerous specific features such as superior ionic conductivity, large electrochemical stability windows, no need for solvent use, ideal specific energy, slight and simple processing (Gerbaldi et al., 2014; Bruce et al., 2008). They are suitable for flexible battery applications due to their low elastic modulus properties. Lithium salts in a suitable polymer electrolyte without solvent are dissolved and solvated through polymer chains (Sel et al., 2015). The ionic conductivities of PEO-based electrolytes show very low values from 10^{-8} to 10^{-4} S cm^{-1} at 40-100 °C temperatures (Stephan, 2006). The polymer crystallizes at room temperature and so, the movement of Li^+ ions is largely hindered. Eventually, the desired ionic conductivity value above 10^{-4} S cm^{-}

[1] at ambient temperature still has not been reached in nonsolvent polymer electrolytes (Fu et al., 2016). The ionic movement of a lithium-ion in a polymer guest.

Lately, it is thought that certain constructional mutations should be made in polymer membranes to improve their electrical and thermal performances and to make them commercially acceptable for use in electrochemical devices. Also, their electrical conductivity needs to be increased. Mostly, the polymer and inorganic salts are mixed to improve ionic conductivity. Thanks to the mobility of inorganic salts that decompose into ions, the ionic conductivity properties of polymer electrolytes are enhanced (Sel et al., 2015).

2.2.1. Nanocomposite (amorphous) polymer electrolytes

Polymer electrolytes, which have an important place in modern energy technology, consist of a class of materials. Intensive studies are carried out on polymer electrolytes for advanced lithium metal and lithium ion-based high energy density batteries (Armand et al., 2011). The advancement in lithium-ion battery technology is based on replacing a traditional liquid electrolyte with a development SPE (Scrosati, 2002). For this reason, several polymers-based lithium membranes are made to succeed in this aim and then their properties have been investigated (Scrosati, 2005). However, it should be noted that undoubtedly the greatest interest is on PEO-based SPEs (Scrosati and Vincent, 2000).

Corresponding to SPEs, these membranes occur with the mixture of PEO and lithium salt to each other. PEO chains move together with structural and solvent substances, on the other hand, they are free of plasticizing solvents (Grey and Armand, 1999). SPEs containing PEO are important in terms of properties such as cheap, risk-free, and chemical resistance. However, SPEs have some issues. It has low conductivities is at below 70 °C, thus limiting the range of applications in lithium polymer batteries. In addition to this, the lithium-ion transport number (t_{Li^+}) is usually in the order of 0.2-0.4, that is, low. The t_{Li^+} is usually in the order of 0.2-0.4, that is, low. The conductivity is caused by the movement of the anion. For this reason, it may cause concentration polarization by restricting the velocity or battery life. As previously mentioned, various methods have been developed to overcome these disadvantages (Bruce et al., 2008).

The first method is increasing the amount of lithium salt, the addition of a low molecular weight plasticizer studied broadly to decrease the high content of crystal while increasing the amorphous structure (Tang et al., 2012; Sheldon et al., 1989; Yang et al., 1995; Lee et al., 1994). As the second method, a composite polymer electrolyte (CPE) can be obtained by blending organic solvent into the polymer to enhance ionic conductivity. However, there is a risk for both the safety and mechanical properties of this method. The third method is the adding of inorganic fillers into the polymer materials to build a composite polymer electrolyte (CPE) and a digital photograph of a sample composite electrolyte (Jiang et al., 2008; Chung et al., 2001; Kumar et al., 2013).

When the inorganic agents are used as solid plasticizers, the readjustment of polymer chains can be kinetically blocked because of the interactions among Lewis acid-base that occur between filler, polymer, and ionic species. Thereby, Li salt is more easily decomposed. The mobility of Li ions is improved. Also, mechanical features of the inorganic-organic hybrid electrolyte system can be changed through the choice and design of inorganic fillers (Fu et al., 2016). The dispersion of ceramic fillers consisting of nanoparticles such as titanium dioxide (TiO_2), Al_2O_3, and SiO_2 in the polymer matrix leads to a significant increase in the transport features of PEO-based SPEs. It has been included in the novel cluster of SPEs as a nanocomposite polymer electrolyte (NCPE) (Bruce et al., 2008). When preparing these nanocomposite polymer electrolytes, the inorganic filler and lithium salt are first dissolved in a low boiling solvent (e.g. acetonitrile), then the solution is turned into a slurry by adding the PEO polymer material and the obtained slurry is well mixed. The slurry is then homogeneously cast into a Petri plate and mechanically stable membranes are obtained (Armand et al., 2011). It has been reported that inorganic filler added to the polymer material prevents the crystallization of the PEO chain in the polymer membrane, which is the amorphous structure at 70 °C and thus the filler behaves like a solid plasticizer (Bruce et al., 2008; Croce et al., 1999; Croce and Scrosati, 2003). Thanks to this prevention, the stability of the amorphous structure is achieved at low temperatures. In this way, the increase in polymer electrolyte conductivity is achieved. It is also contributed to an increase in the Li_t^+ interactions among Lewis acid-base that occur among the inorganic filler, X^- anion of the salt, and PEO chain fractions (Appetecchi et al., 2000; AricQ, 2005). The development of SPEs for lithium batteries is based on

the preference of inorganic material (e.g. ceramic filler) and its surface structure. This has been proven by the examination of sulfate-based superacid zirconia material (Croce et al., 2006a). This refined ceramic filler is twice as much resistant to sulfuric acid (H_2SO_4). The processed zirconia has twice the acid strength compared to sulphuric acid (H_2SO_4). It should be noted that there is a good electron uptake capability of coordinated nonsaturated Zr^{4+} cations and they are improved with the affinity of the charge-pull sulfate-based groups (Bruce et al., 2008). The dispersion of the ceramic filler, one of the inorganic fillers, in the SPE led to a nanocomposite electrolyte with superior transference features. In a previous study, the t_{Li}^+ studied by using the classical method of Bruce and Vincent was found in the range of 0.81-0.05. The t_{Li}^+ of ceramic-free polymer membrane is in the range of 0.42-0.05. Based on this result, the researchers said the polymer with ceramic filler was almost 100% larger than the one without electrolyte (Croce et al., 2006a). It is reported that nanocomposite polymer electrolytes prepared using a proper ceramic filler improve both conductivity and t_{Li}^+values. The enhanced NCPE based lithium-ion battery shows better cycle life reduction in the cycle, on the other hand, there is a particularly stable charge-discharge efficiency (Croce et al., 2006b).

2.2.2. Crystalline polymer-based electrolytes

Crystalline-based polymer electrolytes were insulating and the conduction was only occurring when above a certain temperature in amorphous condition, according to the stereotyped view of 25 years (Armand et al., 2011; Christie et al., 2005; Scrosati, 2005).

Based on recent studies by researchers, it has been predicted that salts such as LiXF6, where X = P, As, Sb, can be soluble in PEO-based SPE and form crystal complexes, which can help ionic conductivity (Bruce et al., 2008; Gadjourova et al., 2001). The crystal complexation of six ether oxygen atoms and lithium ions, PEO_6: $LiXF_6$, X =Sb, P, As has a crystalline texture that can form tunnels through which PEO chains can move to lithium ions. Using short PEO chains in the nanoscale range is very important in terms of forming longer chains, preventing crystallization, and stopping chain entanglement. Also, the changing of the chain length in the nanoscale range has a positive effect on conductivity (Bruce et al., 2008).

To triple the conductivity at room temperature, the average chain length is reduced from 44 EO units (mol. mass approx. 2000, average chain length approx. 9 nm) to 22 EO units (mol. mass 1000, average chain length 4.5 nm) (Stoeva et al., 2003). It is crucial to check both the length of the average chain and dispersity in the nanoscale range. Generally, while producing a polymer, chain reactions occur and thus polydisperse chains are derived. Compared to equivalent monodisperse materials, these polydisperse chains show higher conductivity (Staunton et al., 2007). The length of the average chain is too short compared to crystal size (200-250 nm) and this situation is related to the origin of the nanoscale. After all, each crystallite has many chains ends. These are natural defects, for instance, it supports the lost lithium ions due to the inability of the outer oxygen atoms at the chain ends to complete their coordination. Therefore, the small chains and polydispersity lead to a high density of defects (Staunton et al., 2007).

2.3. Metal-Organic Framework (MOF) Structures

2.3.1. General definitions

Coordination compound

Its definition according to the IUPAC Red Book is as follows: “a coordination compound is any compound that contains a coordination entity. A coordination entity is an ion or neutral molecule that is composed of a central atom, usually, that of a metal, to which is attached a surrounding array of atoms or groups of atoms, each of which is called a ligand” (Damhus et al., 2005).

Polymer

The word polymer means “the substance formed by the combination of macromolecules” (Batten et al., 2012).

Polymer molecule (macromolecule)

Based on the description of IUPAC, the word “macromolecule” preferred mostly in the polymer field corresponds to the only molecule. For instance, it is correct to refer to a substance consisting of macromolecule structures for a single polymer molecule as "macromolecule" or "polymer molecule" rather than using "polymer" called. It is formed by the repetition of relevant building blocks (Batten et al., 2012).

Coordination polymer

This term is defined as organometallic polymer material consisting of metal ion centers connected with linkers (Li et al., 1999; Eddaoudi et al., 2002; Rosi et al., 2003; Yaghi et al., 1995). Currently, they are known as metal-organic frameworks.

2.3.2. Concept of metal-organic framework (MOF)

Metal-organic framework structures are briefly referred to as MOFs and this term was made popular by Yaghi et al., (1995). They are also known as porous inorganic materials and have metal ions and organic ligands. The metal-ligand networks are infinitely extendable with metal nodes and bridging the organic functional ligands, which form network frame-like structures. These are called porous coordination polymers or coordination polymer networks. The coordination polymer network forms have 1D, 2D and 3D structures **(**Kitagawa et al., 2004; Batten et al., 2012; Park et al., 2006). The structure of MOFs is similar to that of zeolites or aminophosphates, but MOFs consist of hybrid materials. Also, there are many advantages of MOFs compared to the well-known nanoporous zeolites due to their specific properties such as structural and functional group tunability (Sel et al., 2015; Chen et al., 2011; Janiak et al., 2010).

2.3.3. Classification of MOFs

MOFs can be grouped into three different classes according to their structural aspects in recent studies **(**Kitagawa et al., 2004). Firstly, they are called the first (1^{st}) generation MOFs. This 1^{st} generation MOFs only persist with guest molecules such as solvent, neutral or ionic species and are irreversibly degraded by their removal. Secondly, they are known as the second (2^{nd}) generation MOFs. Second-generation MOFs consist of fixed and robust porous structures. When the guest particles in the pores are lifted from the structure, there is no change in the structure of the MOFs, they exhibit durable porosity. Numerous inorganic porous structures built through covalent bands are included in the group of 2^{nd} generation MOFs. Thirdly, they have named the third (3^{rd}) generation MOFs. These structures of 3^{rd} generation MOFs are elastic and energetic frameworks. They react to the outer stimulant, such as guest particles, light, electric area and they also turn their pores or channels into reversible

in terms of geometric parameters such as shape, dimension, crystal lattice **(**Kitagawa et al., 2004). On the other hand, MOFs are usually recognized as zeolite-like MOFs (ZMOFs) and carboxylate MOFs. The anionic charge of ZMOFs is just like that of zeolites and for this reason, it is referred to as the anionic framework in cation exchange applications. The carboxylate group MOFs have come to the fore because of their specific features such as high thermal stability, more pore sizes, and large characteristic surface area **(**Kitagawa et al., 2004).

In addition to all these, it is necessary to inform that it has four types of porous structures in terms of spatial dimensions. The wall molecules completely encircle 0D cavities (dots). In these vacancies, it is possible to isolate a specific guest or distribute it within its solid. Regular 1D channels are formed by synthesizing a large number of coordination polymers. The 2D layers are formed by the interpolation of dozens of coordination polymers. By connecting 1D channels from various directions, 3D intersecting channels are formed. Hence, channels in (1D) one-dimensional, layers in (2D) two-dimensional and intersect channels in (3D) three-dimensional are usually used to settle in or change guests **(**Kitagawa et al., 2004).

2.3.4. Properties of MOFs

MOFs have specific properties such as high porosity, high surface area (500-6500 m^2/g), high thermal stability, three-dimensional (3D) structures, low density (0.2-1 g/cm^3), elasticity, variability of their pore size (0.3-3.5 nm), surface polarity through a proper option of organic linker adjustable chemical functionality (Yang et al., 2010; Eddaoudi et al., 1999; Furukawa et al., 2010). Based on IUPAC, porous compounds are grouped according to their diameters of pore sizes, they usually have micro-porous of below 2 nm, mesoporous of between 2 - 50 nm, and macroporous of above 50 nm structures **(**Kitagawa et al., 2004). These materials are not degraded by the addition or removal of solvents and other guest molecules, for this reason, they are rigid porous structures (R.S. Kumar, 2014).

2.3.5. Organic linkers

There are two types of organic ligands, namely aromatic dicarboxylic acid ligands and aliphatic dicarboxylic acid-based ligands **(**Kitagawa et al., 2004; Janiak et

al., 2010; Livage et al., 2001). Aromatic dicarboxylic acid-based ligands have a solid structure and are a versatile material for the gas storage application field. Substances such as succinic and glutaric acids are aliphatic dicarboxylic acid-based ligands, and they are elastic. It is in hydrophobic interaction with alkyl chains **(**Kitagawa et al., 2004; Livage et al., 2001). MOFs are also commonly known as nitrogen-based MOFs and carboxylate-based MOFs depending on the organic ligand part. Nitrogen-based MOFs (e.g. 4,4'-bipyridine ligand molecules) provide linear space adjustments between metal linkers. Additionally, they act as hydrogen bond acceptors in gas storage applications. The carboxylate MOFs consist of two subgroups, among themselves fluorinated (F-MOFs) and non-fluorinated MOFs (Janiak et al., 2010). Perfluorinated carboxylate-based MOFs are remarkably more acidic, more unstable, and less soluble in common organic solvents compare to the non-fluorinated carboxylates. It has also been stated that they allow better hydrogen gas (H_2) storage materials because they bind H_2 gas more robustly and efficiently (Pachfule et al., 2011; Hulvey et al., 2011).

Various framework structures with different metal ions and groups are obtained from benzene-di-, tri-, tetra-carboxylic acid-derived ligands in combination. The dicarboxylate building blocks, which are flexible, tend to change their structural properties from 1D to 2D networks in terms of the types of ligands. By the reason of the long molecular nature of the basic building block units, the microporous coordination frames provide wide channels. Yaghi et al. (2004) and Ferey et al. (2005) explained MOF sequences by studying the combination of carboxylate ligand and di-valent (Cu^{2+}, Ni^{2+}, Zn^{2+}), tri-valent (Fe^{3+}, Cr^{3+}, V^{3+}, Sc^{3+}) metal ions. However, Louise et al. (2006) reported that there are rare studies on trivalent p-block elements such as Al^{3+}, $In^{3+,}$ Ga^{3+}.

MOFs can be synthesized by using various types of benzene organic linkers (Chen et al., 2011; Rowsell et al., 2005). The organic linkers consisting of carboxylate groups can make many different and strong bonds with metal cations. The MOFs consisting of carboxylate ligands have better catalytic performance, higher surface area, and larger pore size (Gascon; 2009). The versatile carboxylate ligands have good oxygen donating properties. These are spacers suitable for forming a MOF network. The BTC linker in particular is widely preferred to occur bridging ligands for MOFs. BTC ligand with two carboxylate groups at 120° angle has a rigid, planar molecule

structure. It can also exhibit hopeful properties for potential applications (Janiak et al., 2010). The geometry of 1,4-benzene dicarboxylic acid (BDC) is very close to a rod-like structure (Chen et al., 2011; Rowsell et al., 2005). Since conjugated carboxylate groups with aromatic rings consist of strong π-π interactions, they are straightforwardly bonded with metal ions and form MOF structures with high strength (Rowsell et al., 2005; Horike et al., 2013). Thus, it can simultaneously bind four metal ions, make long bridges by the benzene ring, and in this way cause a wide variety of structures (Janiak et al., 2010).

Carboxylate functional groups have multi-terminal ligands. These cause limitless structural variety by forming the maximum coordination bond with the metal ion. So, it offers permanent porosity and a very stable structure for MOFs. On the other hand, they provide the opportunity to be used in various potential application fields such as gas separation-storage, catalysis in organic synthesis, and biomedical (Ma et al., 2009).

2.3.6. MOF synthesis methods

MOF structures can be obtained using diverse benzene organic ligands with different ring numbers. Different techniques such as RT, ST, HT, US, EC, and MW can be used to synthesize the MOF (Burgaz et al., 2019).

1) HT method

The single crystals can be synthesized with the help of the dissolubility of minerals in heat water and under excess pressure. It can form crystal structures that are unstable at melting point (T_m) about crystal growth with the HT technique. Besides, these structures with approximate T_m and ideal vapor pressure can be synthesized. A wide range of quality crystal materials is obtained with this technique. However, it is costly and a very difficult process to observe crystal growth (Livage et al., 2001).

2) ST method

ST method is a process based on a very long reaction time. For this reason, several days are needed when using this method. But it is of great importance for the

industrial application of MOFs. Also, the ST method is similar to the HT method (Eddaoudi et al., 2002).

3) RT method

MOF structures with thermally stable, high yield, and high porosity nanocrystals can be synthesized in short reaction times (~0.5h) *via* by RT method (Tranchemontagne et al., 2008).

4) US method

This method is fast and easy to prepare. It is mostly favored in various research application fields such as waste handling, biodegradation of cells, welding, imaging, drug, and food industries (Safarifard and Morsali, 2015).

5) MW method

The MW method has many features such as ecological, simple, short-time reaction, high energy efficiency, reproducibility, faster kinetics, phase selectivity, and rapid heating (Choi et al., 2008).

6) EC method

This method is an effective and simple method and the yield, surface morphology, and pore size of MOF are controlled by this method. It has a great benefit industrial aspects. There is no need to use metal salts and reproducibility is provided by this method. It is based on the synthesis mixture in which it has occurred the anodic dissolution of the metal ion containing the organic linker and an electrolyte. It can be carried out in a partly short time at room temperature by electrochemical synthesis and it can be applied an efficiently and easily method without requiring oxidizing/reducing agents (Joaristi et al., 2012).

2.3.7. Application areas of MOFs

MOFs include extensive application fields such as gas storage-separation, receptor, material surface adsorption, drug release, ion-exchange, catalysis, chromatography optical, and magnetic substance. On the other hand, these materials are widely used in electrochemical capacitors and lithium-ion battery application fields (Burgaz et al., 2019).

2.3.7.1. Use of MOFs as an electrode in Li-ion rechargeable batteries

When the Li-ion battery is discharged, Li^+ ions in the negative electrode with the help of an electrolyte go towards the positive electrode. The lithium ions return when charging. Along the charge-discharge process of the Li-ion cell, lithium ions are introduced into (intercalate) the layered electrode materials, and these ions are removed (Dhawa et al., 2017; Xu, 2004; Tarascon and Armand, 2001). In Li-ion battery applications, it uses intercalated lithium compound at the cathode and typical graphite material at the anode (Tarascon and Armand, 2001). Nano-structured carbon-based materials (graphene, graphite, etc.) have been broadly studied with lithium alloys and transition metal oxides (Fe_2O_3 (ferric oxide), Co_3O_4 (cobalt oxide), TiO_2 (titanium dioxide), MnO_2 (manganese dioxide), NiO (nickel oxide), SnO_2 (tin oxide) and WO_3 (tungsten trioxide)) as an anode in Li-ion cell application. Transition metal oxides made of nanoparticles have higher specific capacitance than that of graphite material (Poizot et al., 2000). On the other hand, thanks to the porous nanomaterials, more contact area is obtained at the electrode and electrolyte interface. Thereby, Li-ion diffusion is achieved with a very short path length. Ultrathin flexible graphene with high conductivity and metal oxide nanocomposite materials effectively cause to stop the volume expansion during the charging and discharging process (Paek et al., 2009).

The most important feature of MOFs is their structure adjustability by a proper selection of various functional group linkers and metal centers, depending on the applications (Yang et al., 2010; Eddaoudi et al., 1999; Furukawa et al., 2010). To be able to intercalate lithium ions to layered electrode materials and at the same time remove (deintercalation) these ions, MOFs (due to their properties such as porous, uncoordinated regions and functionality of organic linkers) have been used in lithium-ion battery electrode materials (Cheng et al., 2003; Huang et al., 2002).

MOFs are capable of capturing mark contents of contamination in the system/byproducts when they working because of their high certain surface area. Due to this ability, it can prevent layer formation, increase internal resistance, and delay electrode reactions. Thus, the desired protection is provided on both electrodes (Fu et al., 2016). MOF structures with natural porous textures may be a suitable candidate in Li-ion cell application as electrode materials. MOFs, which are crystalline porous

materials, have been used as anode materials for the new class of electrode materials emerging in lithium-ion battery applications since 2006 (Cheng et al., 2006).

2.3.7.2. Electrolytes in Li-ion rechargeable battery

The transport process of lithium ions between cathodes and anodes takes place through SPEs. Composite polymer electrolytes consisting of the polymer host, inorganic supplement, and Li-salt containing organic solvent were reported by Steele and Weston in the 1982 year. However, their value was understood technologically as early as 2000. The purpose of using SPEs in lithium batteries is to enhance ionic conductivity, mechanical stability, high energy density, electrolyte leakage, and flexible geometry and to improve a lack of structural integrity. A wide variety of additives such as inorganic filler have been mixed into polymer electrolytes to improve the performance of high-energy electrical devices (Stephan, 2006; Polu and Rhee, 2017; Suriyakumar et al., 2016). By mixing nanoparticle materials such as Al_2O_3, SiO_2, and TiO_2, etc. into SPEs, the stability of SPEs is increased and the dendrite formation and degradation are hindered. NCPEs prepared with MOF used as a filler material exhibit good mechanical strength, ionic conductivity, thermal resistance, high lithium transference number, and better compatibility at high temperatures in electrical devices and hybrid electric devices (Gerbaldi et al., 2014; Fu et al., 2016; Wang et al., 2017; Angulakshmi et al., 2014).

2.3.8. Salts containing lithium

An ideal lithium salt electrolyte solvent used in Li-ion rechargeable batteries should have at least the below properties under suitable environmental conditions:

1) It must be soluble and degradable matter completely without the need for an aqueous environment. In an environment with a high ability of movement, the dissolved ions must be able to move without difficulty.

2) Anion ions must be resistant to oxidizing degradation at the cathode.

3) They must be inactive against organic solvents.

4) They must be inert against cell compounds such as electrode underlayer separative and packaging materials.

5) Anion ions must be free of toxic substances and they also must be inert thermally versus reactions caused by electrolyte dissolvent and other cell compounds.

Types of lithium salt used to prepare electrolyte solvents in electrolyte applications are limited according to broad spectra of proton-free organic components. This information is noted in a detailed document about anhydrous electrolytes improved in Li-ion rechargeable batteries by Dahn et al. (1991). According to the report, approx. 200 electrolyte solvent compounds were identified that compatible formulated with only 5 lithium salts out of 27 major solvents (Xu, 2004). The most basic lithium salts in a low dielectric medium cannot perform minimal solubility properties due to the lithium-ion has a small ionic radius. The oxides Li_2O and halides LiX (where X= chloride (Cl), fluoride (F)) are given as examples. Despite the increased solubility in anhydrous solvents named "soft Lewis base" (e.g. as bromide (Br^-), iodide (I^-), sulfur (S^{2-}), or carboxylates ($R–CO^{2-}$)) instead of anion, the anodic resistance of salt is enhanced. Because these anions can be easily oxidizing at values below 4.0 V against lithium on the loaded surfaces of cathode materials. Usually, lithium salts are formed from the combination of complex anions consisting of a stabilized elementary anion nucleus and Lewis acid substance. For instance, as a result of the complexation of the anion (F^-) of the lithium hexafluorophosphate with the Lewis acid PF_5, $LiPF_6$ salt is formed. Such anions are called super acid anions, they distribute properly the electro-negative ones with the strong electron-attracting Lewis acid linkers.

Corresponding to the complexation of salts, these salts generally are of fewer melting points than basic salts. They dissolve well in lower dielectric environments (Xu, 2004). In a family of lithium salts (e.g. $LiAlX_4$ (X=halides)) commonly preferred in prime Li-ion batteries, chemical inactivity requirement is excepted. Because AlX_3 Lewis acidities are high power, their complex formation with mild alkalies such as Cl^- cannot completely inactivate their affinity. For this reason, these attack most anhydrous solvents such as ethers. The AlX^{4-}anions lead to serious damage such as corrosion to other cell components. In addition to this, anions containing mild Lewis acids do not undergo any changes with organic solvents at ambient temperature and remain stable. There are different types of lithium salts (LiMXn) such as lithium perchlorate ($LiClO_4$), lithium borate ($LiBF_4$), lithium arsenate ($LiAsF_6$), lithium

phosphate ($LiPF_6$), lithium antimonates ($LiSbF_6$). The main physical properties of some salts including ion conductivity data are indicated as follow:

1) $LiClO_4$

The $LiClO_4$ has main physical properties such as molecular weight of 106.4 g, melting temperature of 236 °C, decomposition temperature in a solution of above100 °C, ionic conductivity values in PC, and DMC of $5.6x10^{-3}$ $8.4x10^{-3}$ at room temperature and it has no aluminum corrosion (Xu, 2004). This salt has sufficient solubility and high conductivity (~$9.0x10^{-3}$ S cm^{-1} in EC/DMC) at ambient temperature. It is also a widely used electrolyte solvent due to its large anodic stability of up to 5.1 V on the spinel structure of cathode surface in EC/DMC solvent (Tarascon and Guyomard, 1994). In recent studies on $LiClO_4$ electrolytes, it has been determined that solid electrolyte interface films formed on both surfaces of lithium and carbonaceous anodes have less impedance compare to $LiPF_6$ or $LiBF_4$ electrolytes. This situation is based on the use of HF. Because it was thought that it could react with Li_2CO_3 and form highly resistant LiF. $LiClO_4$ is slightly less hygroscopic and more resistant to media moisture according to the other lithium salts (Aurbach et al., 1995). The high oxidative state of Cl (VII) in ClO_4^- reveals its negative properties. Because it causes to react easily with many organic compounds under specified conditions like an extreme temperature and current load by making it a strong oxidant agent (Newman et al., 1980). In the past, it was reported that in the period corresponding to the 1970s, $LiClO_4$ salt as an ideal electrolyte solvent could not be used in industrial practical applications. Today, this salt is still used conveniently in a variety of laboratory applications because of its simple to use and inexpensive (Uchida and Sato, 1995).

2) $LiAsF_6$

The $LiAsF_6$ has a molecular weight of 195.9 g, melting temperature of 340 °C, decomposition temperature in a solution of above100 °C, ionic conductivity values in PC, and DMC of $5.7x10^{-3}$ $11.3x10^{-3}$ at room temperature. It has no aluminum corrosion (Xu, 2004). In general, $LiAsF_6$ is a superior electrolyte solvent in lithium batteries compared to $LiClO_4$. In lithium systems, its lithium cycling productivity can reach an average of > 95%. It was determined that when combined with $LiAsF_6$/2-Me-tetrahydrofuran (THF) solution, it changes color and chemical degradation occurs. It

was thought that it could perform a reaction between $LiAsF_6$ and solvent. The cathode balance of AsF_6^- anion on the surface of glassy carbon is 1.15 V versus Li. Also, the use of $LiAsF_6$ in a commercial battery is risky due to the high oxidation in any electrochemical reduction in As (V) (Xu, 2004). The stable in suitable solvents such as esters, up to 4.5 V on a variety of cathode faces. Anodic stability of the AsF_6^- anion is high. The conjunction of anode and cathode balance has limited the use of $LiAsF_6$ in both lithium cell and Li-ion batteries as it leads to toxicity (Tarascon and Guyomard, 1994). Therefore, Gnanaraj et al., (2001) indicated that the use of this lithium salt in commercial batteries is not permitted but is still applied in the laboratory.

3) $LiBF_4$

The $LiBF_4$ salt has basic properties such as the molecular weight of 93.9 g, melting temperature of 293 °C, decomposition temperature in a solution of above 100 °C, ionic conductivity values at room temperature in PC, and DMC of $3.4x10^{-3}$ $4.9x10^{-3}$. It has no aluminum corrosion (Xu, 2004). Similar to $LiAsF_6$ salt, $LiBF_4$ salt is an inorganic superacid and anion-based salt. There is a mild ion conductivity in anhydrous dissolvents. Electrochemically, it has been observed that the BF_4^- anion is stable to lithium at about 5.0 V, while it is stable up to 3.6 V against oxidation at the glassy carbon surface versus a standard calomel electrode. When this salt was used in lithium battery research, the number of cycles decomposed rapidly and it has lead to weak lithium cycle efficiency. When this salt was used in lithium battery research, the number of cycles decomposed rapidly and it has lead to weak lithium cycle efficiency. The researchers concluded that $LiBF_4$ salt contained less toxicity than $LiAsF_6$ salt. Also, they stated that it is less risky than $LiClO_4$ salt (Takata et al., 1985). However, it is prevented its use in Li-ion batteries by the reason of its negative features such as its moderate ion conductivity, hydrolysis, and thermal unstable (Hofmann et al., 2013).

4) $LiPF_6$

The $LiPF_6$ salt has some features such as the molecular weight of 151.9 g, melting temperature of 200 °C, decomposition temperature in EC/DMC solution of about 80 °C, ionic conductivity values in PC and DMC of $5.8x10^{-3}$ $10.7x10^{-3}$ at room temperature. It has no aluminum corrosion (Xu, 2004). Among the many salts used for Li cell and Li-ion batteries, the $LiPF_6$ salt has been commercialized due to its

advantageous properties (Xu, 2004). Compared to other salts, $LiPF_6$ salt is widely used in Li-ion batteries from the point of view of its positive features regarding Li mobility, electrochemical equilibrium, ionic conductivity, and interface of solid electrolyte formation on a graphite electrode. However, besides its positive properties, $LiPF_6$ salt has negative properties such as being highly toxic, sensitive to moisture, decomposing into toxic products, and thermal instability. For example, $LiPF_6$ salt has been decomposed above 60 °C and thus its use in the application area of the Li-ion battery was limited (Hofmann et al., 2013). Therefore, academic and industrial researchers have searched for alternative salt that can be used in place of $LiPF_6$ salt. They reported the LiTFSI salt as a candidate. Therefore, academic and industrial researchers have searched for alternative salt that can be used in place of $LiPF_6$ salt. They reported the LiTFSI salt as a candidate (Borgel et al., 2009; Salminen et al., 2006).

5) LiTFSI

The LiTFSI salt has a molecular weight of 286.9 g, melting temperature of 234 °C, decomposition temperature in a solution of above100 °C, ionic conductivity values in PC, and DMC of $5.1x10^{-3}$ $9.0x10^{-3}$ at room temperature. This salt is affected by aluminum corrosion (Xu, 2004).

It is also known as lithium bis(trifluoromethanesulfonyl)azanide (LiTFSA) in the literature (Wilson et al., 2007). Sato et al., (2004) reported that N, N-diethyl-N-methyl-N-(2-methoxyethyl)ammonium (DMMA) – TFSI anion can be preferred in a Li-ion based cell (Sato et al., 2004). In lithium battery applications, it has been thought that LiTFSI salt could be used instead of other salts and commercialized by the 3M company in the early 1990s, as $LiClO_4$ salt is dangerous, $LiBF_4$ and $LiPF_6$ salts are thermally unstable, and $LiAsF_6$ salt is toxic (Webber, A. (1991). It has been reported that LiTFSI salt is a risk-free, thermally stable, and highly conductive material (Hofmann et al., 2013). On the other hand, a Li-ion cell based on lithium nickel oxide cathode and petroleum-based anode without Al has been reported to provide up to 1000 deep discharge cycles with LiTFSI in an EC/DMC liquid. When electrochemical stability analyzes were performed on the surface of a glassy carbon electrode, it was found that the $TFSI^-$ anion is stable up to 2.5 V versus the Ag^+/Ag reference in EC/DMC against oxidation and the oxidation limit versus Li is about 5.0 V. When the LiTFSI salt was applied to lithium-ion cells containing Al, the $TFSI^-$ anion interacted

with Al^{+3} to form $Al(TFSI)_3$ components. This caused serious Al corrosion. For this reason, LiTFSI salt could not be utilized for commercial Li-ion cells. But, today, it is still being studied with the LiTSI salt, especially for polymer-based electrolytes.

The ionic mobility and constant degradation magnitude of these salts are given below, respectively (Ue, 1994).

$LiBF_4 > LiClO_4 > LiPF_6 > LiAsF_6 > LiTFSI$ (1)

$LiTFSI > LiAsF_6 > LiPF_6 > LiClO_4 > LiBF_4$ (2)

The oxidation (redox) potential order of salts is given below (Hofmann et al., 2013).

$LiPF_6 > LiBF_4 > LiTFSI > LiClO_4$

The stability order of the anions of these salts is given below (Ue et al., 1997).

$AsF_6^- > PF_6^- > BF_4^- > TFSI^- > ClO_4^-$

At room temperature, the degradation voltage of electrolytes is given below (Guyomard and Tarascon, 1995).

$ClO_4^- > TFSI^- > AsF_6^- > PF_6^- > BF_4^-$.

3. MATERIALS AND METHOD

Terephthalic acid (H_2BDC, $C_8H_6O_4$, 98%), tetrabutylammonium tetrafluoroborate (TBATFB, $(CH_3CH_2CH_2CH_2)_4N(BF_4)$, 99%), N,N-dimethylformamide (DMF), methanol (CH_3OH, 99.8%) magnesium ribbon (99.5%), LiTFSI, acetonitrile (CH_3CN, 99%) and PEO (M_v=600,000 g mol^{-1}) materials were bought from Aldrich company.

3.1. Synthesis of Nanosized MgBDC MOF

The electrochemical method (EC) was used in the synthesis of nanosized MgBDC MOF. For the synthesis, terephthalic acid (5,25 g) and TBATFB (4,11g) were dissolved into 200 ml DMF in a 250 ml beaker, and methanol was added into this solution. After that, it was mixed at ambient for 30 min. The magnesium ribbons were polished with sandpaper before use as shown in Figure 3.1, and then the electrochemical synthesis was performed by using magnesium ribbon as an anode and cathode in this solution. The electrolysis was carried out in an electrochemical cell under 3 Volt (V, joule/coulomb, J/C) and 9.5 milliamperes (mA, coulomb/second) direct current (DC) for 72 hours with no stirring during the whole reaction time as demonstrated in Figure 3.2. The blurry solution was soaked three times 120 ml of DMF solvent on the first day and then 100 ml of methanol twice two days. In total, this washing process was performed for three days and the solid particles were collected from this blurry solution. The obtained solid precipitates were dried in a vacuum oven at 120°C for 24 hours. The reaction efficiency was calculated as 81%.

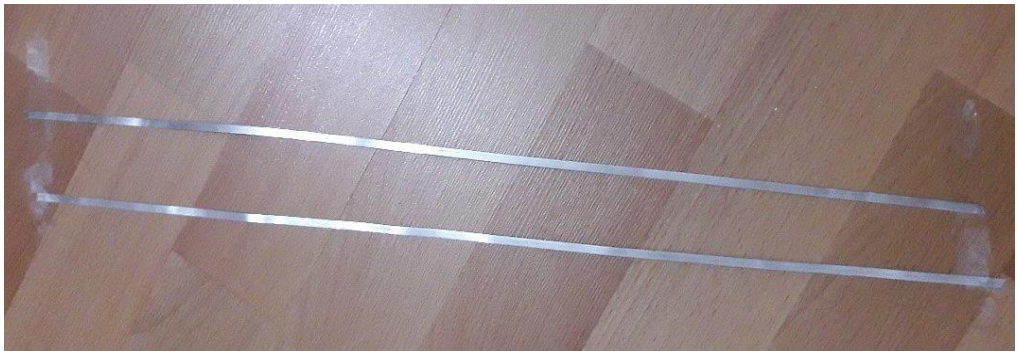

Figure 3.1. Digital photograph of polished magnesium ribbons

Figure 3.2. Experimental setup of nanosized MgBDC MOF synthesis via the electrochemical method

Percent yield (%) calculation of nanosized MgBDC MOF

The yield % of MgBDC MOF nanoparticles was calculated according to the equation number (3.1) below:

$$\%\, Yield = \frac{Actual\ Yield}{Theoretical\ Yield} \times 100 \qquad (\mathbf{3.1})$$

Before synthesis, the weights of the first and second magnesium ribbons were computed to be 0.8324 g and 0.8304 g, respectively. After synthesis, weights of the first and second magnesium ribbons were 0.7506 and 0.8608 g, respectively as demonstrated in Figure 3.3. While the nanoparticle MOFs were synthesized, oxidation-reduction reactions occurred in the anode and cathode systems as shown below.

$$Mg^{2+} + 2e^{-} \longrightarrow Mg \text{ (reduction)}$$

$$Mg \longrightarrow Mg^{2+} + 2e^{-} \text{ (oxidation)}$$

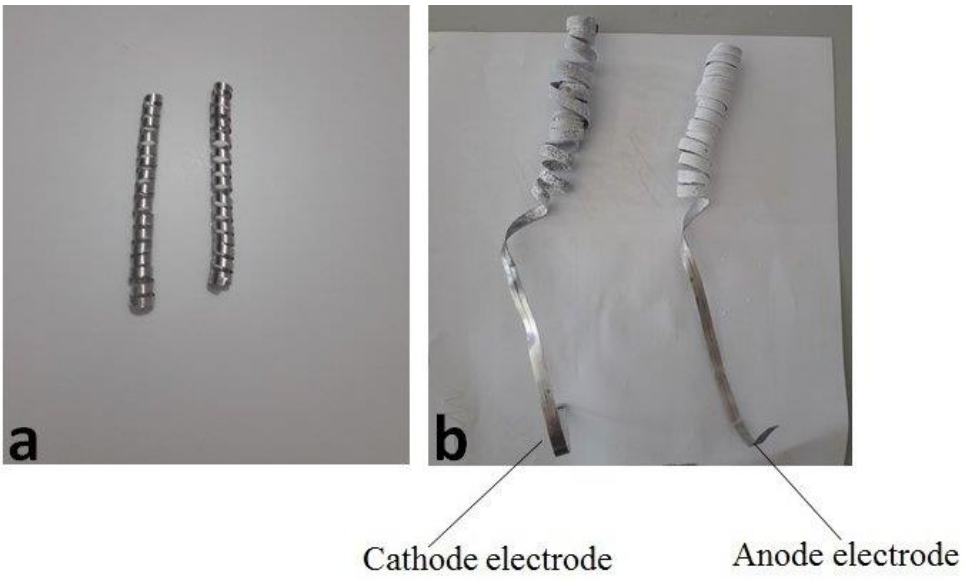

Figure 3.3. a) Magnesium ribbons before synthesis, b) after synthesis

Therefore, the weight loss occurred in the first magnesium ribbon due to the reduction reaction after synthesis and it was understood that this ribbon was the cathode. The second magnesium ribbon, on the other hand, increased in weight due to an oxidation reaction after synthesis, and thus it was determined to be the anode. The process was continued based on the cathode electrode.

The weight difference in magnesium cathode electrode:

$$0.8324 - 0.7506 = 0.0818 \text{ g}$$

The amount of experimentally obtained MgBDC MOF nanoparticles was found to be 0.5137 g. The reaction that occurs when Mg and H_2BDC react is given below.

$$Mg^{2+} + H_2BDC \longrightarrow MgBDC + 2H^+$$

According to this reaction, the molecular weight (M_w) of the BDC component formed when the two hydrogen atoms produced in the products are substracted from the M_w of H_2BDC is calculated as follows.

$$H_2BDC_{\text{mol. weight}} = 166.13 \text{ g/mol}$$

$$H_{\text{mol. weight}} = 1 \text{ g/mol}$$

$$BDC = H_2BDC_{\text{ mol. weight}} - 2H_{\text{ mol. weight}} = 166.13 - 2 = 164.13 \text{ g/mol}$$

$$Mg_{\text{ mol. weight}} = 24.312 \text{ g/mol}$$

In this case, the total molecular weight of MgBDC MOF;

$$\text{MgBDC MOF}_{\text{mol. weight}} = 24.312 + 164.13 = 188.42 \text{ g/mol}$$

In the light of this information, the theoretical yield of MgBDC MOF was calculated as given below:

24.312 g/mol Mg		188.442 g/mol MgBDC MOF
0.0818 g Mg cathode	?	g MgBDC MOF

$? = 0.633$ g Mg BDC MOF

The amount of MgBDC MOF nanostructures obtained in the synthesis was previously weighed as 0.5137 g. This also corresponds to real efficiency. Finally, the yield calculation (%) of the electrochemical synthesis according to the equation numbered (3.1) stated above was found to be 81.153%.

$$Yield\% = \frac{Actual\ Yield}{Theoretical\ Yield} \times 100 = \frac{0.5137}{0.633} \times 100 = 81.153\ \%$$

3.2. Preparation of PEO Based SPEs and NCPEs

Following is done for the production of PEO based SPE and NCPE membranes according to the ratios and code names indicated in Table 3.1:

Firstly, PEO, LiTFSI, and nanosized MgBDC MOF materials were activated at 50°C, 100°C, and 180°C, respectively, under vacuum before anything is done. PEO-based solid polymer electrolytes (PEO-based SPEs) were produced by dissolving a certain amount of PEO and LiTFSI in acetonitrile for 24 hours at 50 ° C in a 25 mm glass bottle and then put in glass Petri dishes after 30 minutes of ultrasonication bath treatment.

Similarly, the same method has been used in the production of PEO-based NCPE membranes consisting of nanosized MgBDC MOF. The mix of PEO, lithium salt, and nanosized MgBDC MOF was stirred in acetonitrile for 24 hours at 50 ° C in a 25 mm glass bottle and then put in glass Petri dishes after 30 minutes of ultrasonication bath treatment. After the casting process, PEO-based SPE and NCPE membranes were kept

to dry for 48 hours at room temperature, and then they were made dry in a vacuum oven at 30 ° C for 1 day at room temperature to take out moisture from SPEs and NCPEs. These membranes were kept waiting for storage in a glove box previous to characterization processes. The production process of PEO-based SPEs and NCPEs is shown in Figure 3.4.

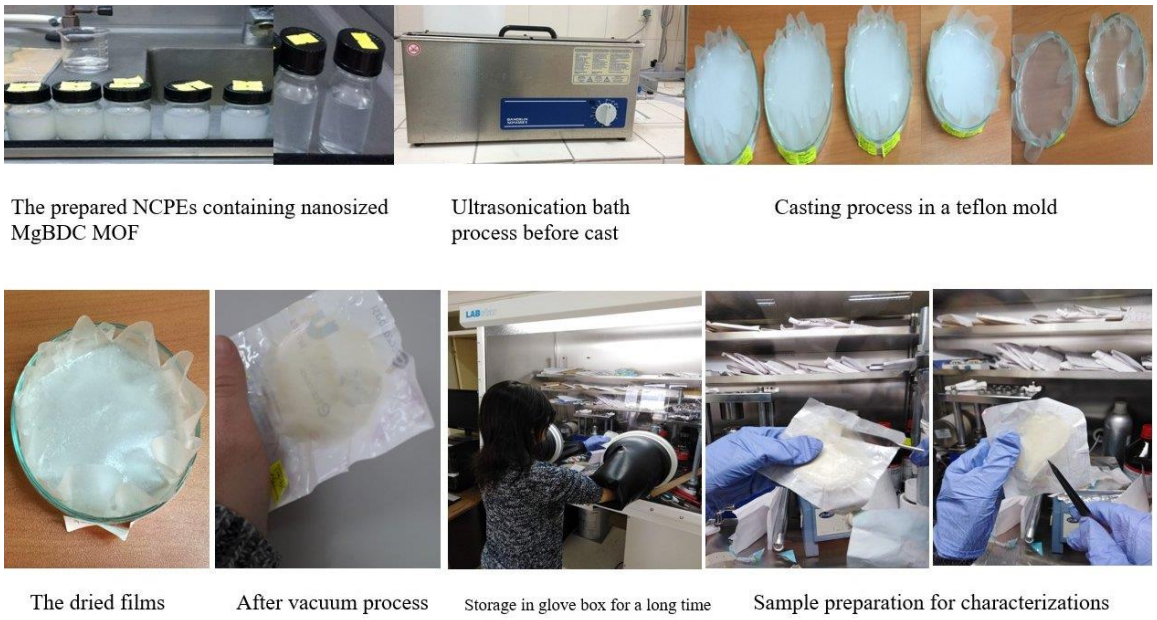

Figure 3.4. Preparation processes of nanocomposite polymer electrolytes consisting of MgBDC MOF

Table 3.1. The percentage rations and code names of PEO based SPE and PEO based NCPE membranes containing MgBDC MOF

Sample code name	PEO (wt %)	LiTFSI salt (wt %)	MgBDC MOF nanoparticles (wt %)
PEO	100	0	0
15Li	85	15	0
20Li	80	20	0
2Mg-15Li	83	15	2
5Mg-15Li	80	15	5
2Mg-20Li	78	20	2
5Mg-20Li	75	20	5

3.3. Characterization Techniques

3.3.1. ATR FT-IR spectrometry

The ATR FT-IR spectrometry analyses were carried on by using a Bruker Tensor 27 type spectrometer (US). The specimen surfaces were displayed in the 4000-400 cm^{-1} range. The spectra were made a record at ambient temperature. The background check and baseline validation were performed.

FT-IR is based on the vibration principle of chemical bonding between particles forming the matter and corresponds to frequency. These vibration frequencies show the specific fingerprint along with absorption peaks for each specimen. The fingerprint region is the part after 2000 cm^{-1} wavenumbers. The spectrum of this region is taken in more detail by doubling it. Certain infrared rays are absorbed through the specimen and the rest of them are transmitted by passing through the specimen.

All different types of matter are formed by a combination of atoms. Therefore, the infrared spectra of two different compositions always occur in different IR spectrums. It is characterized to determine the organic-inorganic chemical composition of various substances. FT-IR is a fast, reliable, and inexpensive technique. By the FT-IR technique, unknown bondings in the material structure can be found, the amount of the component in a mixture can be known, the quality or consistency of a sample can be studied and rapid results can be obtained without damaging the sample (Figure 3.5).

The molecules have three general types of motion: translation, rotation, and vibration. Polyatomic molecules have more complex vibrations called normal mode while diatomic molecule has a single type of motion. There are two types of vibration modes in the IR spectrum. These are the stretching (υ) and bending (δ) vibration modes. The stretching (υ) vibration modes are of two types, asymmetric stretching (υ_a) and symmetrical stretching (υ_s) vibrations. It can also be written as asymmetric-symmetrical stretching (υ_{as}) vibrations while saying the two together. There is an asymmetric (δ_a), symmetric (δ_s), asymmetric-symmetric (δ_{as}) relationship in terms of geometrics for bending (δ) vibration modes, respectively. Besides, scissoring, rocking, wagging, and twisting bending vibration have four types of bending vibration modes. The molecular bonds have vibrations at different frequencies based on the variety of elements and bonds. There is some characteristic frequency that can give vibration in

any bond. The lowest frequencies refer to the ground state and higher frequencies refer to several excited states in quantum mechanics. To increase the molecular vibration frequency, the molecular bond absorbs the energy of light. In any transition between the two situations, the energy of light examined by the wavelength should be equal to the difference in the energy between the two situations. The energy-related to these transitions between molecular vibration has usually 1-10 kcal/mol and is expressed as the infrared of the electromagnetic spectrum. The data obtained is usually plotted as a function of the absorbance (A) or transmittance (T) against wavenumber. The transmittance and absorption are converted logarithmically as follows: $A=\log (1xT^{-1})$. The peak size occurring in the spectra has a direct relationship with the content of available material. It is possible to perform infrared analyzes with appropriate software algorithms for quantitative analysis.

Analysis of solid and liquid samples has been made more powerful recently by the ATR technique. As shown in Figure 3.6, when the ray makes contact with the specimen, the changes are observed in the internally reflected IR beam. In this case, these changes that occur are studied by the ATR apparatus. IR beam with a certain angle and ideal refractive index is transmitted to optically intensive crystal. Thus, the internal reflection of the specimen in contact with the crystal occurs temporal wave.

Figure 3.5. ATR FT-IR spectroscopy

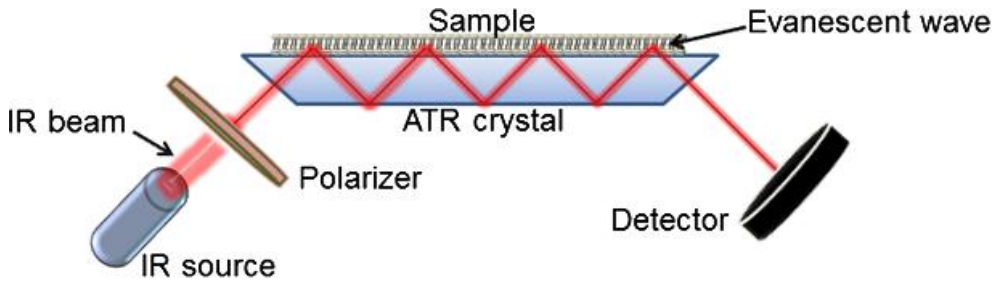

Figure 3.6. Schematic representation of an ATR-FT-IR system (Ausili et al., 2015)

3.3.2. TGA analyzer

Thermal degradation of MgBDC MOF nanoparticles and PEO-based films was measured using a TA Instruments Q600 Simultaneous Differential Thermal Analysis as given in Figure 3.7. The specimens were warmed in alumina pans temperatures between 20 and 1000°C with a heating rate of 20°C/min under nitrogen gas flow. An empty alumina pan was utilized as a reference in each analysis.

TGA includes methods of measuring the change in the physical properties of materials such as weight, absorbed or released heat, size, conductivity, magnetic property of materials by heating or cooling materials. It identifies the quantity and ratio of change in the weight of the material as a function of temperature and time in a controlled atmosphere. So, the thermal stability of materials, polymer-polymer or polymer-additive interactions, moisture in the material, and the ratio of volatile components or additives are determined. It determines the composition of materials and predicts thermal stability. It can characterize substances that lose weight and gain weight because of the degradation. The weight loss and weight gain constitute the weight change mechanism of TGA. In the weight loss, degradation by the breakdown of chemical bondings, vaporization with the loss of volatiles at high temperature, and decrease of the specimen with a decreasing atmosphere interaction occur. In the mechanism of weight gain; oxidation reaction occurs due to the interactivity of the specimen with an oxidative atmosphere. In addition, as the heat passes through the sample, the sample absorbs the heat, and absorption fact occurs. Events occurring in both mechanisms are kinetic processes.

Figure 3.7. TGA apparatus

3.3.3. XRD analyzer

Nanosized MgBDC MOFs and NCPEs of XRD phase analyses were studied with x-ray diffractometer apparatus RIGAKU SMART LAB, Japan. The analyses were done at 40 kV and 30 mA by CuKα radiance and zero background specimen holder. The step size of 0.02° and data collection period of 1 s in each step was performed for all analyses. K-β peaks were repressed using a monochromator. XRD lines were measured using the Rietveld method and PDXL2 software from Rigaku. The data of crystal structure parameters were taken from The Cambridge Structural Database (CSD) (Kaduk, 2002). It is based on Joint Committee on Powder Diffraction Standards (JCPDS) card, number: 54-2162 (Huang et al., 2014). The atomic coordinates, backplane, profile figure shape, scale, and lattice factors were improved.

X-rays are high-energy and low-wavelength electromagnetic radiation, but the X-ray wavelength is much shorter (0.1 nm) than visible light. It is formed when high-speed electrons hit atoms of the target material. This technique is a non-destructive analytical method utilized to determine crystal phases that may appear in substances such as powder, polycrystal. It also determines structural properties such as defect structure, epitaxy, grain size, composition, and preferred orientation. Diffraction patterns provide important information about the crystal structure of matter. When the X-ray beam hits any solid material, some of that the beam is scattered all over with the electrons associated with each atom or ion in its path. This scattering is called

diffraction. Diffraction occurs from scattering involving a large number of atoms. According to Braggs' Law, as given in equation number (3.2), planes in a crystal are exposed to a radiation source at an incident angle of reflection equal to the theta (θ).

$$n \times \lambda = 2d \times (sin\theta) \quad \textbf{(3.2)}$$

As seen in Figure 3.8, there are two parallel atomic planes with a distance of about *d* between them. It is assumed that a parallel and coherent x-ray beam with wavelength (λ) hits these two planes at a theta (θ) angle. The two rays in this beam, represented by the letters A and B, are scattered through the atoms P and Q. The difference of the distance traveled by the rays A' and B', scattered by theta (θ) angle, is equal to the product of their wavelengths by an integer *n*. The difference of the distance traveled by these rays is SQ + TQ and is expressed using the diffraction condition equation (33).

$$n \times \lambda = \mathrm{SQ} + \mathrm{DQ} \quad \textbf{(3.3)}$$

$$n \times \lambda = dsin\theta + dsin\theta \quad \textbf{(3.5)}$$

$$n \times \lambda = dsin\theta + dsin\theta = 2\, dsin\theta$$

where, *n*, λ, and *d* are stated as the diffraction constant, wavelength, the distance between planes, respectively. This equation describing x-ray wavelength and the distance between atoms by the angle of the diffracted beam is known as Bragg's Law. The digital photograph of the XRD apparatus is given in Figure 3.9.

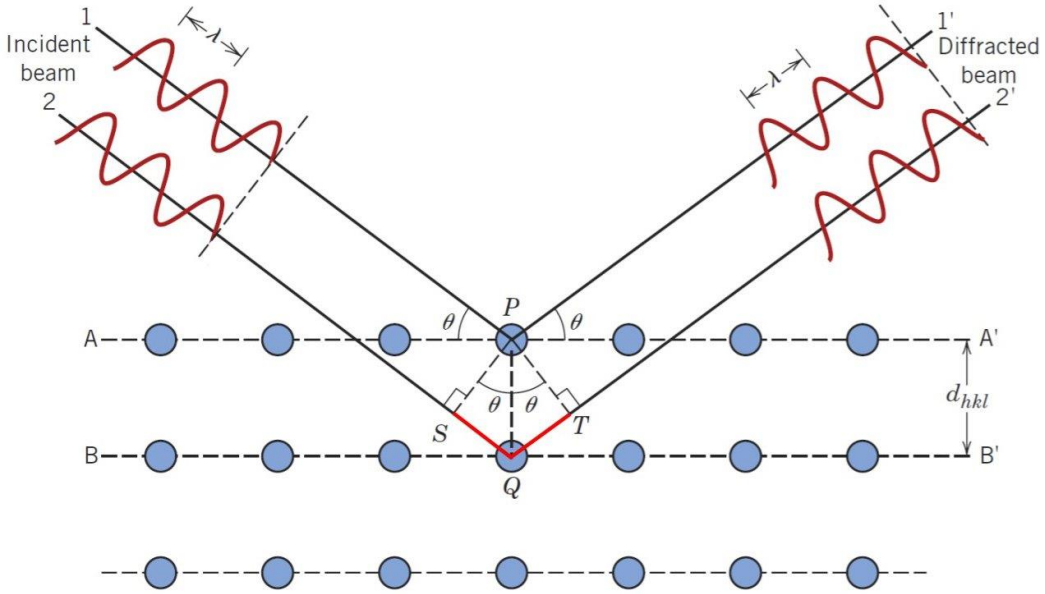

Figure 3.8. The principle of the X-ray diffraction technique (Gawas et al., 2019)

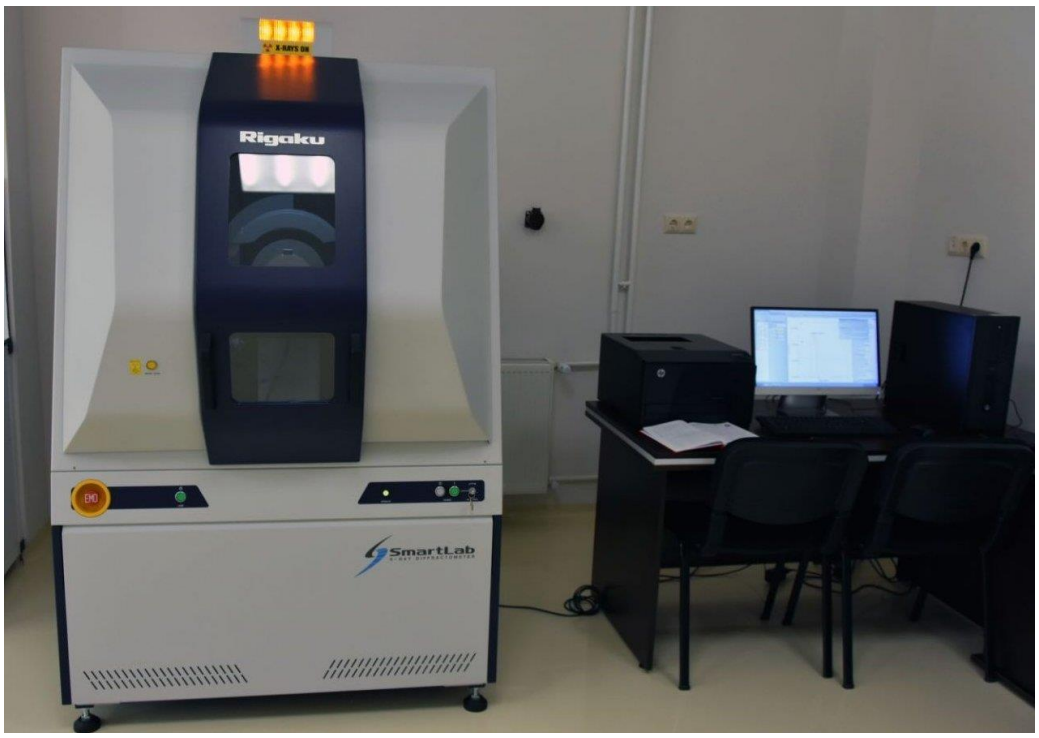

Figure 3.9. The digital photograph of the X-ray diffractometer apparatus

3.3.4. SEM / STEM / EDS techniques

In the scope of this thesis, the morphology and surface images of nanosized MgBDC MOF powders and NCPEs were examined by using SEM (JEOL-JSM-7001F endowed with STEM and EDS). In addition, EDS analysis was performed to identify and map the elemental components of a point or region on the sample. SE detecter, high vacuum mode, and 5-15 kV speeding voltages were studied along with the experiment with EDS as shown in Figure 3.10.

In the SEM technique, the surface of the specimen is focused with the help of an electron beam and then this surface is scanned and the micro image was taken. The electrons by interacting particles in the specimen produce various signals that report about the topography and compound of the specimen surface. The surface of the specimen is scanned by using an electron beam together with the cellular detection scheme. When the location of the electron beam is detected with signaling, it creates a display by matching it. A higher resolution of over 1 nanometer is acquired by this analysis technique. Normal SEM instruments are proper for studying high vacuum, conducting, and drying surfaces. Also, there are instruments with superior features that can work in humid states, low vacuum, and very low and high temperatures.

Figure 3.10. The digital photograph of SEM apparatus

The analysis is performed by sending an electron beam on the sample instead of light in the SEM system. This system has three main sections a specimen, optical colon, and viewing as demonstrated in Figure 3.11. In the optical column section, there is an electron pistol from the electron ray, an anode slub that is applied high voltage to speed the electrons towards the specimen, a magnetic lens to gain a thin electron ray, and finally scanning coils to scan the sample surface of the electron beam. All of the optical columns are kept at 10^{-4} Pa. In the imaging system, some detectors collect various electrons and radiations generated as a result of the sample inlet with the electron beam. This apparatus usually uses two types of radiation signals for imaging, primary and secondary electrons. Primary electrons are backscattered while secondary electrons are removed from the material. The backscattered electrons report on the composition and microstructure of the specimen. The secondary electrons show details about the sample surface.

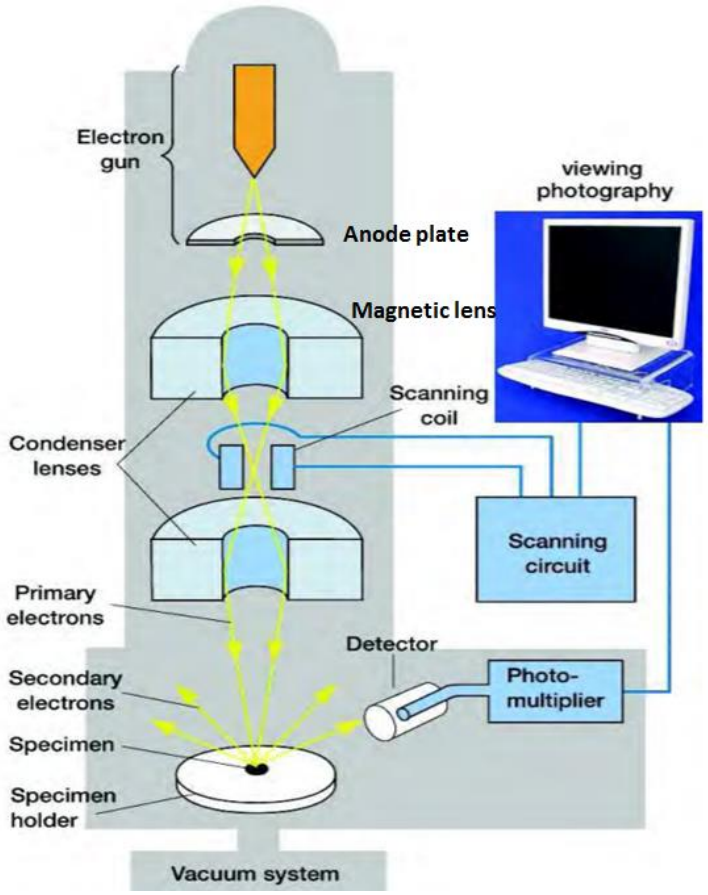

Figure 3.11. The schematic diagram of SEM apparatus (Karan et al., 2015)

3.3.5. AFM analyzer

The topography of the specimen was measured using AFM apparatus (NT-MDT NEXT, Russia) as given in Figure 3.12. The measurements were performed by the tapping mode and a silicone-type sweep. It was determined in semi-contact mode and scanning velocity of 1 Hz. It was done on a specimen scope of 1.8μm × 1.8μm. The analyses were performed at ambient temperature.

Surface morphology and 3D surface topography of materials and thin films are determined with AFM apparatus. It is used to determine various surface properties (friction, surface morphology, and roughness, tribological properties, atomic-level surface forces, etc.) of all kinds of solid materials such as ceramic, metal, polymer, semiconductor, biomaterial. It is also used to obtain physicochemical surface properties of nanoscale structures and nanomaterials.

Figure 3.12. The digital photograph of AFM apparatus

3.3.6. BET analyzer

BET surface area tests were worked at 77 K using nitrogen gas by Quantachrome NOVA 4200e Adsorption Analyzer as shown in Figure 3.13. The surface area of nanosized MgBDC MOF powder was computed with the BET equation.

BET analysis tries to express why gas particles are physically adsorbed on a solid surface. It is a crucial analysis method used to determine the characteristic surface of substances. The experimental data obtained are generally known as physical adsorption. This technique is used in multi-layer adsorption systems. It is preferable to use probe gases when determining the characteristic surface field of substances in this analysis. Care is taken to avoid the chemical interaction of adsorbent with the material surface.

Figure 3.13. The digital photograph of BET apparatus

3.3.7 DSC analyzer

The thermal attitudes of specimens were conducted with DSC using TA instruments Q2000 series (in Figure 3.14). Specimen of approximately 7 mg was put in an aluminum closed-box. It performed heating at temperatures between 25°C and 100°C at 10°C/min, after that cooling back to -90°C at 10°C/min and heating again at temperatures between -90°C to 100°C at 10°C/min. The information of the last cycle

was studied. A blank aluminum closed-box was as a reference. For this analysis, the purge gas was consumed from high-purity nitrogen gas provided at 50 mL/min.

Figure 3.14. The digital photograph of the DSC apparatus

The energy quantity absorbed or emitted during the heating-cooling or holding the specimen at constant temperature is determined by the DSC apparatus. It examines the variation in heat flow ratio (q, W/g) between a specimen and inert reference as a function of time and temperature. The relationship between specimen and reference temperature is as seen in Figure 3.15. When there is a temperature change between the specimen and reference, this temperature difference is brought into equilibrium by changing the energy quantity provided to the specimen. Thus, the content of heat transfer along phase modulation change in the specimen can be learned. The heating-cooling process is applied to a sample of known mass and in this case, the variations in heat capacity are observed as in heat flux. In this way, it ensured that the identification of transitions such as curing, melting points (T_m), glass transition temperature (T_g), and phase modulations as demonstrated in Figure 3.16. When the materials are processed or distilled, if heat capacity and enthalpy information of material are visible, it means your process is operating. DSC can define boiling points, T_g, T_m, and crystallization temperature (T_c), percent crystallinity (X_c %), time, specific heat capacity, fusion heat-reaction, oxidizing-thermal resistance, curing rate and curing degree, impurity, endothermic-exothermic reactions, etc. The percent crystallinity can be computed as in the equation given below (Gupta et al., 2016).

$$X_c\ \% = (\Delta H_m / \Delta H_m^{\circ}) \times 100 \qquad (\mathbf{3.6})$$

where ΔH_m is the melting enthalpy taken from DSC measurement and ΔH_m° is the melting enthalpy per gram of 100% crystalline polymer. During DSC measurement, endothermic and exothermic reactions occur because of the heat exchange as shown in Figure 3.17.

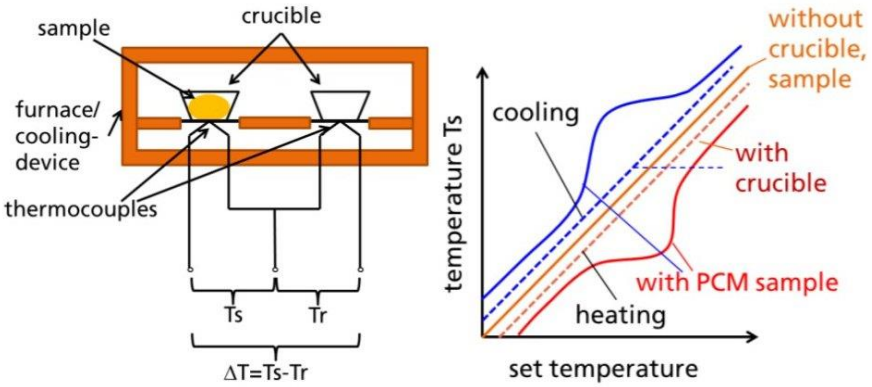

Figure 3.15. The operating principle of the DSC technique (T_s: sample temperature, T_r: reference temperature) (Gschwander et al., 2015)

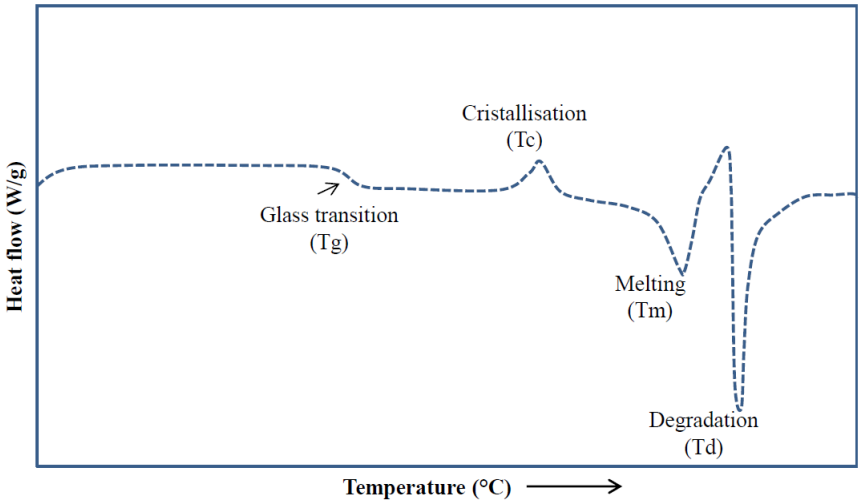

Figure 3.16. Schematic representation of thermal transitions in semicrystalline material obtained from DSC thermogram (Leyva-Porras et alk., 2020)

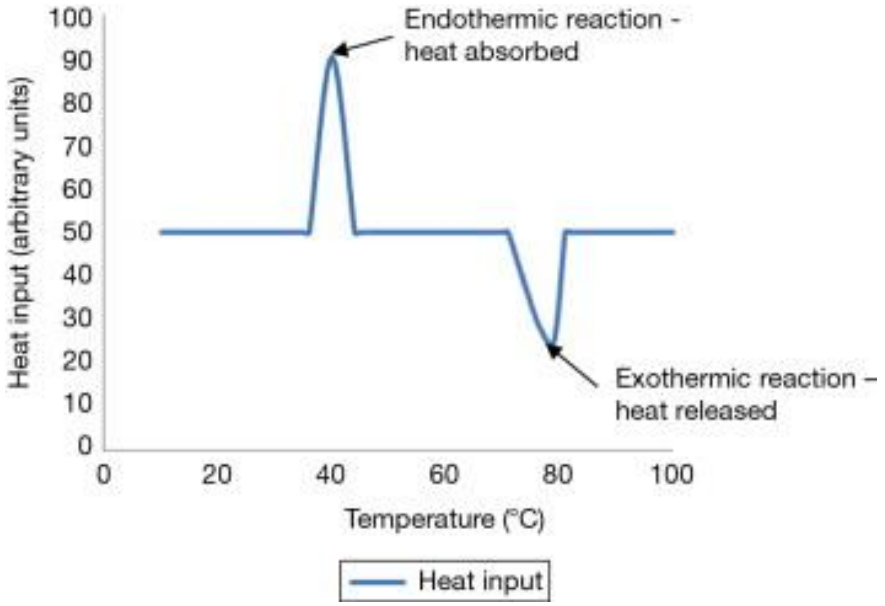

Figure 3.17. The sample undergoes both an endothermic and an exothermic reaction by DSC analysis (Siegel and Saukko, 2013)

3.3.8 POM analyzer

The polarized optical microscope images of specimens were studied on Leica DM4500 P optical microscopy with the help of aligning two polarizers and attaching a Linkam TP 94 hot plate (Figure 3.18). To observe crystallization in the specimens, firstly heating process was applied between 25°C and 100°C at 5°C/min after that cooling process to a rate of 2 °C/min to 50°C. Optical images were captured at magnitudes of ×10, ×20, ×50.

It provides the illumination of the sample with polarized light by this microscope. An experimental setup of an optical polarization microscope to view the field structure of a sample is shown schematically in Figure 3.19. The rule of POM is based on polarized light. A POM apparatus has two polarizers, horizontal and vertical. These are known as cross-polar as they are planned to be directional in a vertical angle together as seen in Figure 3.20. The polarizer is a filtering system that is directed only in a certain and allows light to pass through with the polarization direction. The polarization line of the first polarizer is directed perpendicular to the incident ray, for this reason, vertical waves can move through the filter. The waves that can pass

through are then hindered by the second polarizer. Because in this polarizer, the incoming waves are lined horizontally (see Figure 3.20). POM technique typically investigates the entity of liquid crystalline phases in a solution. In addition, the POM method is used to examine crystal structures, to show the grain boundaries, and to see more clearly the defects such as cracks, scratches, cracks, especially in mechanical processes.

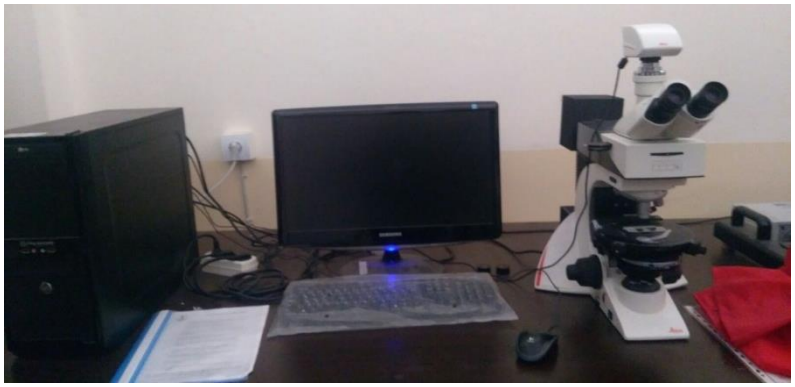

Figure 3.18. The digital photograph of the POM apparatus

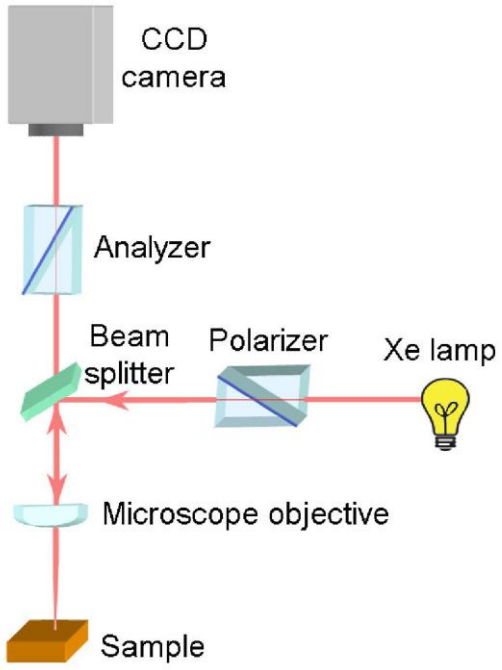

Figure 3.19. Schematic view of the optical polarizing microscope (Pashkevich, 2015)

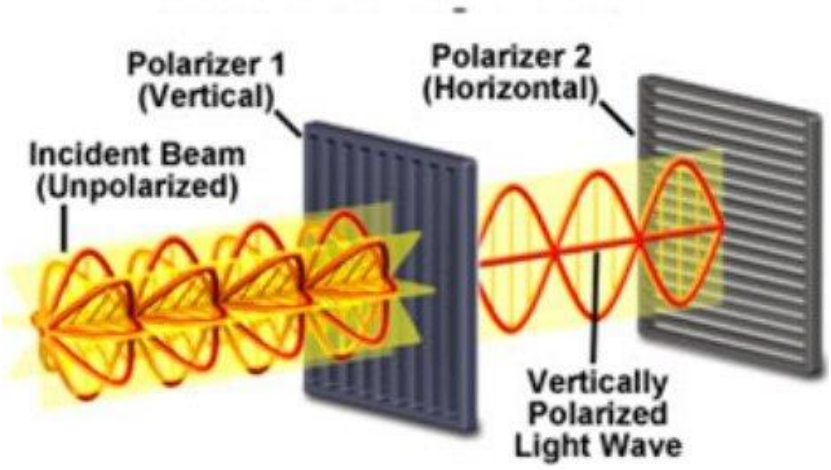

Figure 3.20. Types of the polarization of light waves (Nikon Corporation)

3.3.9 EIS analyzer

The ionic conductivity analyses of membranes sandwiched between two stainless steels (SS) blocking electrodes of 1 cm^2 area were done by the alternative current (AC, Hertz, Hz). A Gamry reference 600 potentiostat system in a frequency range from 50 MHz up to 100 kHz with an amplitude of 10 millivolts (mV) was used for the EIS measurement (Gamry Reference 600 device, Germany) (Figure 3.21). All analyses were conducted range from 30 to 60 °C.

In this study, the EIS device connected to a controlled temperature measuring device and computer was installed outside as shown in Figure 3.22. Ionic conductivity measurements of PEO-based SPE and NCPE films were made inside two aluminum metal-covered pans in ambient air. The electrodes inside the Teflon mold are designed to be 1 cm apart from each other. The prepared sample films were cut in 3 cm × 1 cm and the thicknesses of them were found separately for each and their thicknesses changed 80-130 μm.

These films were placed individually on the sandwich electrodes and then then they have left into aluminum metal-covered pans. In this way, the ionic conductivities of films measurements were made as shown in Figure 3.23. EIS analyzer contains empirical scripts for potentiostatic, galvanostatic, and hybrid impedance spectroscopy analyses as well as single-frequency methods. Also, it is measured physical-

electrochemistry methods such as cyclic voltammetry, chronoamperometry, and chronopotentiometry by EIS analysis. It is also determined many electrochemical properties such as pulse voltammetry, direct current (DC, Hertz) corrosion, electrochemical energy, electrochemical signal analyzer, electrochemical frequency modulation, critical pitting temperature, electrochemical noise, etc.

Figure 3.21. The digital photograph of impedance spectroscopy

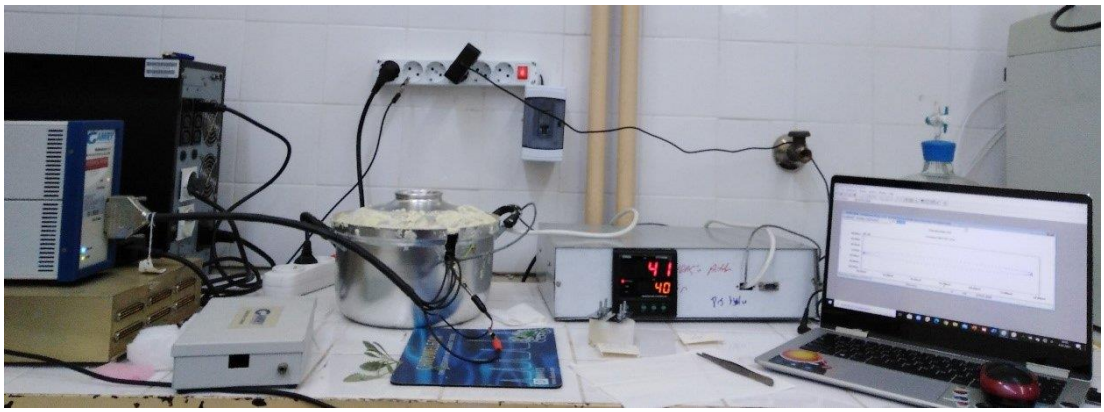

Figure 3.22. The installation EIS device connected to a controlled temperature measuring device and computer

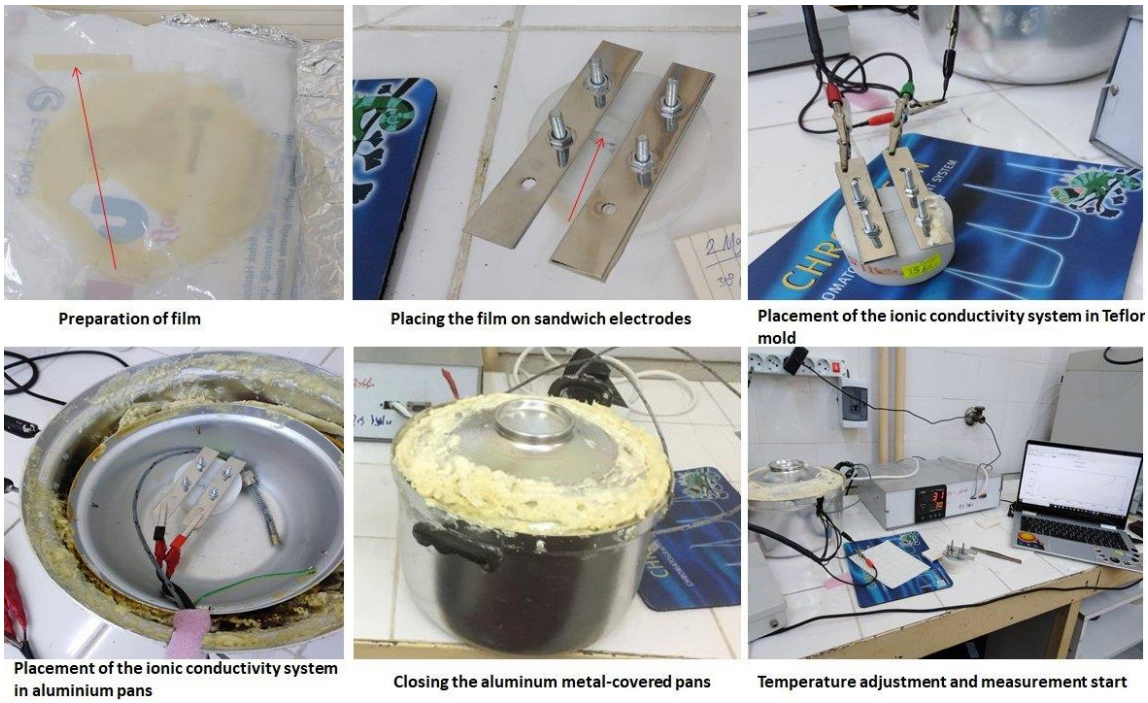

Figure 3.23. Experimental set up the ionic conductivity measurement

Impedance is a measured value in ohms, represented by the symbol *Z*. The current change is determined by measuring the impedance and the characteristic of the material is determined by increasing or decreasing the resistance. In short, impedance is defined as the factor that counteracts the electric current.

The expression Z (ω) consists of a real part [(Z' (ohm)] and an imaginary part [(Z" (ohm)]. If the real section is drawn on the x-axis and the imaginary section is drawn on the y-axis of the graph, a "Nyquist Plot" is obtained as given in Figure 3.24. In this graph, the y-axis is minus and each point in the Nyquist plot must represent impedance at a frequency, ω. Low and high-frequency data are on the right and left sides of the graph, respectively. On the Nyquist plot, impedance can be referred to as the norm of a vector |Z|. The angle (ϕ) between vector and x-axis, generally named “phase angle”. The impedance spectra of stainless steel/CPE/stainless steel (SS/CPE/SS) cells formed in the EIS analyzer are used to examine the ionic conductivity of membranes. Considering membrane geometry, the intersection of the real axis with the high-frequency arc (ω) gives the real impedance (Z' (ohm)) and the calculation is made according to the real impedance data.

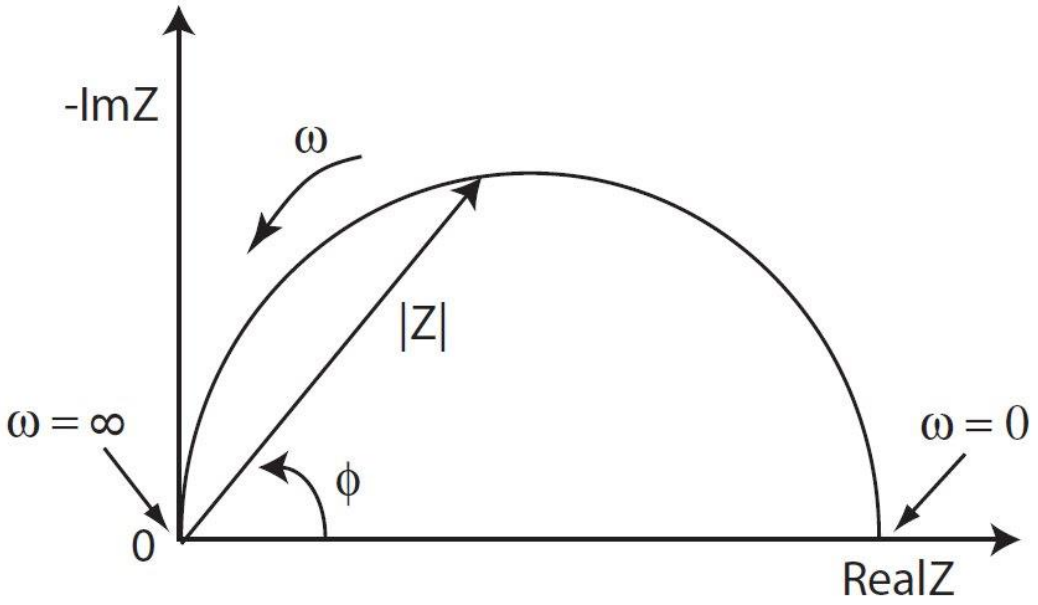

Figure 3.24. A simple Nyquist plot showing complex impedance vector Z(ω) (Addy, 2008)

The bulk resistance of nanocomposite polymer electrolytes containing MgBDC MOFs was found from the impedance spectrum. The ionic conductivity value was computed based on the equation below (Jinisha et al., 2017),

$$\sigma = \frac{t}{Rb \times A} \tag{3.7}$$

where σ (S/cm) is ionic conductivity, t (cm) is the thickness of the membrane, R_b (ohm or Ω) is the bulk resistance taken from x-axis intercession of complicated AC impedance line and A (cm^2) is an area of the membrane.

Also, the calculation of ionic conductivity, σ (S/cm) can be determined using the following equation:

$$\sigma = \frac{d}{Rb \times w \times t} \tag{3.8}$$

where *d* (cm) is the distance of two electrodes and *w* (cm) is the width of the film. Since *A* (*w* × *t*) is equal to the multiplying of *t* and film width (*w*), it can be substituted in the above (3.7) equation. Also, *d* between the two electrodes is fixed and taken as 1 cm.

The conductivity (σ)–temperature (T) plots show an *Arrhenius* type behavior throughout the temperature range. The linear change in log σ against 1000/T drawing can be expressed as a thermally activated status performed with the aid of this equation (Jinisha et al., 2017),

$$\sigma = \sigma_0 \exp\left(\frac{-Ea}{kT}\right) \quad \textbf{(3.9)}$$

where σ_0, E_a, and k are referred to as pre-exponential coefficient, activation energy (J/mol), and Boltzmann constant, respectively. The thermal activation energy is calculated according to the data from the Arrhenius plots.

4. RESULTS AND DISCUSSION

4.1. ATR FT-IR Results of Nanosized MgBDC MOF

ATR FT-IR spectrum results were determined organic bonds of nanosized MgBDC MOF structures in the region of 4000-400 cm^{-1}. As seen in Figure 4.1, the chemical structure interaction of Mg^{2+} ions and BDC is given. According to the IR results given in Figure 4.2, the broad peak that is located at ~3400 cm^{-1} refers to hydroxyl (OH^-) functional groups of water molecules. The exist of hydroxyl absorption peak means that some carboxylate group is not completely deprotonated and it refers to some free carboxylate as some of them are uncoordinated to the metal atom (Mathew et al., 2019). Two strong absorption peaks that appear at 1567 and 1397 cm^{-1} wavenumbers are related to symmetric-asymmetric stretching (υ_{as}) modes of carboxyl (COO) functional groups in MgBDC MOF, respectively (Chakraborty and Acharya, 2018; Mathew et al., 2019). The peaks at 1155, 1103, and 1023 cm^{-1} wavenumbers have corresponded to δ(CH) vibration modes from the BDC linker. A few peaks with smaller intensities can appear in the region of 1300-1020 cm^{-1}. The vibrations peaks that are detected at lower wavenumbers such as 825 cm^{-1} (Vu et al., 2015; Dhaouadi et al., 2011; Ansari et al., 2018), 438 cm^{-1} (Vu et al., 2015; Dhaouadi et al., 2011), and 517 cm^{-1} (Vu et al., 2015) correspond to stretching (υ) vibrations of –Mg–O–Mg–O– groups. A sharp peak that is determined at 755 cm^{-1} is relating the stretching (υ) and bending (δ) modes of Mg–O groups (Dhaouadi et al., 2011). According to FT-IR results, it was observed that vibration peaks caused by the bonding of Mg^{2+} ions and BDC components were absorbed and consistent results were obtained as desired.

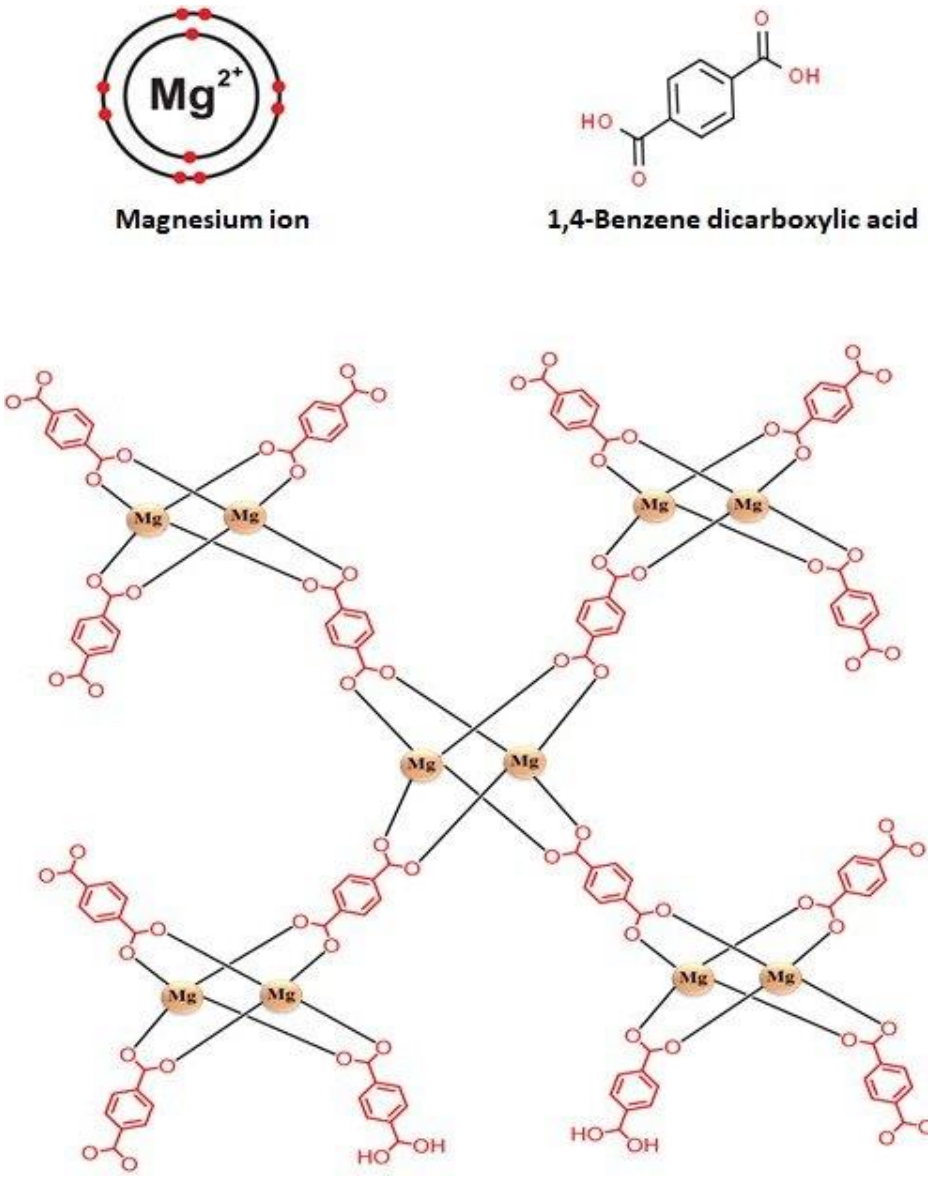

Figure 4.1. The chemical structure interaction of Mg^{2+} ion and BDC

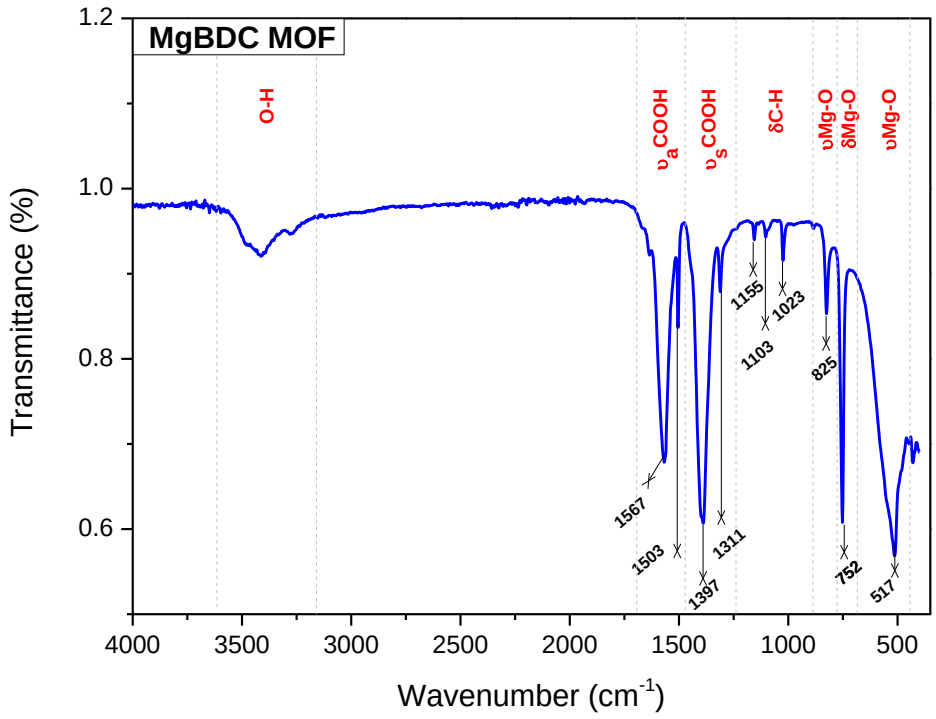

Figure 4.2. FT-IR spectra of nanosized MgBDC MOF in the region of 4000-400 cm^{-1}

4.2. TGA Analysis Results of Nanosized MgBDC MOF

TGA analysis results of nanosized MgBDC MOF are as shown in Figure 4.3 for the endothermic, exothermic reactions, and weight losses that occur with the temperature increase in the material. When examining the TGA curves, thermal events can be explained by two important conditions such as the removal of volatile components from the structure and the occurrence of oxidation of the material. An endothermic reaction occurred in which water and OH groups were removed from the structure between 60-200 °C. It was observed first endothermic peak at 190 °C as seen in Figure 4.3. The first thermal decomposition and the first weight loss of 13% occurred from 60 to 200 °C. These groups are attributed in consequence of the chemical events of solvents and precursors used in the structure. It is seen that MgBDC based MOF nanomaterials started to burn out at temperatures between 150 and 250°C. The molecules in DMF material used as solvent were completely removed from the structure when the temperature reached 235°C. A lot of exothermic reactions took

place between 200 and 550 °C and then thermogram curves continued in a stable line up to 550 °C. After 550 °C temperature, there were no volatile substances in the structure. Then second thermal decomposition broke down due to the second endothermic peak occurred at 645 °C. As a result, the MOF structure broke down and the second weight loss of 37.5 % occurred between 590 and 660 °C with temperature increase. The benzene dicarboxylate organic ligand, which was established as a strong coordination bridge with magnesium ions, was removed structure in the temperatures range of 590-660 °C. The thermogram curves also progressed in a stable line in temperature between 660 and 905 °C. The last one, that is, the third endothermic peak occurred at 930 °C and the third thermal decomposition and the third weight loss of 18.7% took place in the temperature range of 905 and 932 °C (Davies et al., 2007; Biswas et al., 2016). The weight loss occurred mostly between 590 and 660 °C temperatures. Thus, it was confirmed by TGA analysis that nanosized MgBDC MOF materials had high stability.

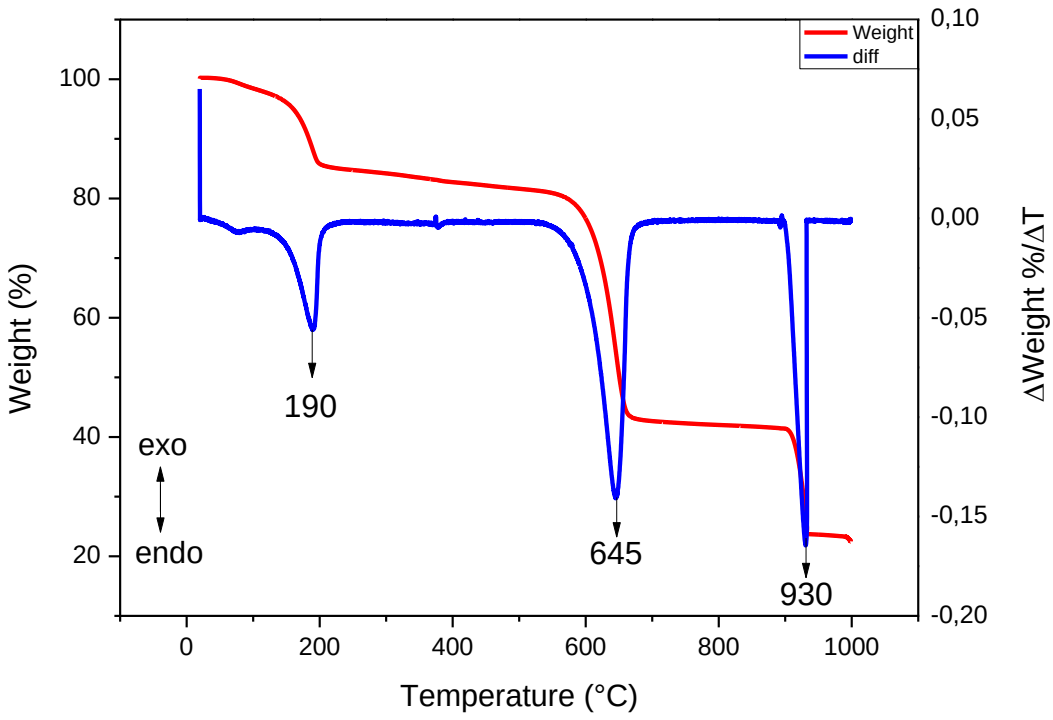

Figure 4.3. TGA results of nanosized MgBDC MOF

4.3. XRD Analysis Results of Nanosized MgBDC MOF

The experimental XRD data of nanosized MgBDC MOF samples are demonstrated in Figure 4.4. The sharp peaks that are determined at 2θ values of 9.6°, 14.5°, 29.7°, 34.2°, 38.8°, and 42.05° correspond to crystalline planes such as (220), (420) (Yuan et al., 2013), (201) (Rather, 2014), (202) (Rather, 2014; Saoud et al., 2014), (101) (Saoud et al., 2014) and (200) (Dhawa et al., 2017), respectively. X-ray diffraction pattern of nanosized MgBDC MOF is in good agreement with previously simulated XRD peaks (Kaduk, 2002; Davies et al., 2007; Biswas et al., 2016). Considering the crystallographic data, the high crystalline nature and purity of nanosized MgBDC MOF were confirmed. In Figure 4.4, the relative intensity of the second peak that is located at 2θ value of 14.5° (420) is the highest among all the peaks. The peak splitting at 2θ values of 9.5° and 14.5° was not observed, thereby protecting the crystal structure of nanosized MgBDC MOF (Davies et al., 2007; Biswas et al., 2016). The other characteristic peaks of MgBDC MOF were observed at 2θ values of 44.6°, 46.1°, 49.9°, and 58.7°. According to the quantitative analysis results of XRD data, it was determined that nanosized MgBDC MOF and brucite phase ($Mg(OH)_2$) contains the ratio of 96% and 4%, respectively. The brucite phase, that is, $Mg(OH)_2$ has the hexagonal structure crystal system and the characteristic reflection of its has appeared at 2θ values of 38,8° (101) (Rather, 2014; Saoud et al., 2014). XRD results of nanosized MgBDC MOF are compatible with the literature.

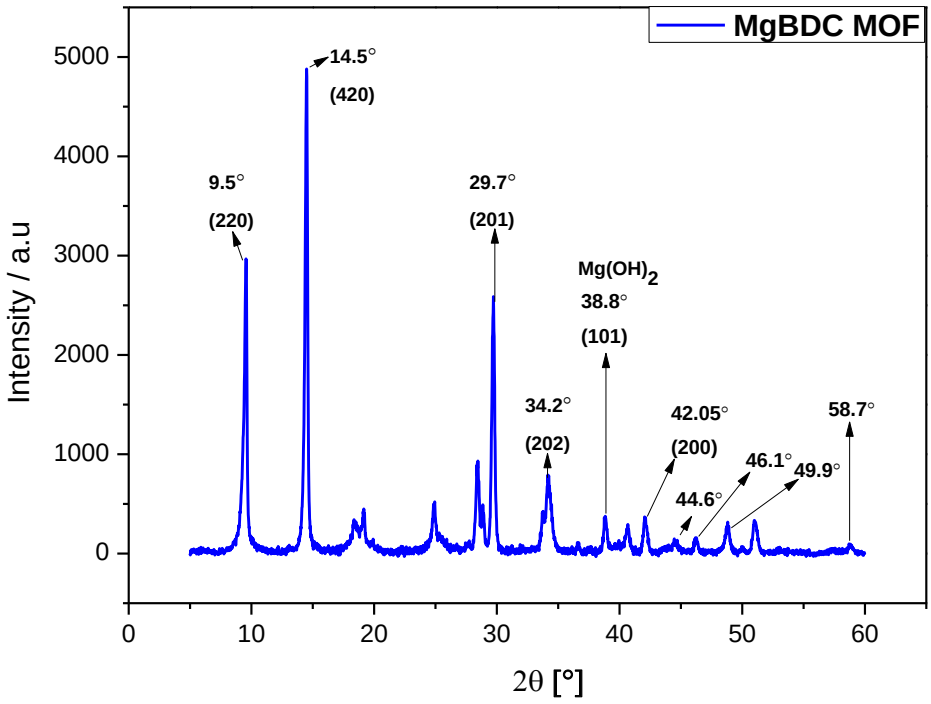

Figure 4.4. The experimental XRD pattern of nanosized MgBDC MOF

4.4. SEM/STEM/EDS Analysis Results in Nanosized MgBDC

SEM/STEM/EDS results of nanosized MgBDC MOF that were synthesized by using electrochemical synthesis methods are shown in Figures 4.5 (a-c). The morphology structure of MgBDC MOF nanoparticles in powder form is spherical, smooth structure, and pore-free. The grain sizes of these structures change in the range of 10-25 nm in Figure 4.5 (a). The morphology structure of MgBDC MOF nanoparticles that is obtained from a drop of dilute methanol solution, is plate-like and the grain sizes of them vary in the range of about 20 nm in Figure 4.5 (b) (Dhawa et al., 2017). In previous publications, the preparation of magnesium-based MOF structures by using the electrochemical method was not done and these structures were not observed on nanosized scales. So, quite good results were obtained from SEM analysis. STEM image of MgBDC MOF nanostructures was shown in Figure 4.5 (c). The homogeneous, regular, and uniform structures of powdered MgBDC nanoparticles were determined by STEM technique.

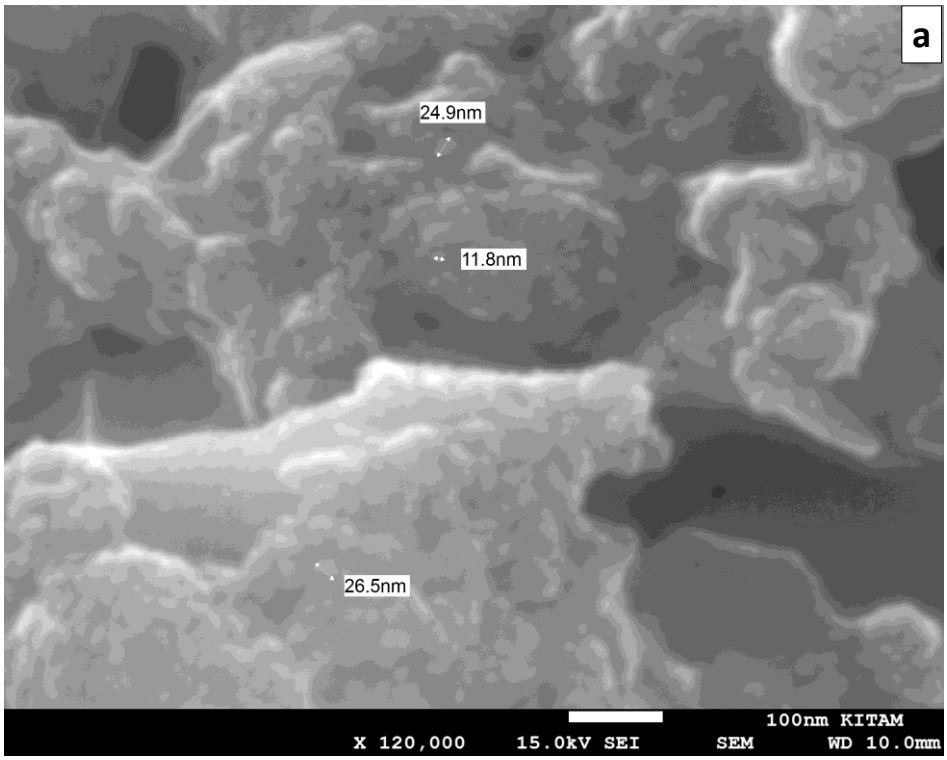
a
24.9nm
11.8nm
26.5nm
100nm KITAM
X 120,000 15.0kV SEI SEM WD 10.0mm

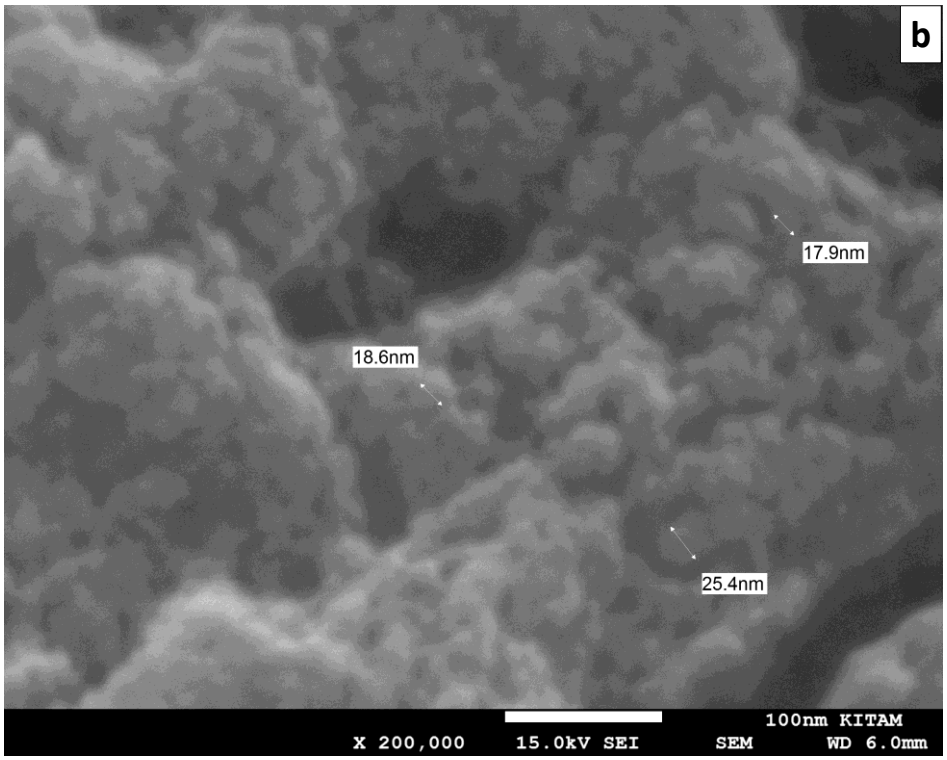
b
17.9nm
18.6nm
25.4nm
100nm KITAM
X 200,000 15.0kV SEI SEM WD 6.0mm

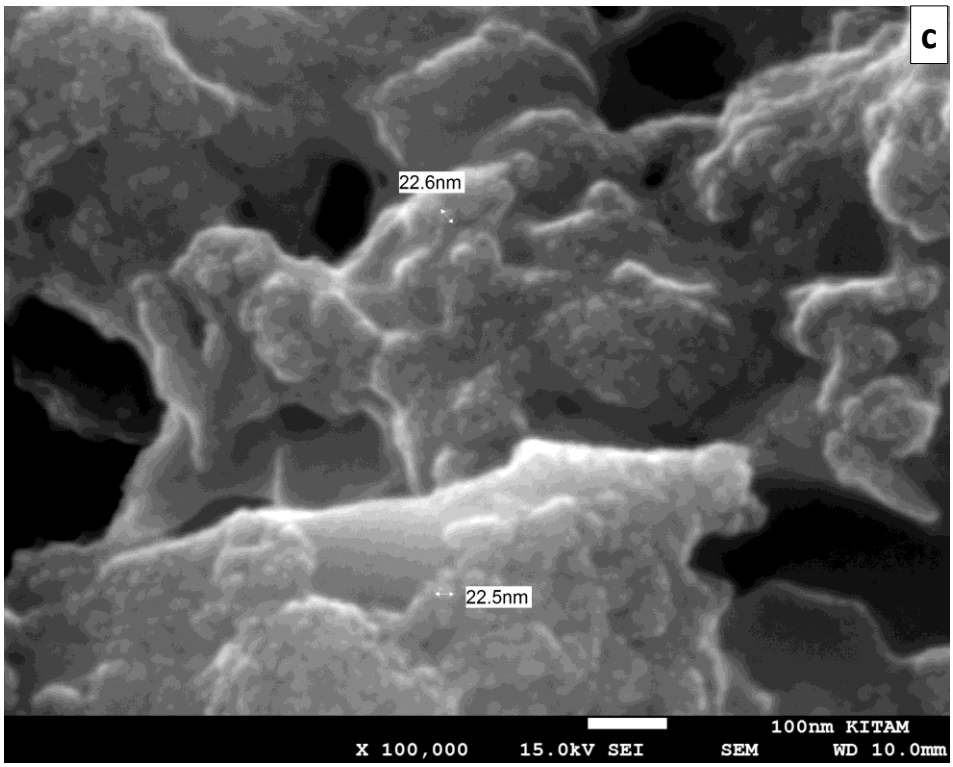

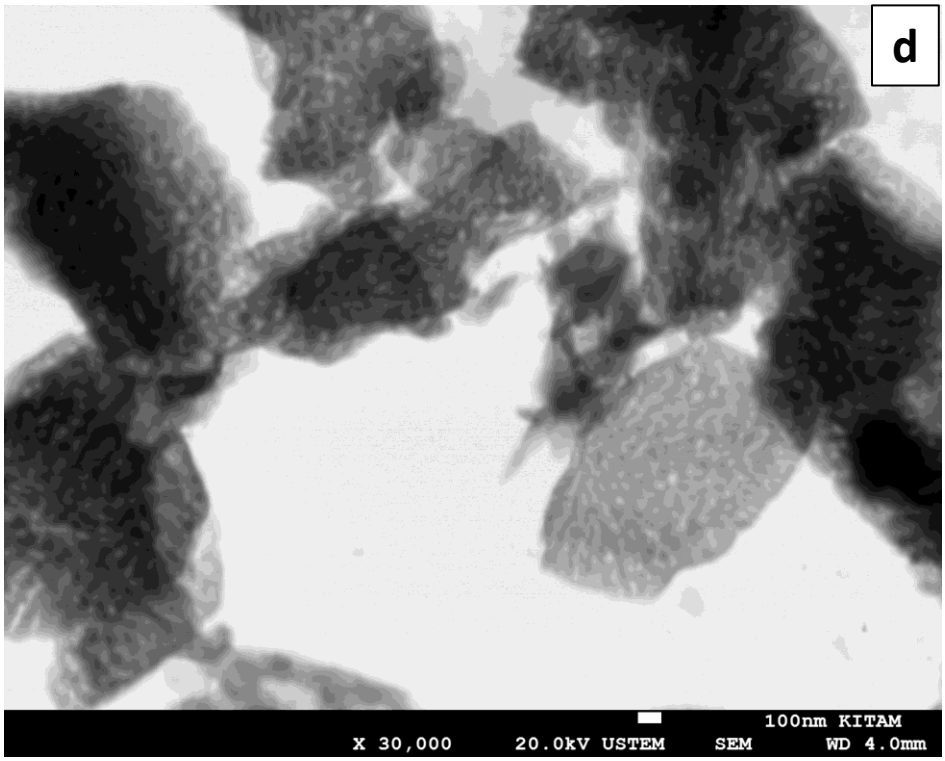

Figure 4.5. (a) and (b) SEM images of nanosized MgBDC particles in powder form, (c) SEM image of them in dilute form, and (d) STEM image of them

It was determined that SEM micro-images in Figure 4.5 (a-b) and EDS results of MgBDC MOF nanoparticles as shown in Figure 4.6 (a-c) were consistent with each other. The chemical compounds of nanosized MgBDC MOF were studied by EDS regional-mapping-spectra analyses as given in Figure 4.6 (a-c). Based on EDS regional and EDS mapping analysis results, it was verified that nanosized MgBDC MOF structures are homogeneous distribution as demonstrated in Figure 4.6 (a-b). The presence of high purity Mg, C, and O atoms was confirmed by EDS mapping-spectra analyses of MgBDC MOF as indicated in Figure 4.6 (b-c) (Dhawa et al., 2017).

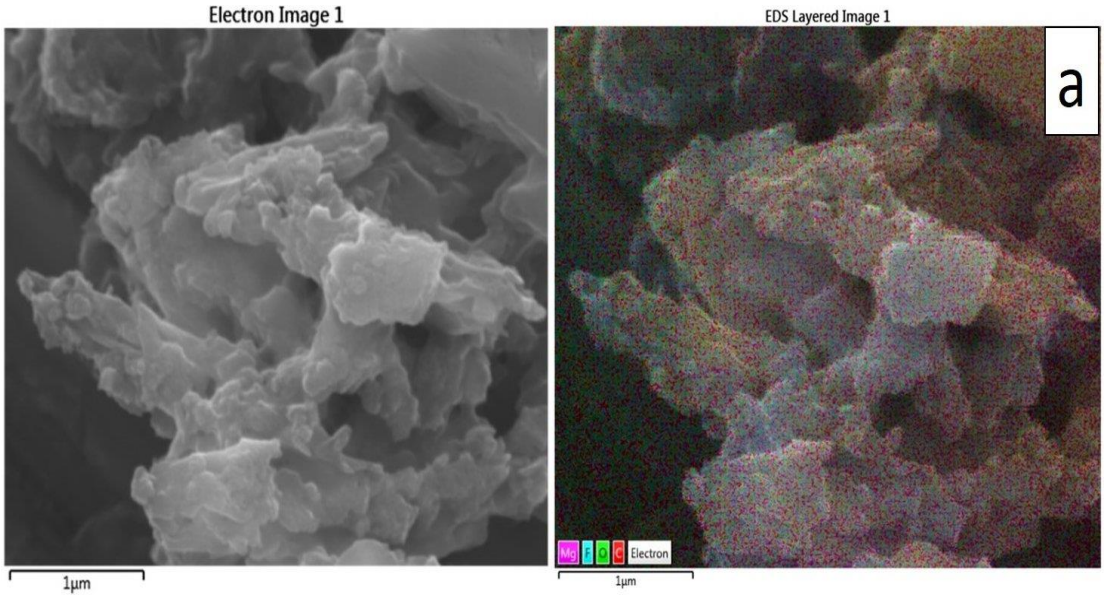

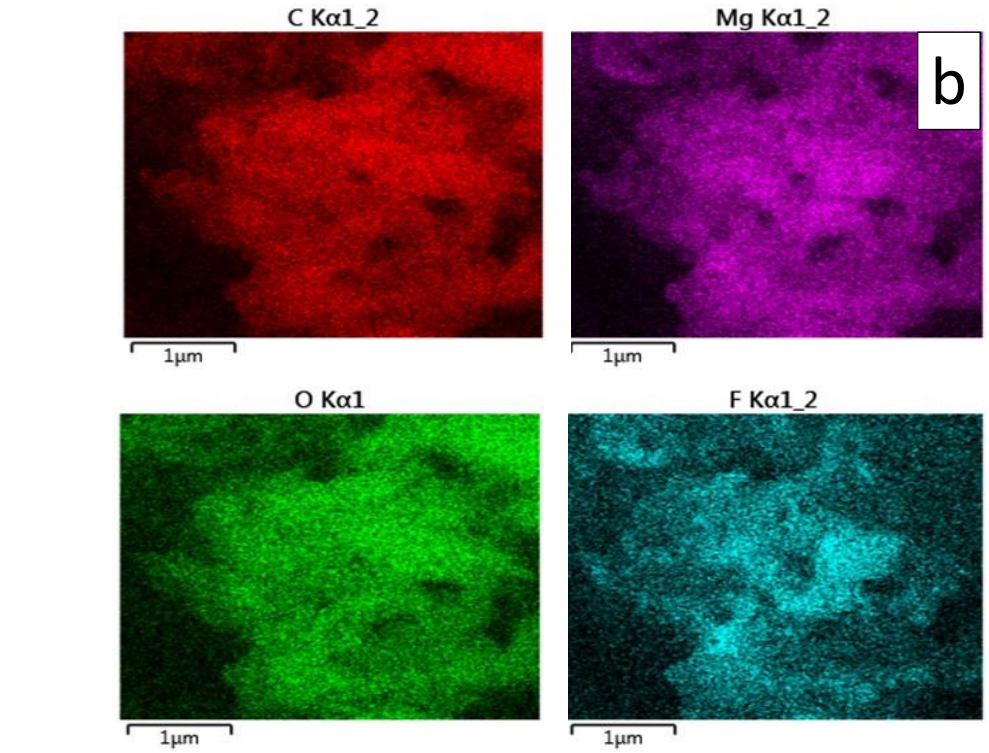

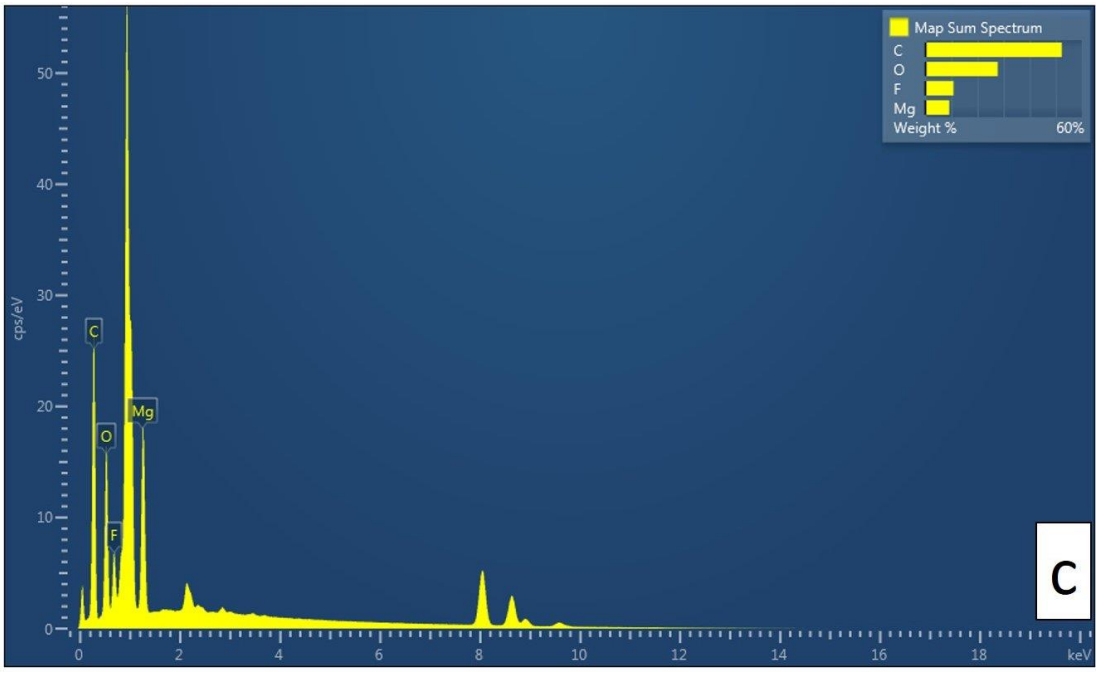

Figure 4.6. (a) EDS regional, (b) EDS mapping, and (c) EDS spectra analysis results of nanosized MgBDC MOF particles

4.5. AFM Analysis Results of Nanosized MgBDC MOF

The surface roughness of nanosized MgBDC MOF structures was studied by AFM analysis and AFM images of nanosized MgBDC MOFs are given in Figure 4.7. MgBDC MOF nanoparticles were very well dispersed on the substrate. Based on AFM tapping mode images, it was observed that MgBDC MOF nanoparticles had homogeneous structure, regular distribution, and spherical shape. It has also been found that their dimensions range from 30 to 50 nm. The uniform distribution of them on the surface can be related to good nucleation sites for their controlled growth. The AFM results were consistent with the SEM results and the morphological properties and grain structures supported each other.

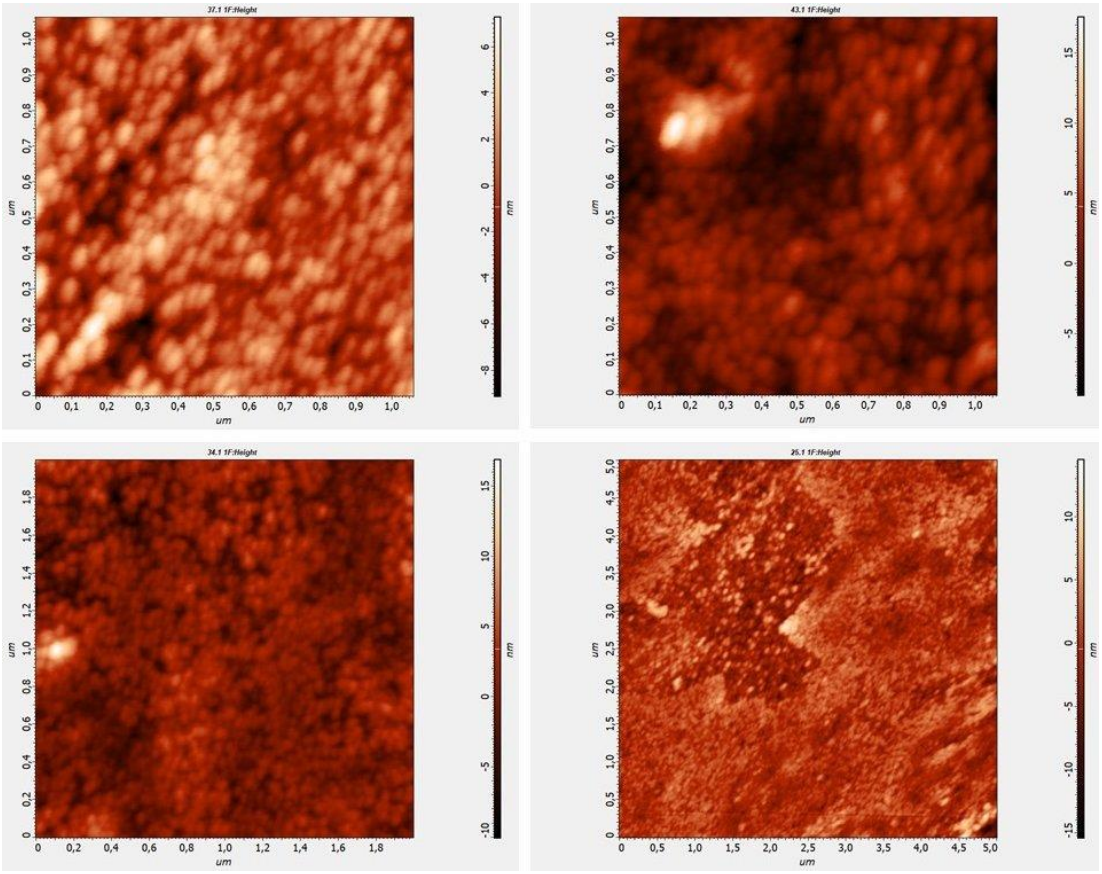

Figure 4.7. AFM images of nanosized Mg-BDC MOF

4.6. BET Analysis Results of Nanosized MgBDC MOF

BET analysis results are shown in Table 4.1. The total surface area (S_{BET}), pore volume (V_{pore}), and average pore size radius of nanosized MgBDC MOF were found to be 23.132 m^2/g, 0.057 cm^3/g, and ~50 nm, respectively. In a previous study, MgBDC MOF in N, N'-diethylformamide (DEF) solvent was synthesized by using the solvothermal method. After drying at 120 °C for 18 hours, a fair amount of MOF was carried out at a temperature of 30 °C for 30 minutes under nitrogen atmospheric pressure and the other portion of the MOF was applied at 400 degrees under the same time and conditions. BET surface areas of these were found to be 193 and 378 m^2/g, respectively (Yuan et al., 2013). According to these analyzer results, the surface area of carbon-doped poly(vinylpyrrolidone) MgBDC MOF is determined as 310 m^2/g in another previous study (Dhawa et al., 2017). This situation can be explained by that structural features of MOF nanoparticles are affected by starting materials, variety of solvents, concentrations, synthesis techniques, and temperatures (Biswas et al., 2016; Tranchemontagne et al., 2008). Also, DEF is an expensive solvent and it is well known that higher surface areas can be reached surface area generally achieved with cheap DMF (Burgaz et al., 2019; Chen et al., 2010).

Table 4.1. BET analysis results of nanosized MgBDC MOF

Tot. surface area (S_{BET})	The pore volume (V_{pore})	Average pore size radius (nm)
23.132 m^2/g	0.057 cm^3/g	~50

4.7. ATR FT-IR Spectroscopy Results of PEO Based NCPEs Containing MgBDC MOF

ATR FT-IR spectrum results were examined to determine the organic structures of pure PEO, pure LiTFSI, PEO–LiTFSI system (PEO based SPE), and PEO based NCPEs containing nanosized MgBDC MOF in the region of 4000–400 cm^{-1}. The FT-IR results of these structures are given and discussed in detail in Figures 4.8-18 and

Tables 4.2-4. The schematic representation of attachment of Li^+ ion with ether oxygen of polymer chain PEO is given in Figure 4.10.

When Figure 4.8 was examined, many band structures were obtained with different wavenumbers. The characteristic vibrational spectral bands in pure PEO are found about 1150, 1100, 1050, 528, and 508 cm^{-1} wavenumbers. These peaks are referred to as the symmetric and asymmetric stretching vibrations of carboxylic acid functional groups (Reedy et al., 2006; Burgaz, 2011; Isakov et al., 2009; Yoshihara et al., 1964). The v_{as}(C–O–C) vibration modes are separated into three strong peaks at 1146, 1096, and 1060 cm^{-1} in as shown in Figure 4.8. The peaks at 1360 and 1341 cm^{-1} are the peaks of $\delta(CH_2)$ vibration (Reedy et al., 2006; Polu and Rhee, 2015; Tang et al., 2007). In Figure 4.8, the bands observed in the 2881 and 1466 cm^{-1} are a result of v(C–H) vibration (Polu and Rhee, 2015; Tang et al., 2007; Ramesh et al., 2008; Rajendran et al., 2000; Rajendran et al., 2001; Mathew et al., 2019) and CH_2 scissoring vibrations, respectively (Ramesh et al., 2008; Mathew et al., 2019). The other vibrational spectral peaks at 1279 and 1240 cm^{-1} have corresponded to asymmetric and symmetric CH_2 twisting vibrations (Isakov et al., 2009; Yoshihara et al., 1964; Nagajothi et al., 2018; K.N. Kumar et al., 2014; K.K. Kumar, et al., 2014). The peaks at 960 and 946 cm^{-1} are corresponded to CH_2 twisting vibration mode and the band at 841 cm^{-1} is referred to as CH_2 wagging mode (Polu and Rhee, 2015; Ramesh et al., 2008; Rajendran et al., 2001; Mathew et al., 2019). All results in pure PEO electrolyte spectrum are consistent with the literature and it was confirmed the existence of PEO crystallinity as shown in Figure 4.8.

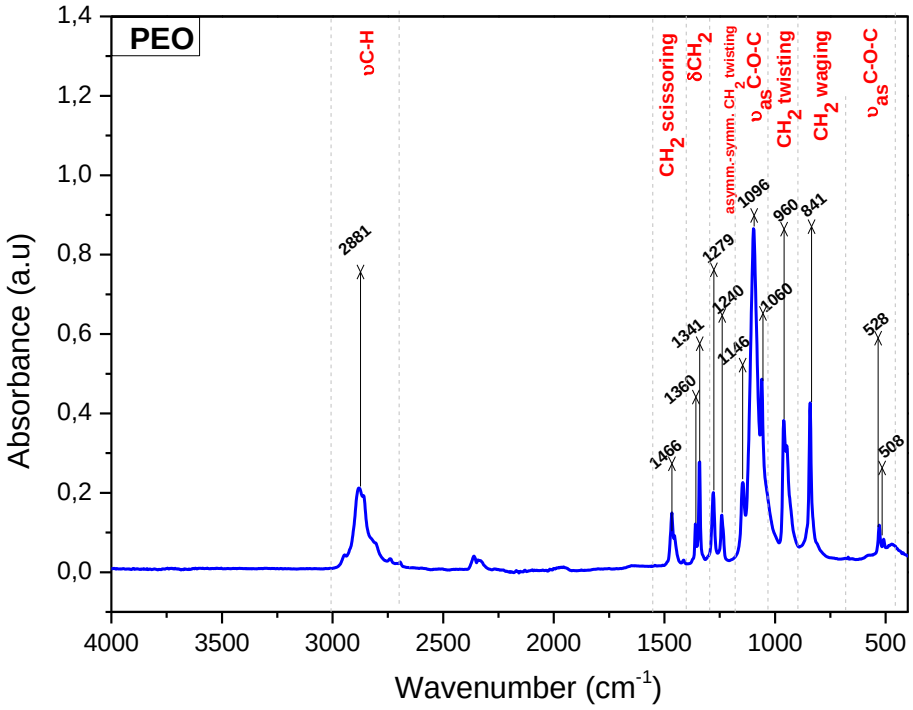

Figure 4.8. ATR FT-IR results of pristine PEO in the region of 4000-400 cm^{-1}

Absorption peaks for pure LiTFSI at 1345, 1326, and 1315 cm^{-1} are referred to $\upsilon_a(SO_2)$ vibration (Li et al., 2000; Deepa et al., 2004; Zhou and Fedkiw, 2004). Spectral peaks at 1243 and 1196 cm^{-1} are peaks of $\upsilon_{as}(CF_3)$ vibration (Li et al., 2000; Deepa et al., 2004; Zhou and Fedkiw, 2004; Deepa et al., 2002; Wu et al., 2017; Nagajothi et al., 2017). The peaks at 1140 and 1061 to 799 cm^{-1} are attributed to $\upsilon_s(SO_2)$ and υ_s(S–N–S) vibration modes, respectively (Polu and Rhee, 2015; Li et al., 2000; Deepa et al., 2004; Zhou and Fedkiw, 2004; Wu et al., 2017; Nagajothi et al., 2017; Vélez et al., 2016). The spectral bands at 772 and 746 cm^{-1} are referred to υ(C–S) (Polu and Rhee, 2015; Li et al., 2000; Zhou and Fedkiw, 2004) and $\delta_s(CF_3)$ vibration modes, respectively (Polu and Rhee, 2015; Li et al., 2000). The δ(S–N–S) vibration mode peaks at 645 cm^{-1} (Polu and Rhee, 2015; Li et al., 2000). The absorption peaks at 607 and 601 cm^{-1} in-plane and out-of-plane of $\delta_a(SO_2)$ deformation modes, respectively (Polu and Rhee, 2015; Li et al., 2000). The peaks at 572, 552, and 512 cm^{-1} are referred to $\delta_a(CF_3)$ vibration modes (Polu and Rhee, 2015; Li et al., 2000; Deepa et al., 2004). It is confirmed in this study that the peaks from previous studies for pure LiTFSI have

approximately the same wavenumbers as shown in Figure 4.9. The small peaks were found in the region of 3640-3399 cm^{-1} wavenumbers range corresponding to the hydroxyl functional (OH^-) groups of water molecules due to the moisture from the structure.

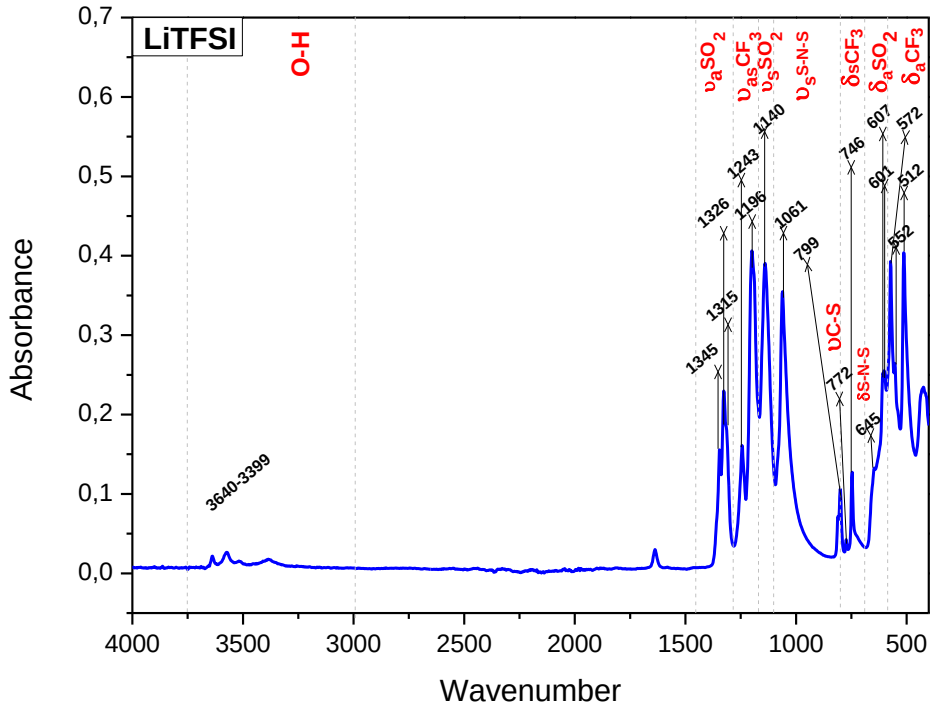

Figure 4.9. ATR FT-IR results of pure LiTFSI in the region of 4000-400 cm^{-1}

Polymer-salt complexation occurs when a certain amount of LiTFSI salt (15 wt.% and 20 wt.%) is added to the polymer electrolyte film (Reedy et al., 2006; Polu and Rhee, 2015; Gupta et al., 2016; Wen et al., 1996; Xu, 2004; Borodin and Smith, 2006; Singh et al., 2017). The complexation of LiTFSI salt occurred with the attachment of Li^+ cation ion with five ether oxygen of polymer chain PEO chain as given in Figure 4.10 (Gupta et al., 2016; Xu, 2004). The motion of lithium cations (Li^+) takes place through the hopping and diffusion mechanism. As shown in Figure 4.10, lithium cation (Li^+) affects five ether oxygen of PEO and goes towards polymer matrix by hopping movement (Gupta et al., 2016; Borodin and Smith, 2006).

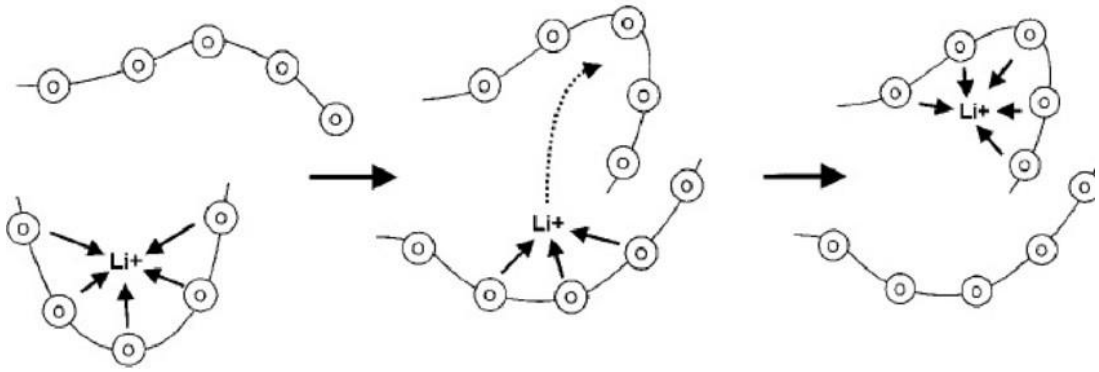

Figure 4.10. Schematic representation of attachment of Li^+ ion with ether oxygen of polymer chain PEO (Meyer, 1998)

When LiTFSI was incorporated with the PEO matrix, IR bands of υ(C–H), υ_{as}(C–O–C), and $TFSI^-$ compounds were affected in terms of intensity, shape, and position. The original peaks of pure PEO have shifted from 2881 to 2877 cm^{-1}. The intensity of υ(C–H) vibration mode decreased and broadened as indicated in Figure 4.11 (Reedy et al., 2006; Polu and Rhee, 2015; Tang et al., 2007; Mathew et al., 2019). The center of the band of PEO changed because of the sulfur-methylene ($S\text{-}CH_3$) bond from $TFSI^-$ anion (Polu and Rhee, 2015).

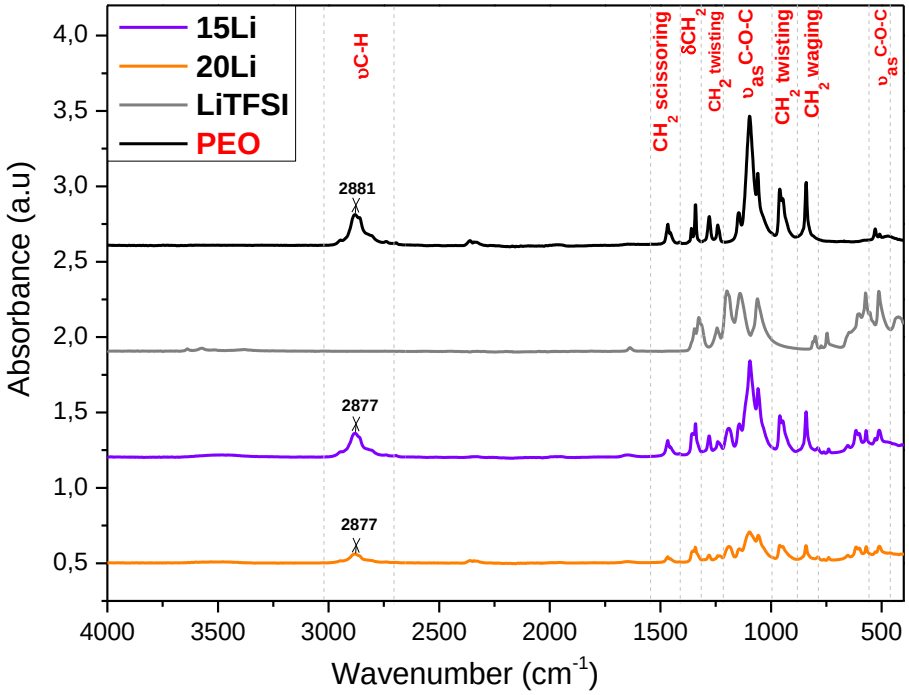

Figure 4.11. ATR FT-IR results of PEO-LiTFSI electrolytes in the region of 4000-400 cm^{-1} (PEO affected by LiTFSI)

After adding LiTFSI salt to the PEO substance, CH_2 scissoring vibration changed from 1466 to 1465 cm^{-1}. The peaks of $\delta(CH_2)$ vibration replaced from 1360, 1341 to 1354, 1340 cm^{-1}. The vibrational spectra of v_{as}(C–O–C) vibration mode from 1146,1096, 1060 to 1142, 1194, 1056 cm^{-1}. The peaks of CH_2 twisting at 960 and 946 cm^{-1} did not change. The peak of CH_2 wagging mode shifted from 841 to 842 cm^{-1}. While there was no change in the peak of v_{as}(C–O–C) vibration mode at 528 cm^{-1}, the band at 508 cm^{-1} shifted to 509 cm^{-1}, respectively as shown in Figure 4.12 (Polu and Rhee, 2015; Ramesh et al., 2008; Rajendran et al., 2001; Mathew et al., 2019; Gupta et al., 2016). The intensity of CH_2 scissoring, $\delta(CH_2)$, v_{as}(C–O–C), CH_2 twisting, and CH_2 wagging modes decreased and broadened (Polu and Rhee, 2015; Mathew et al., 2019). Also, it can be said that the shapes and positions of them changed in the IR spectrum. The FT-IR vibrational spectra of the PEO-LiTFSI sample have considerably spread and so, it can be indicated that the crystal structure of PEO decreases and turns into an amorphous structure with the help of a mixture of a lithium salt (Tang et al.,

2007; Mathew et al., 2019; Gupta et al., 2016; Wen et al., 1996). Many shifts occurred in bands of PEO due to the strong lithium cation complexation with PEO. These shifts can be explained by the that Li^+ acts in the polymer matrix by hopping mechanism as shown in Figure 4.10 (Gupta et al., 2016). The decrease of peaks in the FT-IR spectrum is an expected situation. This situation can be explained that these bands bonded with organic compounds from $TFSI^-$ anions. Also, there is related to the proportion of lithium salt added to PEO. Correspondingly, it can be said that as the content of salt increases, it absorbs more and bonds better. As a result, PEO-based electrolytes containing 20 wt % lithium salt may be more an amorphous and proper material in the PEO-LiTFSI system.

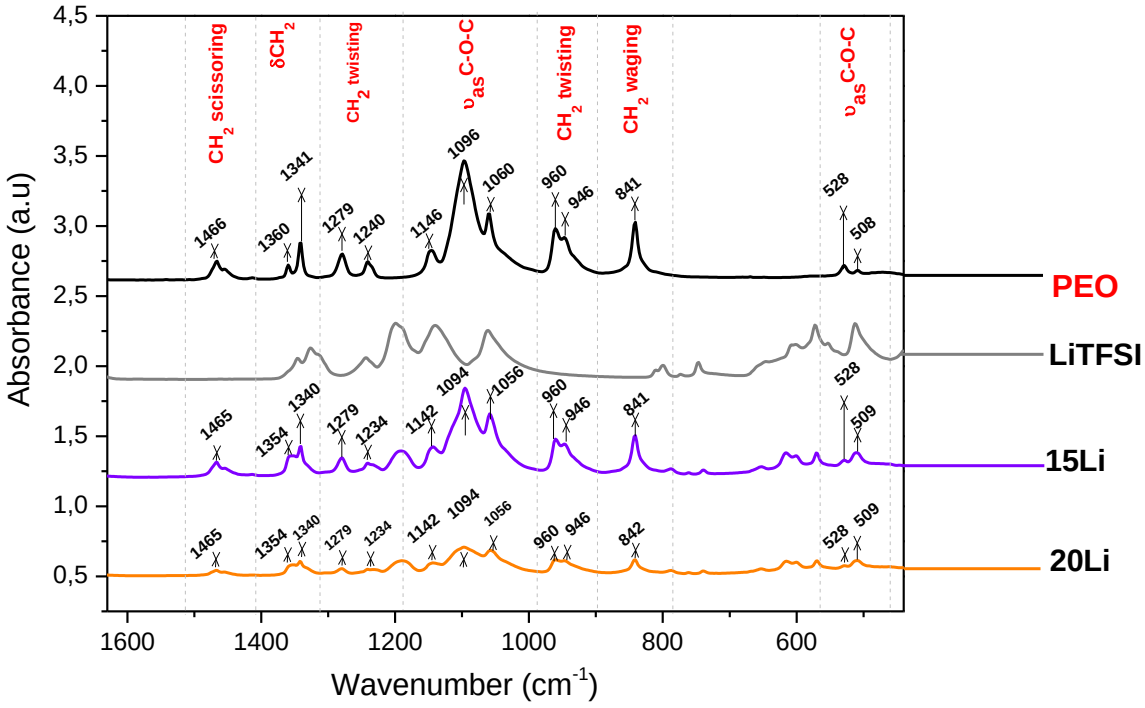

Figure 4.12. ATR FT-IR results of PEO-LiTFSI electrolytes in the region of 1630-400 cm^{-1} (PEO affected by LiTFSI)

After adding Li salt to PEO material, the absorption peaks of pure LiTFSI were broadened and changed. $v_a(SO_2)$ vibration mode shifted from 1345, 1326, to 1354-

1352, 1341 cm^{-1}. The bands at 1315 cm^{-1} disappeared as shown in Figure 4.13. $v_{as}(CF_3)$ vibration mode shifted from 1243, 1196 to 1240-1232, 1191 cm^{-1}. $v_s(SO_2)$ and v_s(S–N–S) vibration modes shifted from 1140 and 1061 to 1144-1143 and 1057 cm^{-1}, respectively, as shown in Figure 4.13. Similarly, absorption peaks of pure Li salt were expanded and shifted due to C–SO_2–N bonds, and their intensities were decreased. υ_s(S–N–S) vibration mode shifted from 799 to 788-787 cm^{-1}, v(C–S) mode from 772 to 761-760 cm^{-1} (Polu and Rhee, 2015), $\delta_s(CF_3)$ mode shifted from 746 to 739 cm^{-1} (Li et al., 2000; Bakker et al., 1996), δ(S–N–S) mode from 645 to 654-653 cm^{-1} and the $\delta_a(SO_2)$ in-plane and out-of-plane vibration mode from 607, 601 to 616-615, 601-600 cm^{-1}, respectively (Polu and Rhee, 2015). In polymer-lithium salt complex, $\delta_a(CF_3)$ vibration mode was shifted from 572, 512 to 570-569, 510 cm^{-1}. The band at 553 cm^{-1} disappeared as given in Figure 4.13 (Polu and Rhee, 2015). The disappearances, increases, or decreases of peaks in the FT-IR spectrum is an expected situation. This situation can be explained that these bands bonded with organic compounds from PEO.

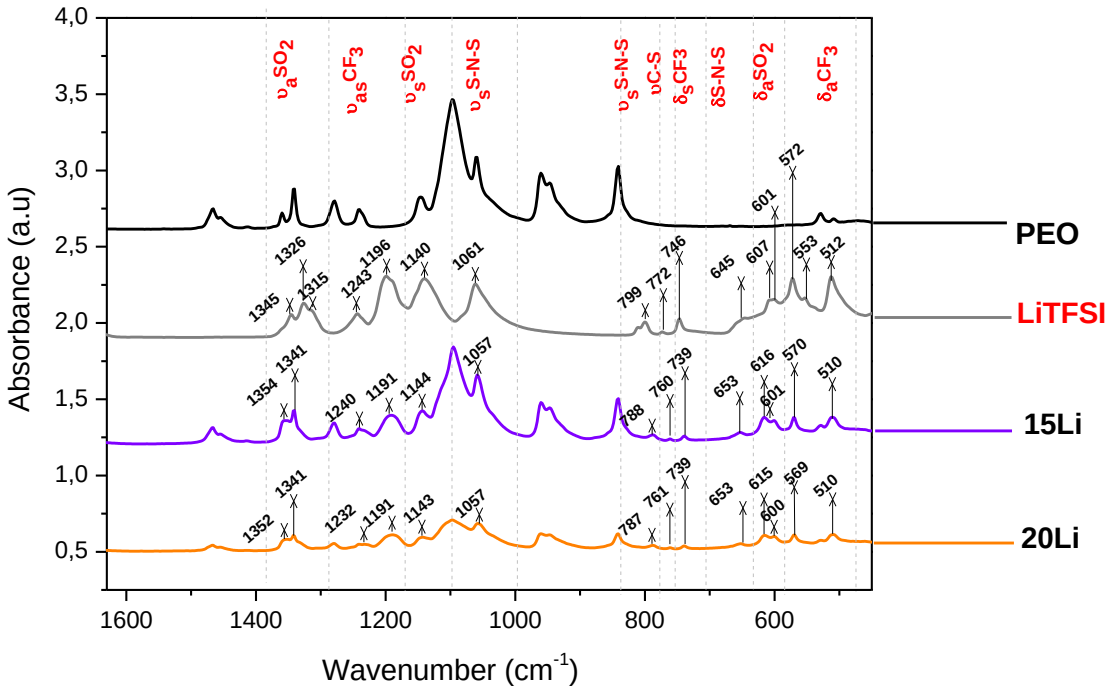

Figure 4.13. ATR FT-IR results of PEO-LiTFSI electrolytes in the region of 1630-400 cm^{-1} (LiTFSI affected by PEO)

When nanosized MgBDC MOF was incorporated with the PEO-LiTFSI matrix, the intensities, positions, and shapes of all $TFSI^-$, PEO, and MgBDC MOF peaks were changed. As mentioned earlier in the FT-IR analysis of MgBDC MOF powder, the sharp peaks of its were explained at 1567, 1503, 1397, 1311, 1155, 1103, 1023, 825, 752, and 517 cm^{-1} as shown in Figure 4.14. The asymmetric and symmetric stretching vibrations from the carboxylic acid functional groups (COOH) were observed in strongly characteristic absorptions at around between 1600-1500 cm^{-1} and 1470-1400 cm^{-1}, respectively, as shown in Figure 4.14 (Burgaz et al., 2019). The υ_a(COOH) and υ_s(COOH) vibration bands corresponding to 1565-1503 and 1400 cm^{-1}, respectively showed that BDC was coordinated with magnesium (Mathew et al., 2019; Burgaz et al., 2019; Chakraborty and Acharya, 2018). The bending (δ) vibration modes located in the region of 1200-700 cm^{-1} correspond to the fingerprint of BDC aromatic compositions as shown in Figure 4.14 (Mathew et al., 2019; Sabouni et al., 2010). The δ(C–H) in-plane and out-of-plane bending modes present in the benzene ring of the BDC linker are observed in the region the peaks range of 1230-950 and 900-700 cm^{-1}, respectively as shown in Figure 4.14 (Yadav et al., 2016; Petit, and Bandosz, 2010). The vibrations peaks at 825 and 517 cm^{-1} refer to stretching vibrations of –Mg–O– groups (Dhaouadi et al., 2011; Ansari et al., 2018; Davies et al., 2007). The sharp peak that is observed at 755 cm^{-1} is relevant to the stretching and the bending vibrations of Mg–O groups (Ansari et al., 2018).

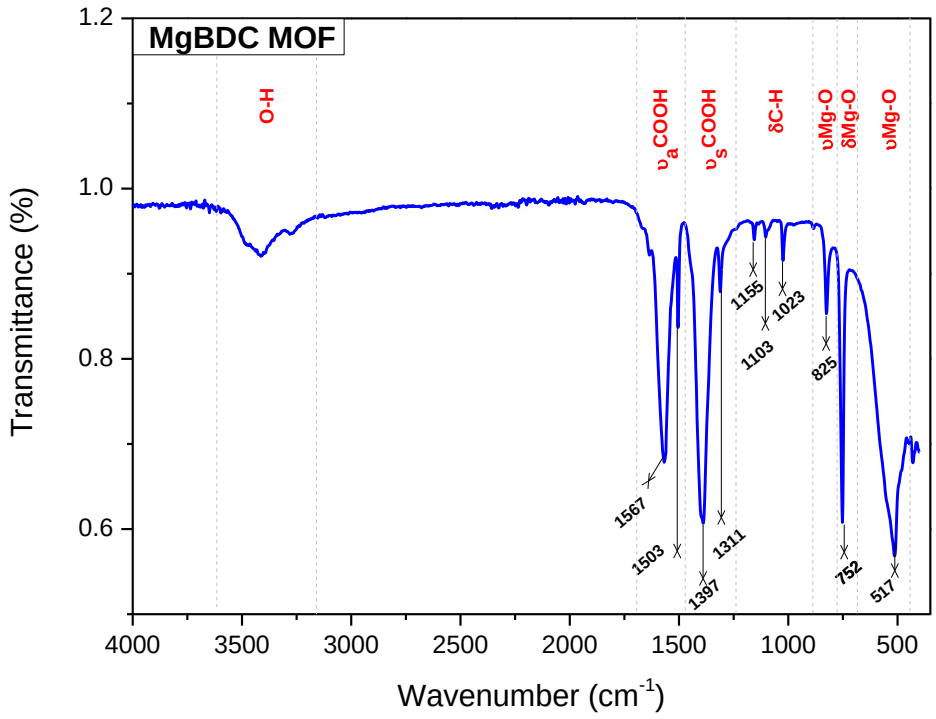

Figure 4.14. FT-IR results of nanosized MgBDC MOF powder in the region of 4000-400 cm^{-1}

After adding MgBDC MOF to the mixture of polymer-lithium salt, the characteristic peaks of pure PEO slightly changed. The observed v(C–H) vibration mode at 2877 cm^{-1} in the PEO-LiTFSI system shifted to 2879-2877 cm^{-1} in the PEO-LiTFSI-MgBDC MOF system as given in Figure 4.15. In the FT-IR spectrum, the observed band at 2879 cm^{-1} was broadened. Similarly, the obtained CH_2 scissoring vibration peak at 1465 cm^{-1} in the PEO-based SPE system shifted to 1467 cm^{-1} as shown in Figure 4.16. The peaks of $\delta(CH_2)$ vibration mode shifted from 1354, 1340 to 1355-1350, 1342-1331 cm^{-1} as shown in Figure 4.16. There was no change in the band of asymmetric CH_2 twisting at 1279 cm^{-1} and the symmetric CH_2 twisting mode shifted from 1234 to 1236-1228 cm^{-1} as shown in Figure 4.16. The v_{as}(C–O–C) vibration modes shifted from 1142, 1094, 1056 to 1143-1135, 1099-1093, 1056-1055 cm^{-1} and had a lower intensity peak them (Mathew et al., 2019). The CH_2 twisting vibration peaks shifted from 960 to 962-950 cm^{-1}. The band at 946 cm^{-1} disappeared in a PEO-based NCPE system containing 20 wt.% lithium salt and 5 wt. % MgBDC MOF. There was no change in the peak of CH_2 wagging vibration at 841 cm^{-1} as shown in Figure

4.16. There were no changes in the peaks of v_{as}(C–O–C) vibration mode at 528 and 509 cm^{-1} (Mathew et al., 2019). On the other hand, a broad peak was found around 3400 cm^{-1} correspondings to hydroxyl functional groups of water molecules because of the small amount of moisture remained PEO-LiTFSI-MgBDC structure (Mathew et al., 2019). As a result of the adding of MgBDC MOF into the PEO-LiTFSI matrix occurred the constitution of complexation in this system. The previously amorphized structures with the adding of lithium salt were slightly crystallized again due to the mixture of MgBDC MOF to PEO-LiTFSI matrix. This case is related to the proportion of MgBDC MOF added to the PEO-LiTFSI matrix. Correspondingly, it can be said that as the amount of MgBDC MOF increases, the structure becomes more crystalline property. As the use of MgBDC MOF is effective in crystallizing the material, the amount of MgBDC MOF is important. Therefore, the amount of MgBDC MOF used in NCPEs production was determined as an optimum ratio of 2 and 5 wt. %. According to FT-IR analysis results, it can be said that the ratio of 5 wt. % MgBDC MOF ratio used is more suitable for obtaining semi-crystalline material. As a result, it can be stated that the obtained structures turned to semi-crystalline polymer materials. The decreases and increases of peaks are the desired situation in IR bands of the PEO-LiTFSI-MgBDC system. This situation can be explained that these peaks bonded with organic compounds from MgBDC MOF.

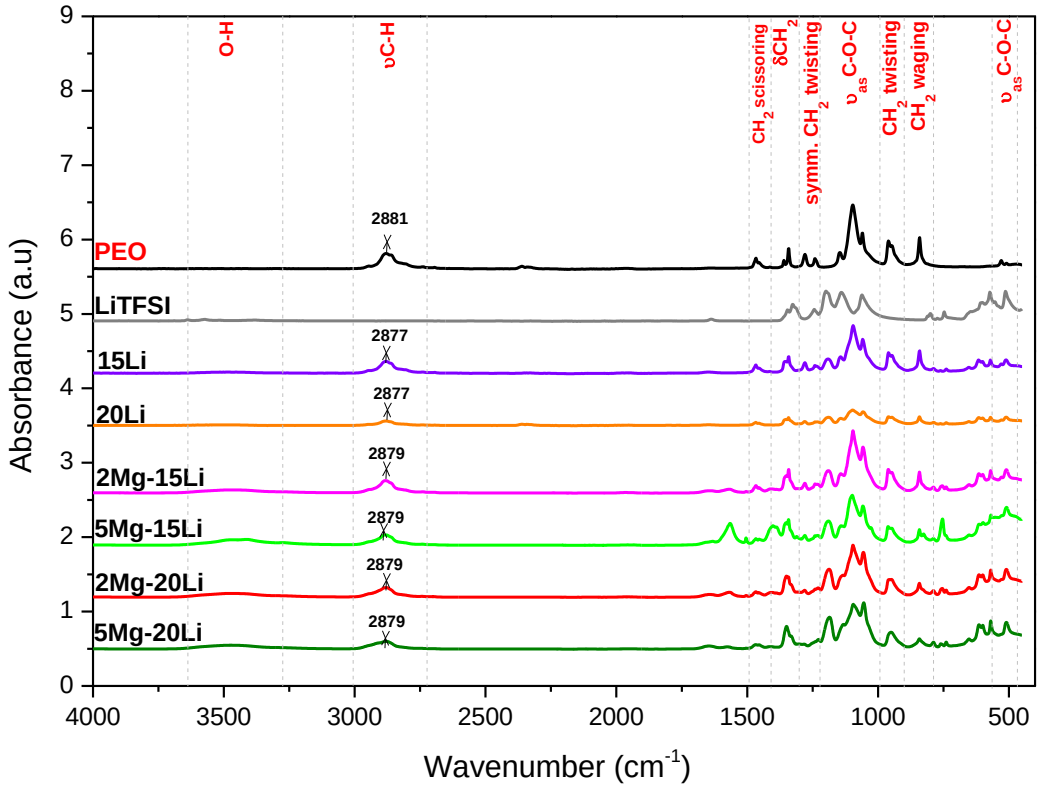

Figure 4.15. ATR FT-IR results of PEO based NCPEs containing MgBDC MOF in the region of 4000-400 cm^{-1} (PEO affected by MgBDC MOF)

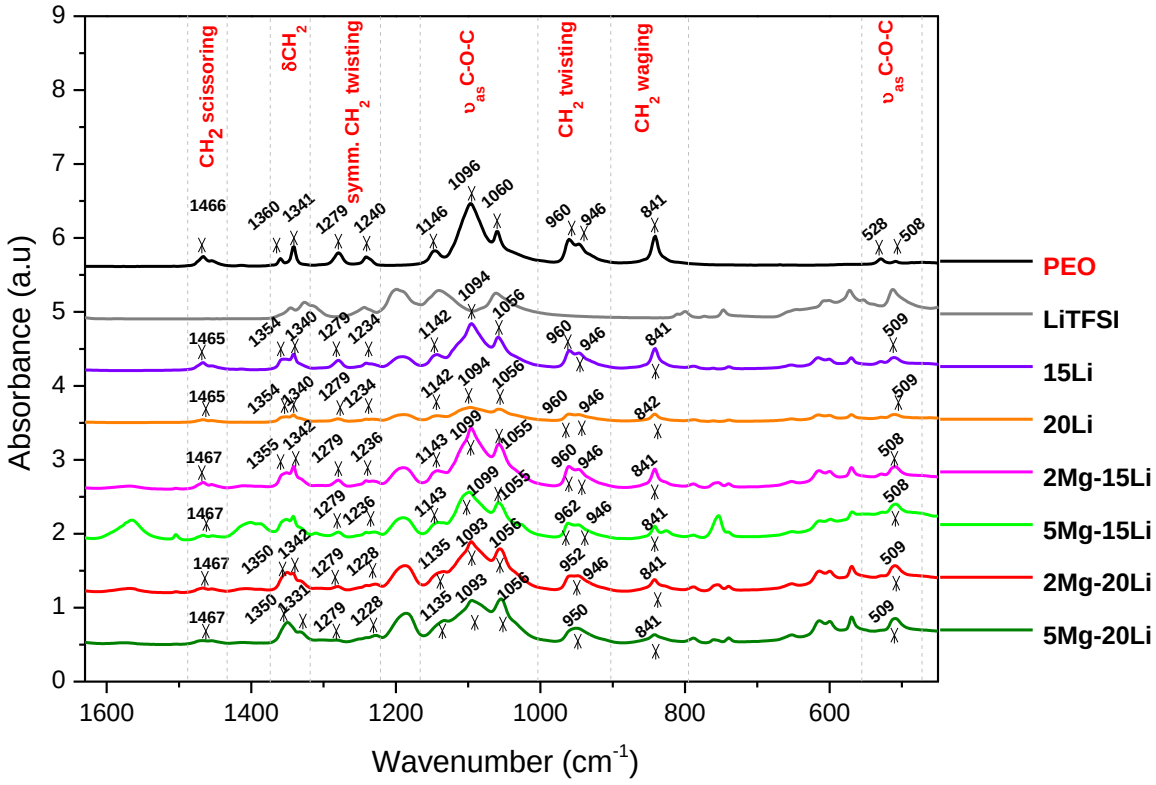

Figure 4.16. ATR FT-IR results of PEO based NCPEs containing MgBDC MOF in the region of 1630-400 cm^{-1} (PEO affected by MgBDC MOF)

When the nanosized MgBDC MOF was incorporated into the PEO-LiTFSI system, the absorption peaks of pure LiTFSI changed. The observed $v_a(SO_2)$ vibration peaks at 1354-1352 cm^{-1} in the PEO-LiTFSI system shifted to 1351-1349 cm^{-1}, the band at 1341 cm^{-1} was no change. A new peak at 1330-1310 cm^{-1} was obtained in the PEO-LiTFSI-MgBDC MOF system as shown in Figure 4.17. The bands of $v_{as}(CF_3)$ vibration mode shifted from 1240-1232, 1191 to 1233-1227, 1189-1185 cm^{-1}. $v_s(SO_2)$ vibration modes shifted from 1144-1143 to 1142-1132 cm^{-1}. The v_s(S–N–S) vibration modes shifted from 1057 to 1057-1054 cm^{-1}. The band at 788-787 cm^{-1} was no change. Peak of v(C–S) vibration mode at 761-760 cm^{-1} disappeared. The band of the $\delta_s(CF_3)$ vibration mode at 739 cm^{-1} was no change. δ(S–N–S) mode shifted from 654-653 to 652-651 cm^{-1} and $\delta_a(SO_2)$ in-plane and out-of-plane deformation mode shifted from 616-615, 601-600 to 614-613, 600-598 cm^{-1}, respectively. The $\delta_a(CF_3)$ modes shifted from 510 to 509 cm^{-1}. The band at 570-569 cm^{-1} was no changed as shown in Figure 4.17. The decreases, increases, or absents of peaks in the FT-IR spectrum are the

desired situation. This situation can be explained that these bands bonded with organic compounds from MgBDC MOF. Also, there has a relationship between the proportion of MgBDC MOF and lithium salt added to the PEO-LiTFSI system. Correspondingly, it can be said that as the amount of lithium salt and MgBDC MOF increases, it absorbs more and bonds better. As a result of the made analyses, PEO-based electrolytes containing 20 wt.% lithium salt and 5 wt. % MgBDC MOF may be more amorphous structures.

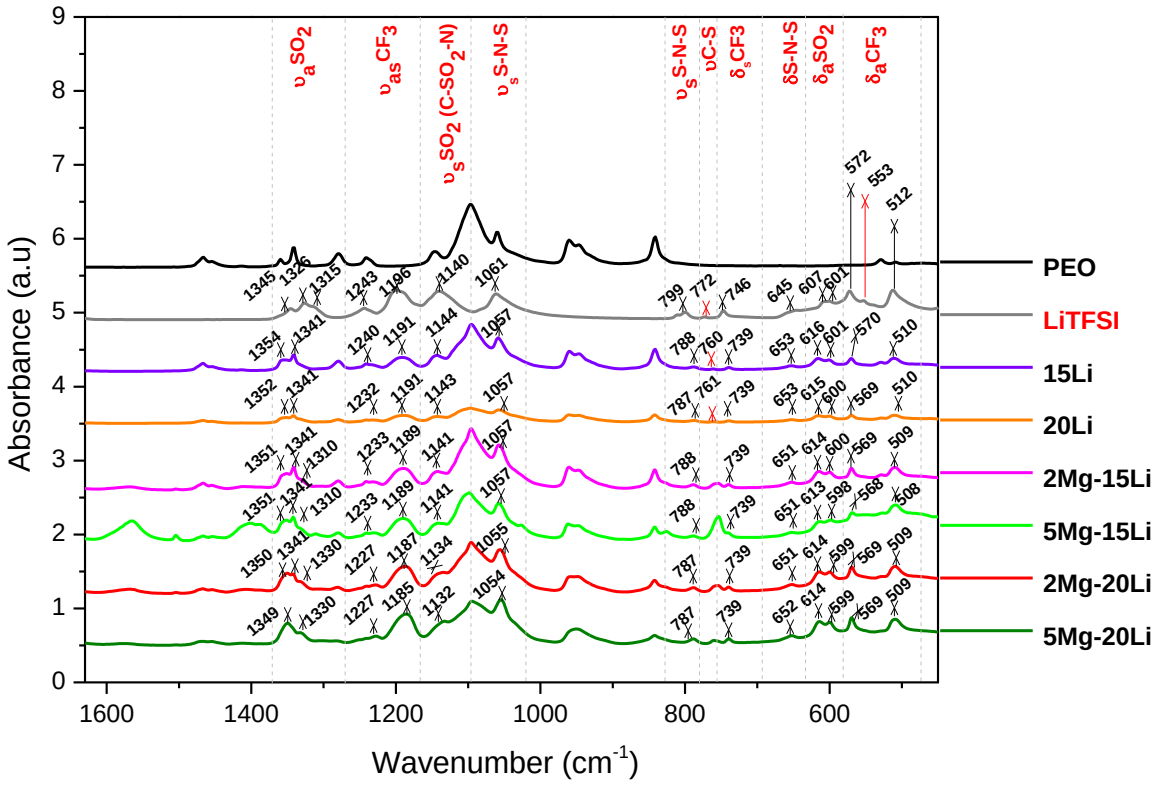

Figure 4.17. ATR FT-IR results of PEO based NCPEs containing MgBDC MOF in the region of 1630-400 cm^{-1} (LiTFSI affected by Mg-BDC MOF)

After adding MgBDC MOF nanocomposite to the PEO-LiTFSI system, the v_a(COOH) vibration modes groups shifted from 1567, 1503 to 1578-1565, 1504 cm^{-1}. The v_s(COOH) vibration modes groups shifted from 1397, 1311 to 1466-1468, 1401-1411 cm^{-1} in the PEO-based NCPE system. The bands of (C–H) in-plane and out-of-plane vibration modes observed at 1155 and 1103 cm^{-1} have no appeared. The band at

1023 shifted to 1026 cm^{-1} and the shape, intensity, and position of its change in the PEO-LiTFSI-MgBDC MOF system as shown in Figure 4.18. This case can be explained that this band bonded with C–SO_2–N bonds from PEO and lithium salt. The peak of υ(Mg–O) vibration was replaced from 825 to 826 cm^{-1}. *δ*(Mg–O) vibration shifted from 752 to 760-753 cm^{-1}. In the PEO-LiTFSI-MgBDC MOF system, the band of *υ*(Mg–O) vibration mode at 517 cm^{-1} disappeared or this band was linked to the PEO-LiTFSI structure. As stated previously in the PEO-LiTFSI system, there is a similar situation in the PEO-LiTFSI-MgBDC MOF system in terms of the disappearances, increases, or decreases of the peaks. This means that the organic components may be bounded to the structure or absorbed as desired. On the other hand, it can be said that more absorption and bonding were observed in the structure due to the rise in the amount of both Li salt and MgBDC MOF nanoparticles. In other words, this can be stated that PEO-based NCPEs containing 20 wt. % lithium salt and 5 wt. % MgBDC MOF, sample 5Mg-20Li may be more suitable for solid polymer electrolytes.

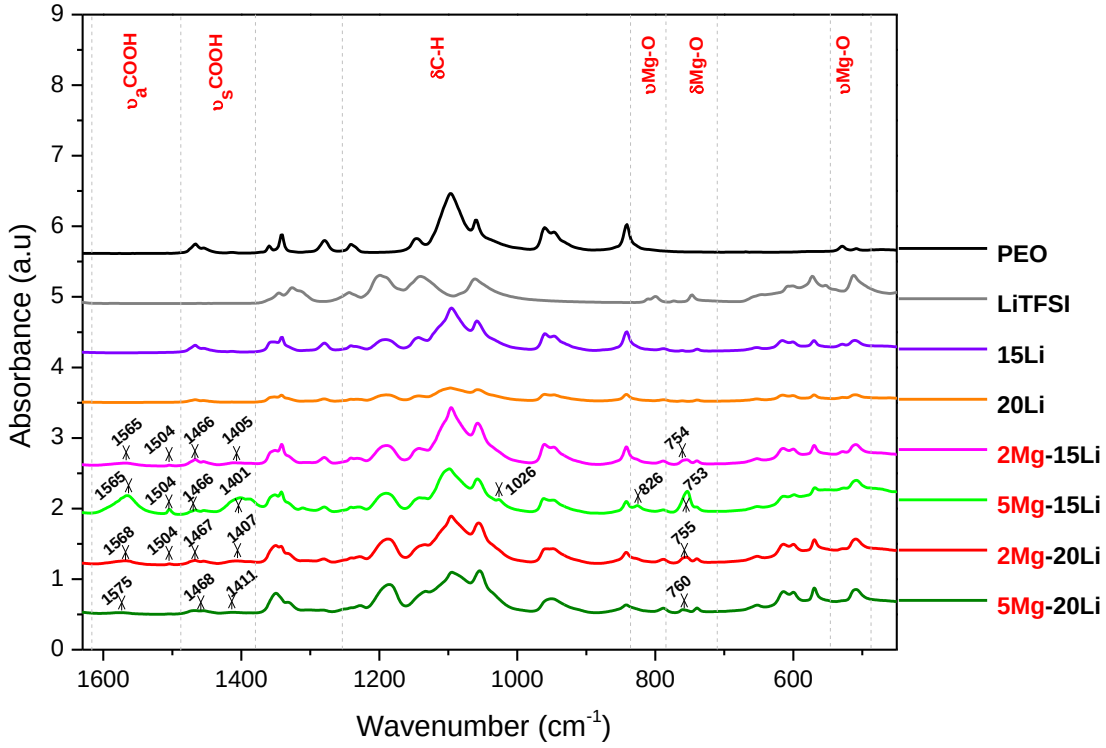

Figure 4.18. ATR FT-IR results of PEO based NCPEs containing MgBDC MOF in the region of 1630-400 cm^{-1} (MgBDC MOF affected by PEO-LiTFSI)

Table 4.2. ATR FT-IR spectrum results and vibration modes of pure PEO electrolyte, PEO-LiTFSI, and PEO-LiTFSI-MgBDC

Vibration modes	Pure PEO of wavenumbers (cm^{-1})	PEO-LiTFSI of wavenumbers (cm^{-1})	PEO-LiTFSI-MgBDC MOF of wavenumbers (cm^{-1})
υ(C–H)	2881	2877	2879-2877
CH_2 scissoring	1466	1465	1467
δ(CH_2)	1360, 1341	1354, 1340	1355-1350, 1342-1331
Asym. CH_2 twisting	1279, 1240	No change, 1234	No change, 1236-1228
υ_{as}(C–O–C)	1146, 1096, 1060	1142, 1094, 1056	1143-1135, 1099-1093, 1056-1055
Symm. CH_2 twisting	960, 946	No change, No change	962-950, No change
CH_2 wagging	841	840	No change
υ_{as}(C–O–C)	528, 508	No change, 509	No change, No change

Table 4.3. ATR FT-IR spectrum results and vibration modes of pure LiTFSI, PEO-LiTFSI, and PEO-LiTFSI-MgBDC

Vibration modes	Pure LiTFSI of wavenumbers (cm^{-1})	PEO-LiTFSI of wavenumbers (cm^{-1})	PEO-LiTFSI-MgBDC MOF of wavenumbers (cm^{-1})
$\upsilon_a(SO_2)$	1345,1326, 1315	1354-1352, 1341, Absent	1351-1349, No change, 1330-1310
$\upsilon_{as}(CF_3)$	1243, 1196	1240-1232, 1191	1233-1227, 1189-1185
$\upsilon_s(SO_2)$	1140	1144-1143	1142-1132
υ_s(S–N–S)	1061	1057	1057-1054
υ_s(S–N–S)	799	788-787	No change
υ(C–S)	772	761-760	Absent
$\delta_s(CF_3)$	746	739	No change
δ(S–N–S)	645	654-653	652-651
In-plane of $\delta_a(SO_2)$	607	616-615	614-613
Out-of-plane of $\delta_a(SO_2)$	601	601-600	600-598
$\delta_a(CF_3)$	572, 553, 512	570-569, Absent, 510	No change, No change,509

Table 4.4. ATR FT-IR spectrum results and vibration modes of MgBDC MOF and PEO-LiTFSI-MgBDC MOF

Vibration modes	MgBDC MOF powder of wavenumbers (cm^{-1})	PEO-LiTFSI-MgBDC MOF of wavenumbers (cm^{-1})
υ_a(COOH)	1567, 1503	1578-1565, 1504
υ_s(COOH)	1397, 1311	1468-1466, 1401-1411
In-plane / out-of-plane of δ(CH)	1155, 1103, 1023	Absent, Absent, 1026
υ(Mg–O)	825	826
δ(Mg–O)	752	760-753
υ(Mg–O)	517	Absent

4.8. TGA Results of PEO Based NCPEs Containing MgBDC MOF

TGA analysis results of pure PEO, PEO-Li, and PEO-based NCPEs containing MgBDC MOF in the range of 0-1000 °C are shown in Figures 4.19 (a). The zoomed ones of temperatures in the range of 0-400 and 350-450 °C are given in Figure 4.19 (b-c), respectively. Thermal decomposition results of pure PEO, PEO-LiTFSI and PEO-based NCPEs containing MgBDC MOF systems are shown in Figure 4.20. $T_{d,\ 95\%}$, $T_{d,\ 85\%,}$ and $T_{d,\ max}$ values of pure PEO, PEO-LiTFSI, and PEO-based NCPEs containing MgBDC MOF are given in Table 4.5.

The first weight loss of less than 1% from 20 to 100 °C is obtained and this loos of weight is attributed to the taking apart from humidity and residues of solvent structure as demonstrated in Figure 4.19 (b) (Mathew et al., 2019; Uma et al., 2005). After adding LiTFSI salt into the PEO substance, the irreversible degradation started about 368 and 202°C for polymer electrolytes containing 15 wt. % and 20 wt. % lithium salt, respectively as given in Figure 4.19 (b-c). The second weight losses find at temperatures above 200 °C and these losses are corresponding to the decomposition of PEO (Mathew et al., 2019). The irreversible thermal decomposition in the PEO-LiTFSI system observes above 350 °C (Mathew et al., 2019). It was found about 399 and 393°C for the PEO-based electrolyte containing 15 wt. % and 20 wt. % lithium salt, respectively. The weight loss of 10 % was obtained from 277 to 399 °C for PEO-based electrolyte containing 15 wt. % lithium salt and the weight loss of 7% was at temperatures between 288 and 393 °C for PEO-based electrolyte containing 20 wt. % lithium salt. When the blending of MgBDC MOF filler to PEO-LiTFSI system, the

resistance to thermal of polymer electrolytes improved. The thermal decompositions of them took place at about 360-390 °C as given in Figure 4.20. The total average loss of weight of them was found to be 78.5 % at temperatures between 390 and 560°C. It has been seen that the thermal stability of PEO-based NCPEs has reached above 360 °C (Mathew et al., 2019).

$T_{d,\,95\%}$ values of PEO-based NCPEs were found to be shorter than PEO as shown in Figure 4.20 and Table 4.5. This situation can be explained as follows. As DMF solvent deteriorates to formic acid, dimethylamine, carbon dioxide, hydrogen cyanide, and carbon monoxide. It may also be possible for some contaminations to occur at extreme temperatures (Burgaz et al., 2019). Therefore, it may be related to the solvent used. $T_{d,\,85\%}$ values of PEO-based NCPEs increased with the addition of 2 and 5 wt.% nanosized MgBDC MOF to the PEO-LiTFSI system. As given in Figure 4.20 and Table 4.5, $T_{d,\,85\%}$ values of 2Mg-15Li, 5Mg-15Li, 2Mg-20Li were obtained at temperatures 389, 392, 390°C, respectively. However, $T_{d,\,85\%}$ values of 5Mg-20Li sample was found to be about 363°C. The 5Mg-20Li sample started thermal decomposition earlier according to other samples. This may be related to the proportion of lithium salt. The $T_{d,\,max}$ values of 2Mg-20Li and 5Mg-20Li samples were found to be at 430 and 427 °C, respectively and these were the highest values. These values are extremely important in terms of ionic conductivity measurements. It has given films a strong barrier effect in terms of thermal degradation by the addition of nanosized MBDC MOF to the PEO-LiTFSI system. The improved thermal stability of NCPEs has corresponded to the shielding effect (Angulakshmi et al., 2014).

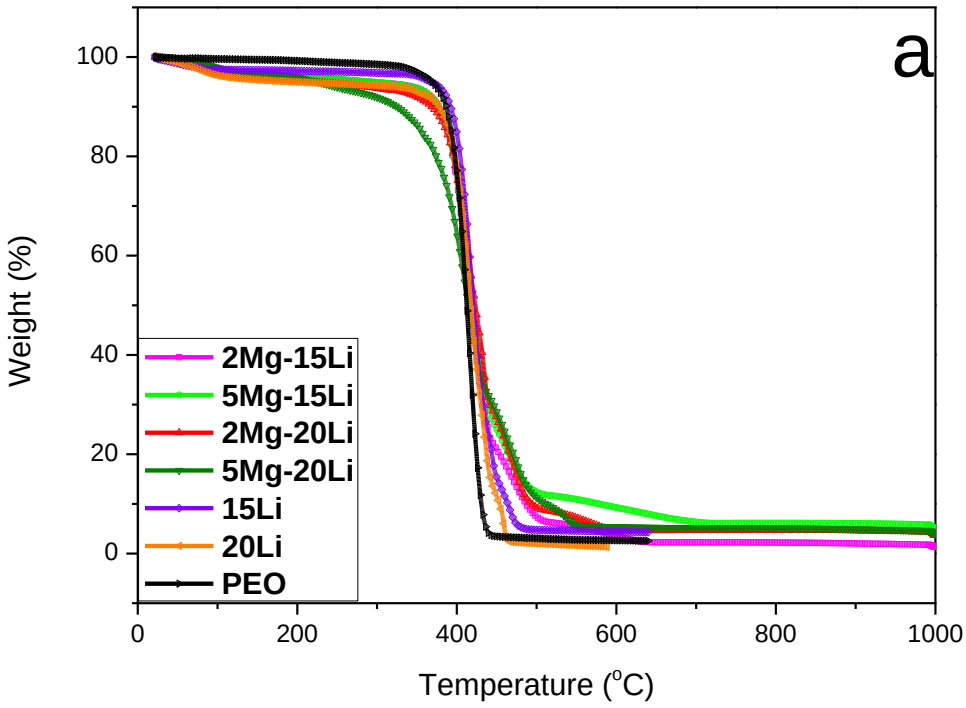
a
Weight (%)
Temperature (°C)
2Mg-15Li
5Mg-15Li
2Mg-20Li
5Mg-20Li
15Li
20Li
PEO

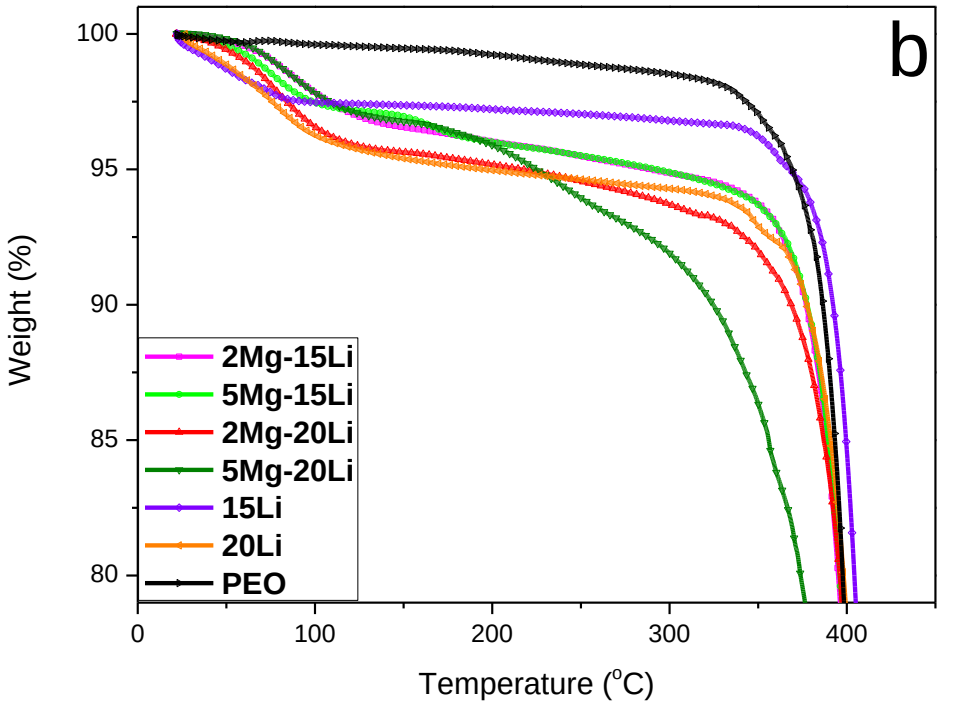
b
Weight (%)
Temperature (°C)
2Mg-15Li
5Mg-15Li
2Mg-20Li
5Mg-20Li
15Li
20Li
PEO

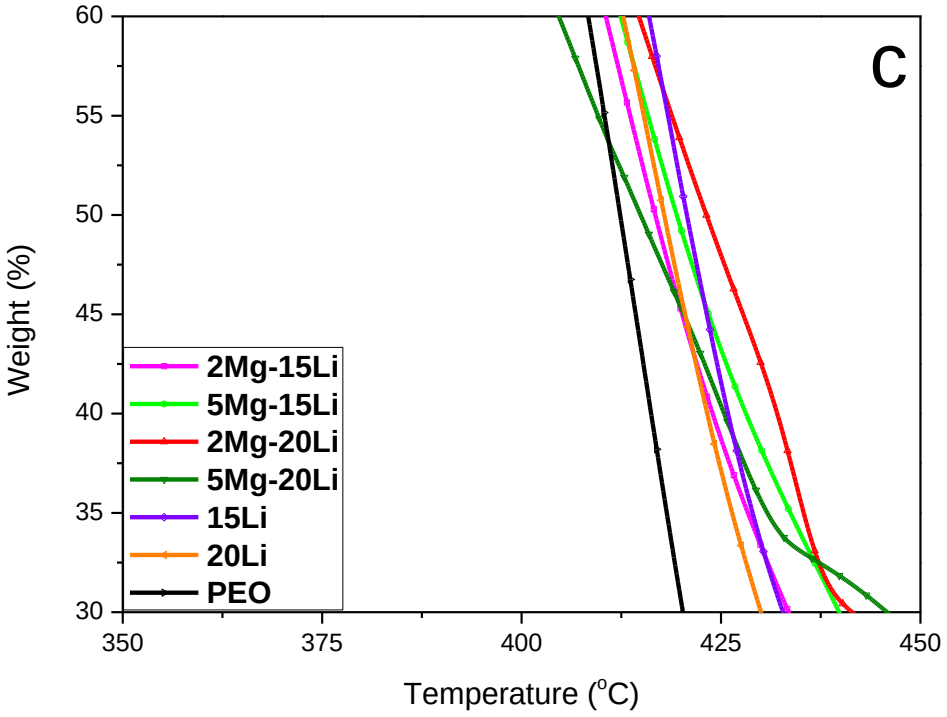

Figure 4.19. (a) TGA analysis results of pure PEO, PEO-Li, and PEO based NCPEs containing MgBDC MOF in the range of 0-1000 °C (b) The zoomed TGA analysis results of pure PEO, PEO-Li and PEO based NCPEs containing MgBDC MOF in the range of 0-400 °C (c) The zoomed TGA analysis results of PEO based NCPEs containing MgBDC MOF in the range of 350-450 °C

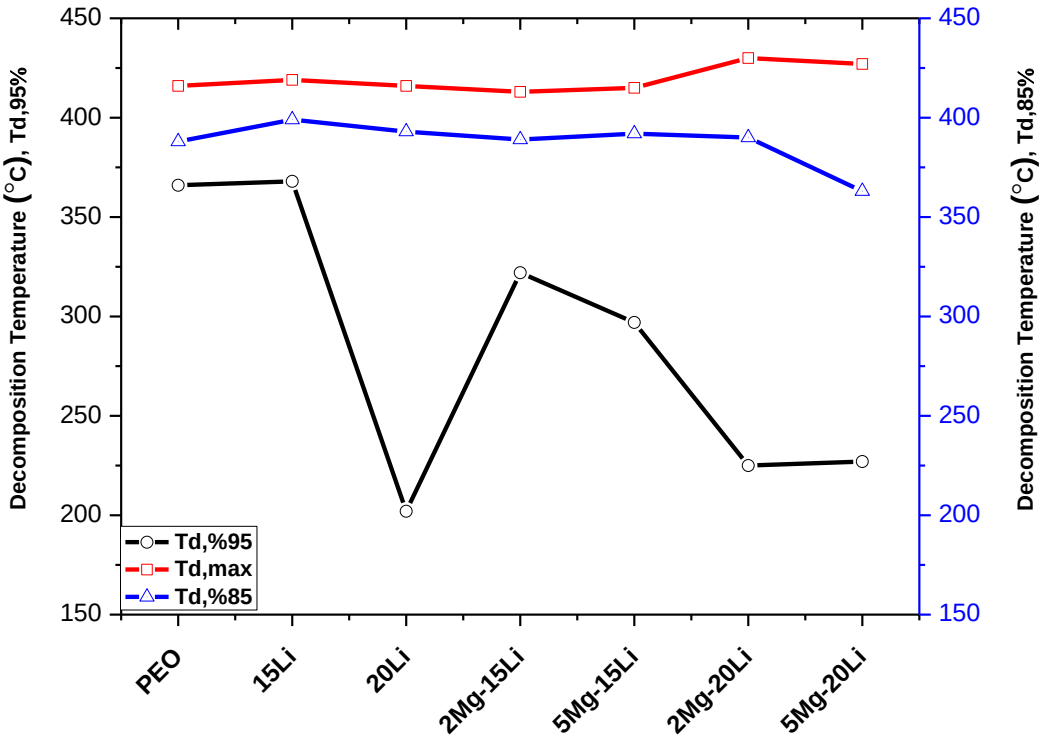

Figure 4.20. Thermal decomposition results of pure PEO, PEO-Li, and PEO based NCPEs containing MgBDC MOF

Table 4.5. The thermal decomposition values of pure PEO, PEO-LiTFSI, and PEO based NCPEs containing MgBDC MOF

Sample code	$T_{d, 95\%}$ (°C)	$T_{d, 85\%}$ (°C)	$T_{d, max}$ (°C)
PEO	366	388	416
15 Li	368	399	419
20 Li	202	393	416
2Mg-15Li	322	389	413
5Mg-15Li	297	392	415
2Mg-20Li	225	390	430
5Mg-20Li	227	363	427

4.9. DSC Analysis Results of PEO Based NCPEs Containing MgBDC MOF

DSC curves of pure PEO, PEO-based SPEs, and NCPEs are given in Figure 4.21 (a-b). The T_m, T_g, ΔH_m, and X_c (%) values were computed from DSC curves and they are shown in Table 4.6. As shown in Figure 4.21 (a) and Table 4.6, T_m of pure PEO, 15Li, and 20Li samples was found at 66.5, 66.28, and 62.55 °C, respectively. T_m values of 2Mg-15Li, 5Mg-15Li, 2Mg-20Li, 5Mg-20Li samples were obtained at temperatures 58.74, 59.13, 50.94, and 50.09 °C, respectively. As seen, the intensity of pure PEO melting peak regularly reduces as the content of nanosized MgBDC MOF and lithium salt rises. So, the mixture of lithium salt and nanosized MgBDC MOF into PEO strongly restricts crystallization and reduces the content of the crystalline structure of the polymer. In other words, the decrease in T_m value improves the amorphous property of the sample (Mathew et al., 2019; Hema et al., 2009)**.** On the other hand, after the incorporation of Li salt and MgBDC MOF nanoparticles into the polymer matrix, the area and position of the PEO melting peak have been exposed to change (Angulakshmi et al., 2014).

In Figure 4.21 (b), T_g of pure PEO, 15Li and 20Li polymer electrolytes was observed at temperatures -53.58, -33.27 and -34.94°C, respectively ($T_{g15Li} > T_{g20Li} > T_{gPEO}$). It can be seen that T_g increases on the incorporation of lithium salt into polymer electrolyte film with a corresponding decrease in T_m. An increase of about 20 and 18°C was determined for 15Li and 20Li polymer electrolytes. After adding MOF filler into the PEO-LiTFSI system, T_g values of PEO-based NCPEs decreased slightly. T_g values of 2Mg-15Li, 5Mg-15Li, 2Mg-20Li, 5Mg-20Li samples were found at temperatures -38.56, -35.32, -38.21 and -39.05 °C, respectively. According to these results, the Tg value order of magnitude is as follows: $T_{g15Li} > T_{g20Li} > T_{g5Mg\text{-}15Li} > T_{g2Mg\text{-}20Li} > T_{g2Mg\text{-}15Li} > T_{g5Mg\text{-}20Li} > T_{gPEO}$. It was determined that T_g values of NCPEs increased compared to pure polymer. However, it was observed that T_g values decreased slightly compared to PEO-based SPEs. A decrease may be observed at temperatures between approximately 2 and 5°C in T_g of polymer membranes due to the crystal structure of the metal-organic framework. The addition of nanosized MgBDC MOF filler into the PEO-LiTFSI system contributes to the increase in free volume and local chain flexibility by reducing T_g. The decrease in T_g of NCPEs electrolyte film shows enhanced flexibility of polymer chain (Polu and Rhee, 2017). Also, this change in the T_g value may correspond to the amorphization due to the mixing of MOF filler and Li

salt into PEO. also, it may be related to the interactivity of Li^+ and Mg^{2+} cation ions with ethylene oxide (EO) from the PEO compound. matrix (Mathew et al., 2019). To summarize, the T_g value decrease in MOF-doped nanocomposite polymer electrolytes was the result of the interaction of oxygen in the EO part together with Lewis acidic regions in MOFs. The interaction between ethylene oxide chains has improved the mobility of the amorphous side of PEO polymer with MOF fillers. Thus, free volume and chain elasticity were increased by lowering T_g. In a sense, it can be said that there is a 2.5% free volume increase in polymer materials. The ΔH_m° is pure 100% crystalline PEO phase. The amount of ΔH_m° in pure PEO is taken as 196.4 J/g (Gupta et al., 2016; Burgaz, 2011). The values of ΔH_m and X_c (%) of pure PEO electrolyte, PEO-LiTFSI system, and PEO-based NCPEs containing MgBDC MOF are compared in Figure 4.22 and Table 4.6. The T_m and degree of crystallinity (X_c) values of polymer electrolyte films dramatically decreased when 20 wt.% LiTFSI salt was combined with PEO (Gupta et al., 2016). LiTFSI salt has a strong electron-withdrawing group (SO_2CF_3) and the salt dissolution occurs because the $–SO_2–N–SO_2–$ the functional group from the $TFSI^-$ anion exhibits high elasticity (Chaurasia et al., 2011). As in previous studies, it was estimated that the degree of crystallinity (X_c) can decrease when lithium salt is incorporated into the PEO structure (Polu and Rhee, 2017). The mixing of nanosized MgBDC MOF into the PEO-LiTFSI system decreased both the T_m and X_c of the PEO (Gupta et al., 2016; Angulakshmi et al., 2014). As given in Table 4.6, X_c (%) values of PEO-based SPEs and NCPEs decreased as the amount of lithium salt and nanosized MgBDC MOF increased. The T_g of the polymer electrolyte film was decreased by adding nanosized MgBDC MOF to the PEO-LiTFSI system and in addition to this, contributed to increase chain elasticity and free volume of polymer material. As far as is known, the rise in chain elasticity is a measurement of the ability of polymer chains to rotate around chemical links. A reduction in T_g value can help in the easy movement of ions thanks to the rich structure of inorganic fillers. Thereby, an increase desired in value of ionic conductivity can be observed (Polu and Rhee, 2017). In other words, the intermolecular force between LiTFSI salt, nanosized MgBDC MOF, and carboxylic acid of PEO causes the ionic conductivity of polymer electrolyte films to increase (Polu and Rhee, 2017; Karuppasamy et al., 2016).

ΔH_m and X_c (%) values decrease continually as a function of the mixing of lithium salt and nanosized MgBDC MOF to PEO. According to the data in Figure 4.22,

the computed X_c (%) values for each polymer electrolyte indicated a further reduction in crystallinity of polymer structure after the admixture of MgBDC MOF nanoparticles into the PEO-LiTFSI system. The 2Mg-20Li and 5Mg-20Li samples reduce ΔH_m and X_c more than 2Mg-15Li and 5Mg-15Li samples. The reduction of X_c (%) with the adding of nanosized MgBDC MOF and lithium salt can be started by two potential reasons: the first one, it may be related to ethylene oxide-lithium complexation (EO/Li^+) by coordination of ether-oxygen from PEO with lithium ions. The second one may be EO/ Mg^{2+} complex due to the interaction between the cations from magnesium ions and the ether-oxygen components from PEO. The nanosized MgBDC MOF and LiTFSI salt prevented crystalline growth and reduced the polymer chain numbers that occur in crystallization fields in PEO-based NCPEs. Therefore, X_c (%) reduced and decrease in crystallinity was thought to help significantly to enhance the ionic conductivity of NCPEs.

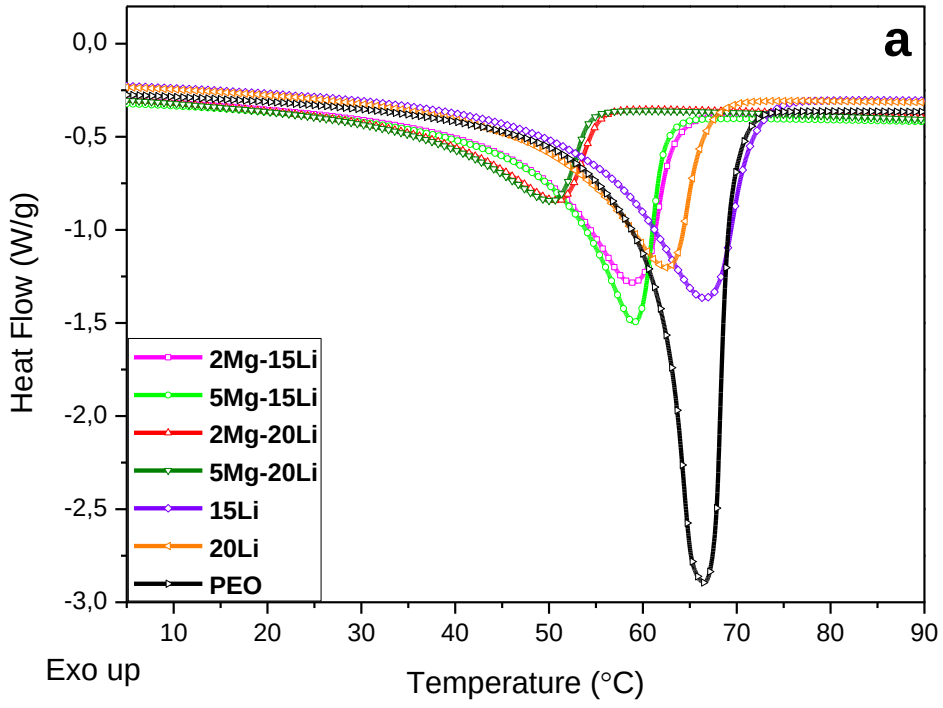

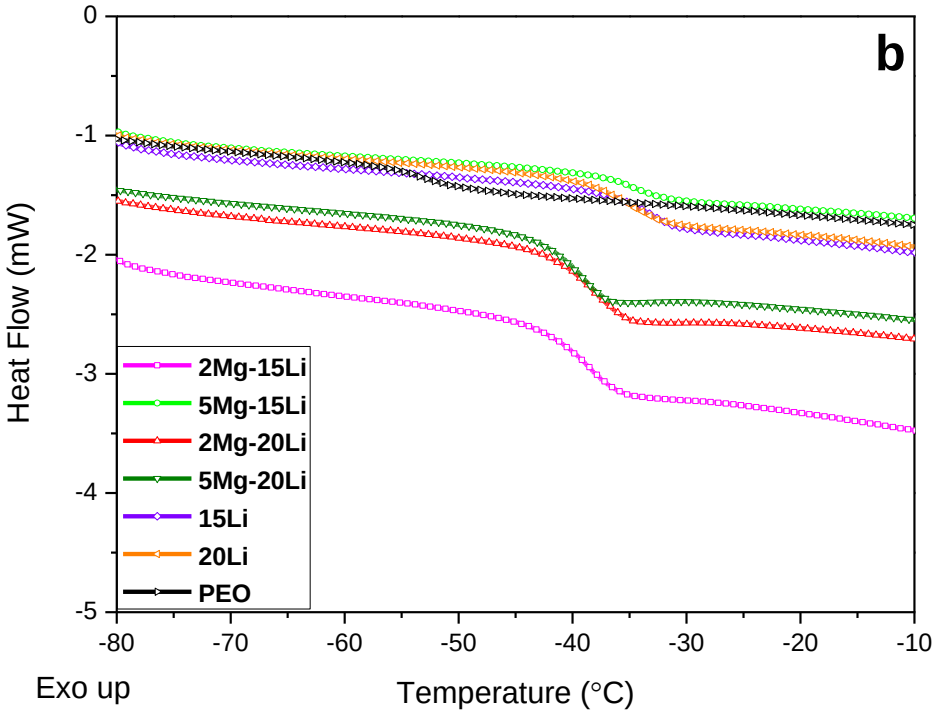

Figure 4.21. (a) T_m results of pure PEO, PEO-Li, and PEO based NCPEs containing Mg-BDC MOF (b) T_g results of pure PEO, PEO-Li, and PEO based NCPEs containing Mg-BDC MOF

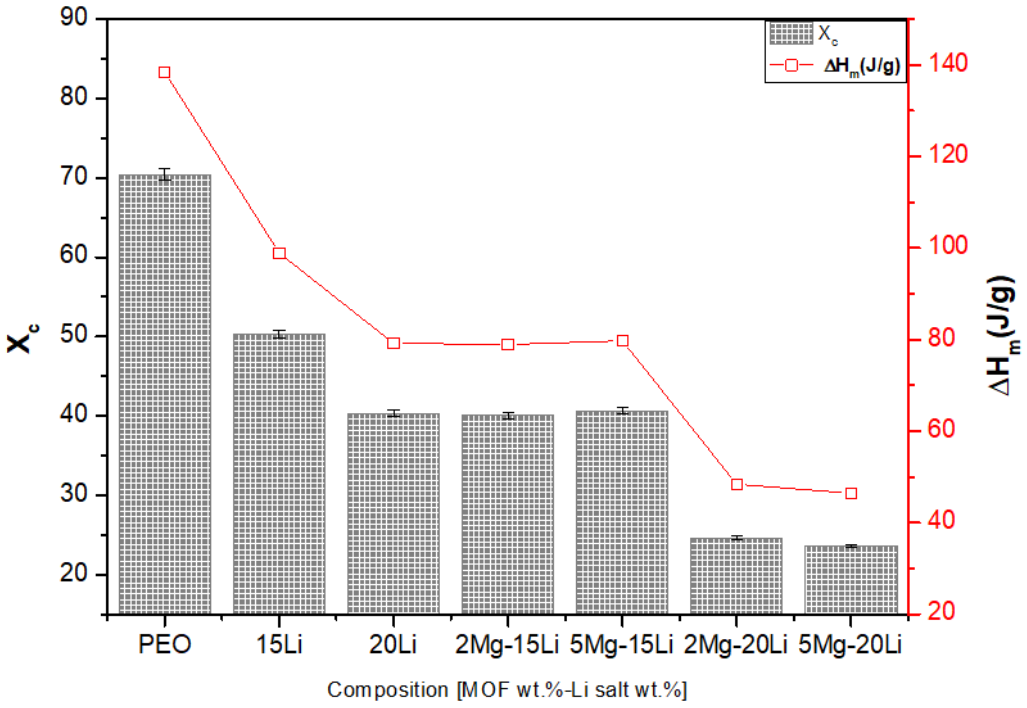

Figure 4.22. Graphical results of the calculated percent crystallinity X_c (%) and melting enthalpy (ΔH_m) values of pure PEO, PEO-LiTFSI, and PEO based NCPEs containing MgBDC MOF

Table 4.6. Numerical results of T_m, T_g, ΔH_m, X_c (%) values of pure PEO, PEO-LiTFSI and PEO based NCPEs containing MgBDC MOF

Sample code	T_m (°C)	T_g (°C)	ΔH_m (J/g)	X_c (%)
PEO	66.50	-53.58	138.4	70.4
15Li	66.50	-33.27	98.91	50.3
20Li	62.55	-34.94	79.21	40.3
2Mg-15Li	58.74	-38.56	78.94	40.1
5Mg-15Li	59.13	-35.32	79.75	40.6
2Mg-20Li	50.94	-38.21	48.39	24.6
5Mg-20Li	50.09	-39.05	46.45	23.6

4.10. XRD Analysis Results of PEO Based NCPEs Containing MgBDC MOF

The XRD patterns of PEO-based SPEs and NCPEs are given in Figure 4.23. Two characteristic peaks of PEO were observed at 2θ values of 19.1° and 23.2° which correspond to crystalline planes of (120) and (112), respectively (Tokur et al., 2016; Yoshimoto et al., 2005; Balo et al., 2017; Mohapatra et al., 2009). When LiTFSI salt is added to the polymer material, it was observed that the intensity of peaks reduces significantly because of molecular interactions between PEO and lithium salt. As a result of this interaction, polymer-lithium salt complexation occurs, and the helical structure of the polymer is disrupted to form free lithium ions in the system. In addition to this, polymer-lithium salt complexation leads to small shifts in 2θ values of main PEO peaks (Karuppasamy et al., 2016; Mohapatra et al., 2009).

Based on the crystallographic data of nanosized MgBDC MOF given in Figure 4.4, the characteristic peaks of Mg-based MOF were observed at 2θ values of 9.5°, 14.5°, 29.7°, and 44.6°, respectively. But, the peak intensities of MgBDC MOF fillers changed. The intensities of the peaks at 2θ value of 9.5°, 14.5°and 29.7° decreased visibly, while it was observed that the peak at 2θ value of 44.6° appeared and increased clarity. The anion-cation interaction between MgBDC MOF and polymer can be like the interactivity between polymer and lithium salt. Therefore, MgBDC MOF can prevent the formation of the PEO crystal package. As mentioned previously, this situation can be explained that the reduction in PEO crystallinity is caused by the penetration of MgBDC MOF into the PEO-LiTFSI system. This behavior can lead to a rise in ionic conductivity of polymer electrolytes by distortion of polymer chain reassembly.

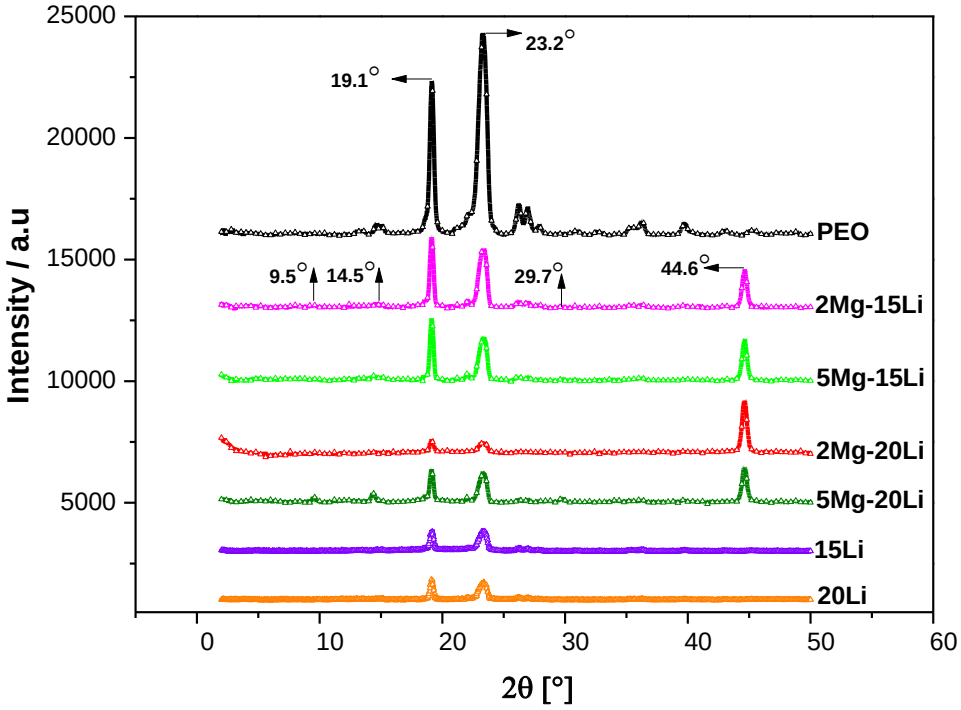

Figure 4.23. XRD analysis results of pure PEO, PEO-Li, and PEO based NCPEs containing MgBDC MOF

4.11. SEM/EDS Analysis Results of PEO Based NCPEs Containing MgBDC MOF

SEM microimages of pure PEO, PEO-based SPE, and NCPEs are given in Figures 4.24 (a-c) and 4.25 (d-f). It is confirmed by SEM that PEO has spherulites in semi-crystalline structure as shown in Figure 4.24 (a). When LiTFSI salt was combined with PEO, it was observed that the size of the spherulites was decreased as given in Figures 4.24 (b-c) (Gupta et al., 2016). On the other hand, when LiTFSI salt was added to PEO, the aggregations occurred and formed a soft form, such as foam as shown in Figure 4.24 (b). This is determined as the “breathing mode” in literature. In addition to this, it was explained that the ethylene oxide-lithium complexation forms a crystalline complex by coordinating the ether oxygen (Graebe et al., 2017). On the surface of polymer electrolytes containing lithium salt were observed some small pores. This case has corresponded to nonhomogenous evaporation of solvent during the casting of the films (Mathew et al., 2019; Evans et al., 1987).

By the penetration of nanosized MgBDC MOF materials into the PEO-LiTFSI system, it was observed that the nanomaterials were homogeneously distributed, obtained a smooth surface morphology, and embedded in the polymer as shown in Figures 4.25 (a-c). MgBDC MOF nanoparticles were ball-shaped spherical and their sizes change the ranging from 30 to 50 nm. The sizes of the MgBDC MOF-based polymer electrolytes were observed a little bit larger than the MgBDC MOF powder, however, they were less aggregated. This may be related to the good casting circumstances of polymer membrane or the absence of probable physical interactivities between polymer and surface functional groups of MgBDC MOF nanoparticles.

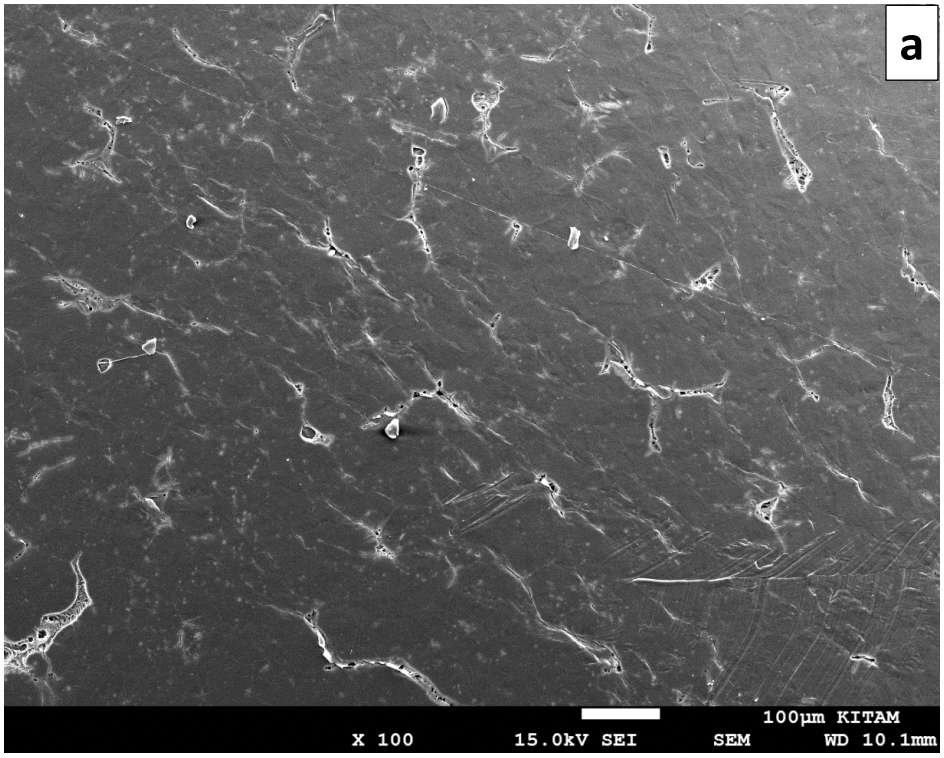

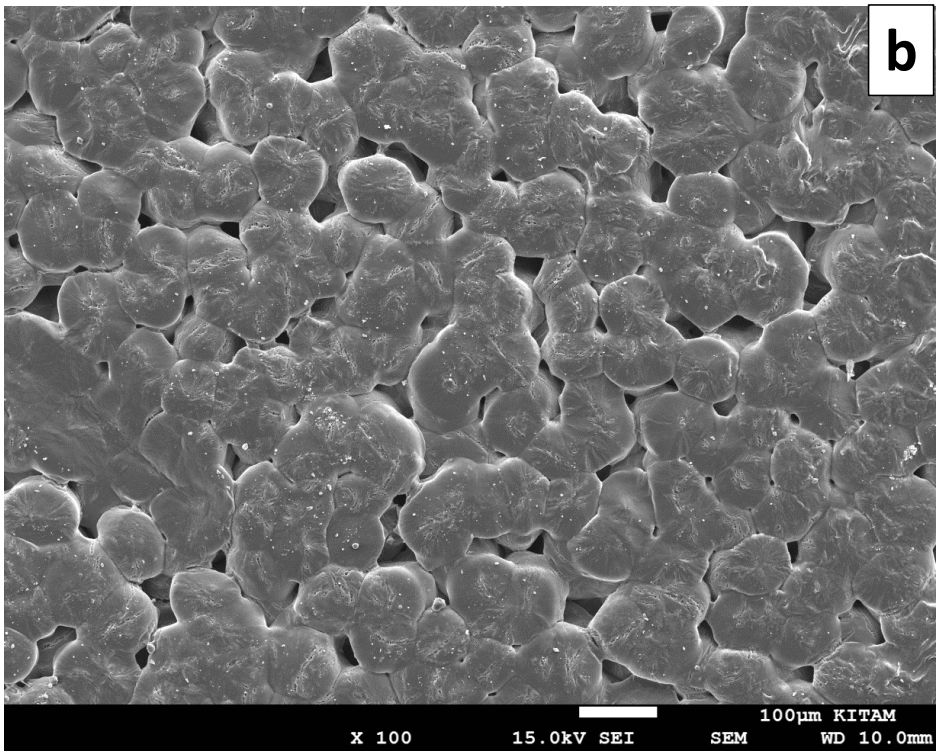

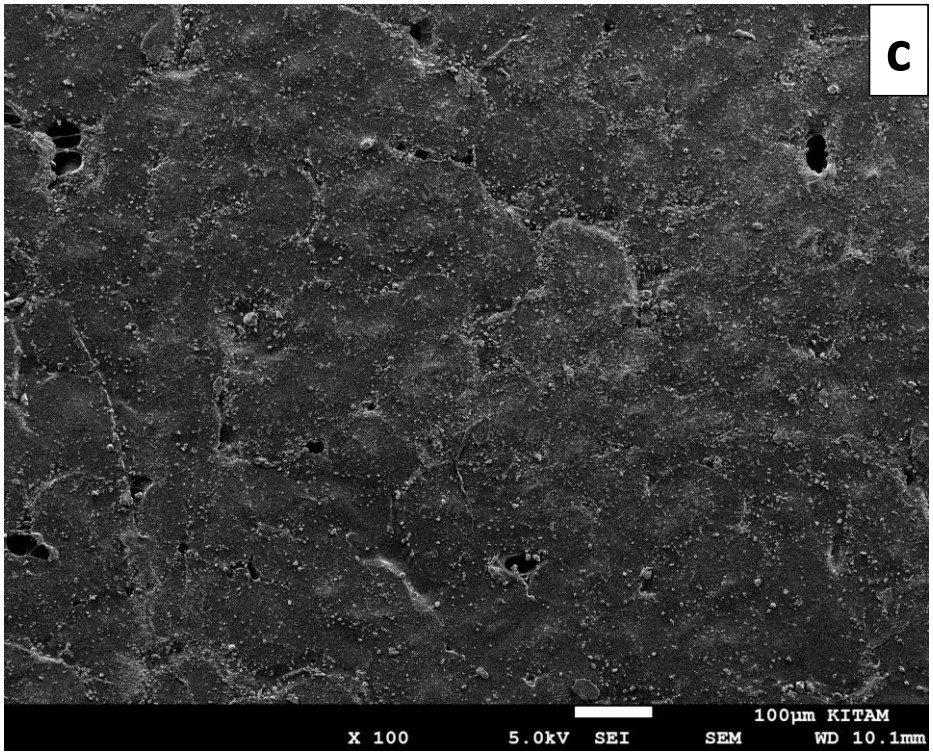

Figure 4.24. SEM analysis results of (a) pure PEO electrolyte at 100x magnification (b) 15Li polymer electrolyte 100x magnification (c) 20Li polymer electrolyte at 100x magnification

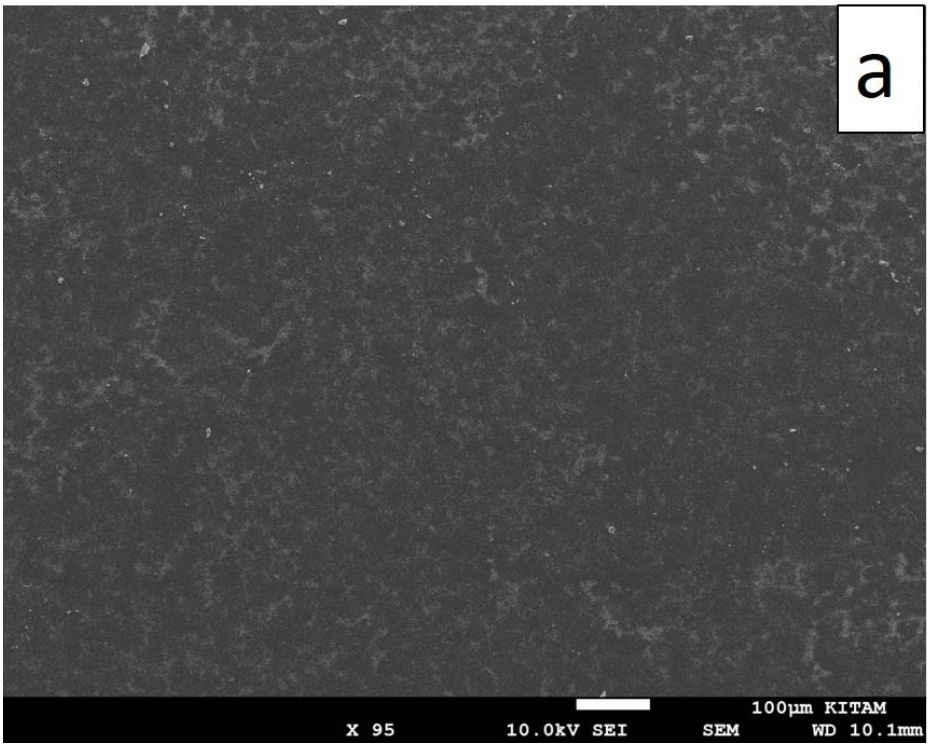
a
X 95
10.0kV SEI
SEM
100µm KITAM
WD 10.1mm

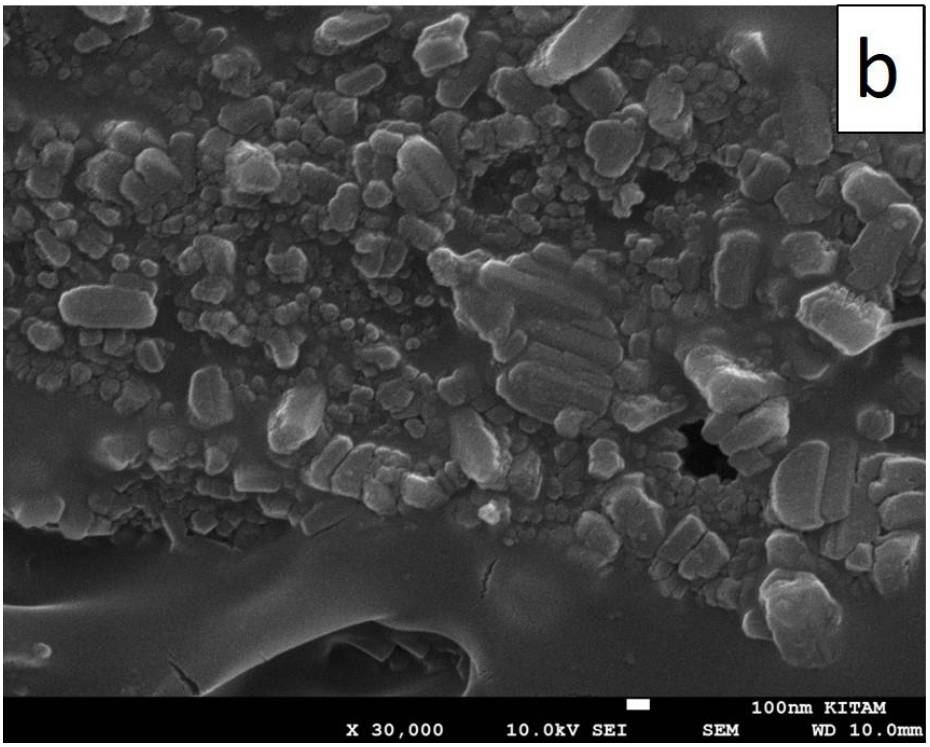
b
X 30,000
10.0kV SEI
SEM
100nm KITAM
WD 10.0mm

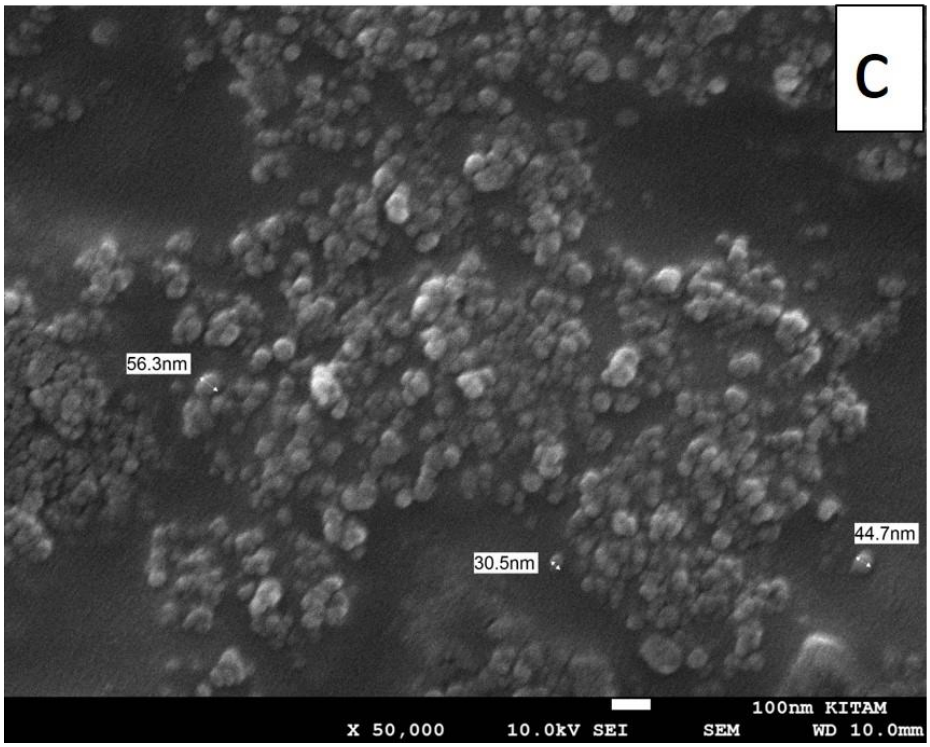

Figure 4.25. SEM analysis results of (a) PEO based NCPEs containing MgBDC MOF at 95x magnification (b) at 30,000x magnification (c) at 50,000x magnification

The chemical compounds of PEO-based NCPEs containing 5 wt. % MgBDC MOF nanoparticles and 15 wt % lithium salt was studied *via* EDS regional, mapping, and spectrum analyses are given in Figure 4.26 (a-c), respectively. Based on SEM images in Figure 4.26 (d-f) complied with EDS results of PEO-based NCPEs containing MgBDC MOF. As previously mentioned, EDS regional, mapping, and spectrum analysis results of Mg-based MOF nanoparticles supported the extreme purity of MgBDC MOF nanostructures that Mg, carbon, and oxygen have existed as shown in Figure 4.26 (a-c) (Dhawa et al., 2017). The sulfur (S) and fluorine (F) elements came from $TFSI^-$ anions and thus their presence in the polymer membrane was confirmed. As regards EDS regional-mapping results, it was verified that nanosized Mg-based MOF nanoparticles were homogeneous distribution. In the EDS spectrum, PEO-based NCPEs gave a strong peak of the Mg atom and the existence of elements such as C, O, Mg, F, and S has been verified. In previous studies, the use of nanoparticle MOFs as filling material in PEO-based SPEs enhanced mechanical, ionic conductivity, and electrochemical resistance because of the required nanoporous and

hybrid material of metal-organic framework (Yuan et al., 2013; Burgaz et al., 2019). In this respect, it can be said that SEM/EDS analysis results can improve ionic conductivity.

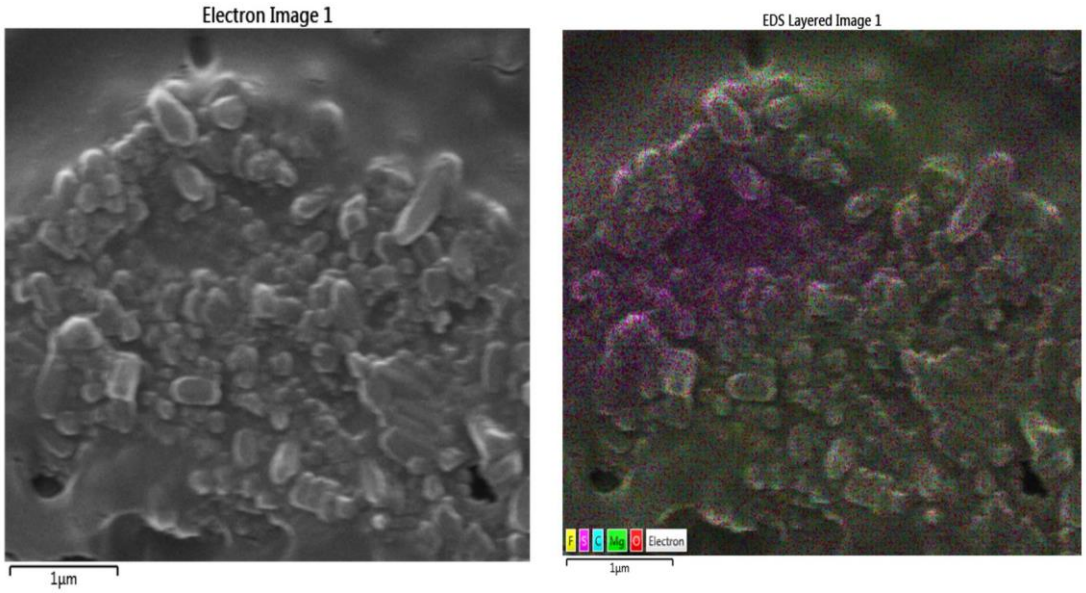

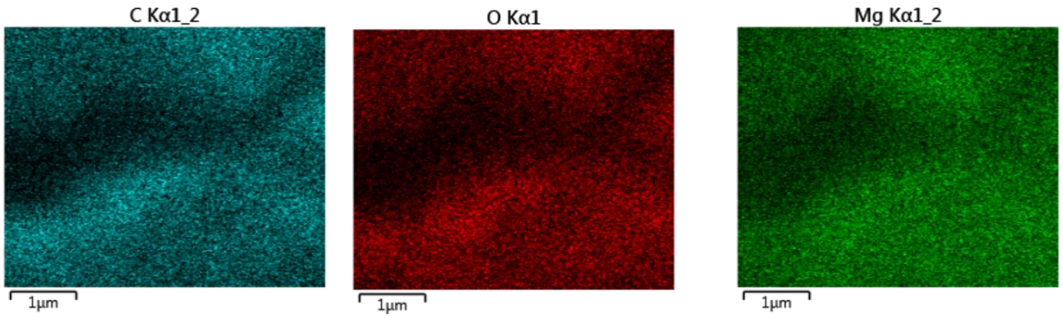

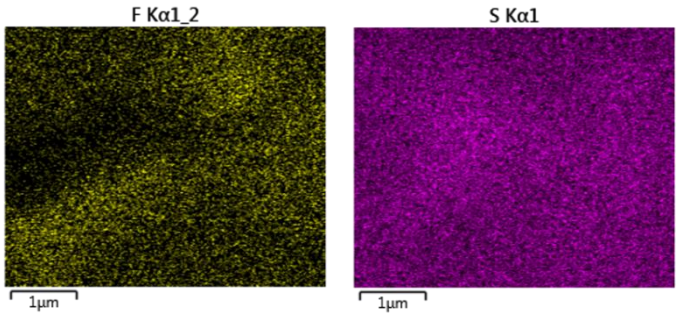

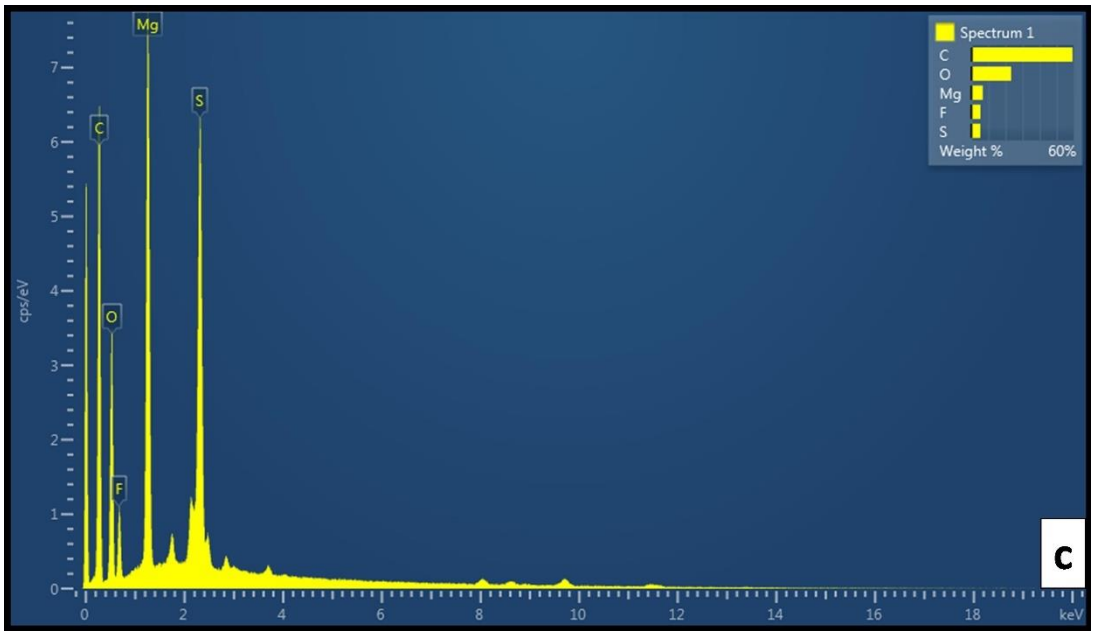

Figure 4.26. (a) EDS regional, (b) EDS mapping, and (c) EDS spectrum analysis results of nanosized MgBDC MOF

4.12. POM Analysis Results of PEO Based NCPEs Containing MgBDC MOF

The nucleation and gradual growth of spherulites in solid polymer electrolyte systems were observed by POM analysis. The polarized optical microphotographs of pure PEO, PEO-based SPEs, and NCPEs at the beginning of crystallization and after crystallization are given in Figures 4.27-33.

The usual crystalline spherulitic structure of pure PEO has been studied in Figure 4.27. As in previous studies, the first nucleation centers become visible in pure PEO. They have a homogeneous and regular spherulitic structure and also are isotropic spherical three-dimensional shapes. The lamellar crystalline nature of pure PEO along with dark boundaries has been indicated the amorphous content in the polymer (Burgaz, 2011; Kumar et al., 2011; Marzantowicz et al., 2005; Strawhecker and Manias, 2003). So, this study is consistent with previous studies.

After the complexing PEO with LiTFSI salt, the first nucleation centers become visible like pure PEO. In the 15Li and 20Li samples, which are PEO-LiTFSI systems, the dark boundaries expanded more and the spherical patterns changed significantly as

shown in Figures 4.28-29. The spherulitic structure of pure PEO became nonhomogeneous. This situation can be related to the high concentration of nucleation centers (Davies et al., 2007). The imide salt itself can perform as a nucleation substance in the PEO-Li salt system. In this case, the spherulitic occur relatively early collision with each other, due to the high density of nucleation centers. Therefore, this process leads to limitation of the size of the spherulites, and consequently, three-dimensional grain-like structures resulted. After the collision of the spherulites, their growth also got slower. The reason for this phenomenon in the previous study can be explained as the agglomeration of non-crystallizable material on the crystallization side. The imide salt agglomerated in the crystallization side may act as a plasticizer (Davies et al., 2007). This case explains that the amorphous content in the PEO-LiTFSI system has significantly increased and hence it has decreased crystallinity in the material (Dhaouadi et al., 2011; Davies et al., 2007).

As shown in Figures 4.30-33, after the nanosized MgBDC MOF was incorporated into the PEO-Li system, the first nucleation centers were not captured as in the pure PEO and PEO-Li system. Also, there was a change in light intensity as seen from the images in Figures 4.30-33. Because of the presence of 2 and 5 wt.% nanosized MgBDC MOF, the crystallization process is prevented, and thus the specific spherulite texture of pure PEO is completely broken down as given in Figures 4.30-33. Also, the spherulite sizes with PEO-based NCPEs containing MgBDC MOF have changed a lot, and they have very small contrasted with pure PEO and PEO-LiTFSI electrolyte systems. In addition to this, the spherulites turn into the anisotropic structure and non-spherical shapes (Ansari et al., 2018). This case may be related to the EO/Mg^{2+} interaction between the cations from magnesium ions and the ether-oxygen components from PEO material. Similarly, it can be related to the EO/Li^{+} interaction that occurs between anions from lithium ions and ether-oxygen coordination in PEO material. Thus, the PEO chain numbers were decreased that occur the crystallization fields in MgBDC MOF-based NCPEs. Based on POM image results, it can be said that the nanosized MgBDC MOF substance in the 5Mg-20 Li sample has a better distribution inside PEO-LiTFSI film than the other samples. This sample may be a more amorphous structure. The nanosized MgBDC MOF substance and lithium salt prevent crystalline growth. The reduction in crystallinity of the polymer complexation has been confirmed as discussed earlier in DSC and XRD results. So, the reduction in

crystallinity has made a great contribution to the enhancement of ionic conductivity of NCPE films.

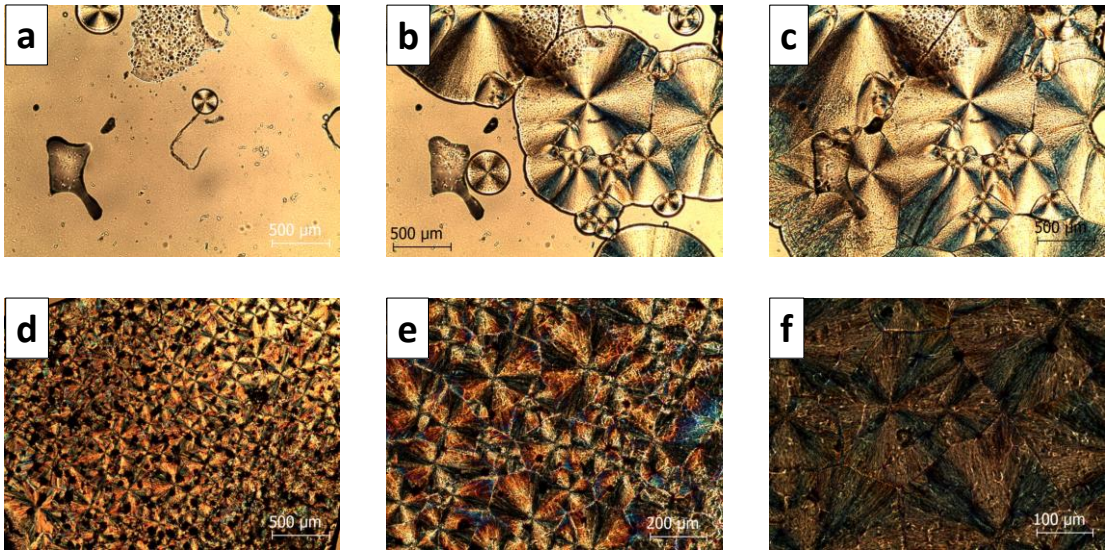

Figure 4.27. POM results of PEO a) first nucleation, b) and c) growth of spherulites, d) and e) crystallization process f) dark boundary region (scale bar 500, 200, and 100 µm)

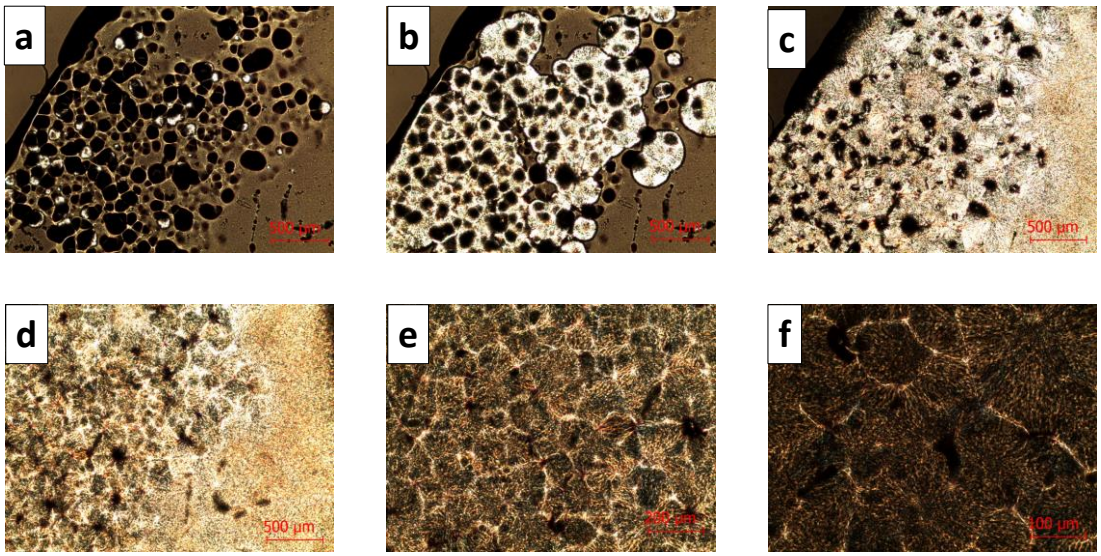

Figure 4.28. POM results of 15Li a) first nucleation, b) and c) growth of spherulites, d) and e) crystallization process f) dark boundary region (scale bar 500, 200, and 100 µm)

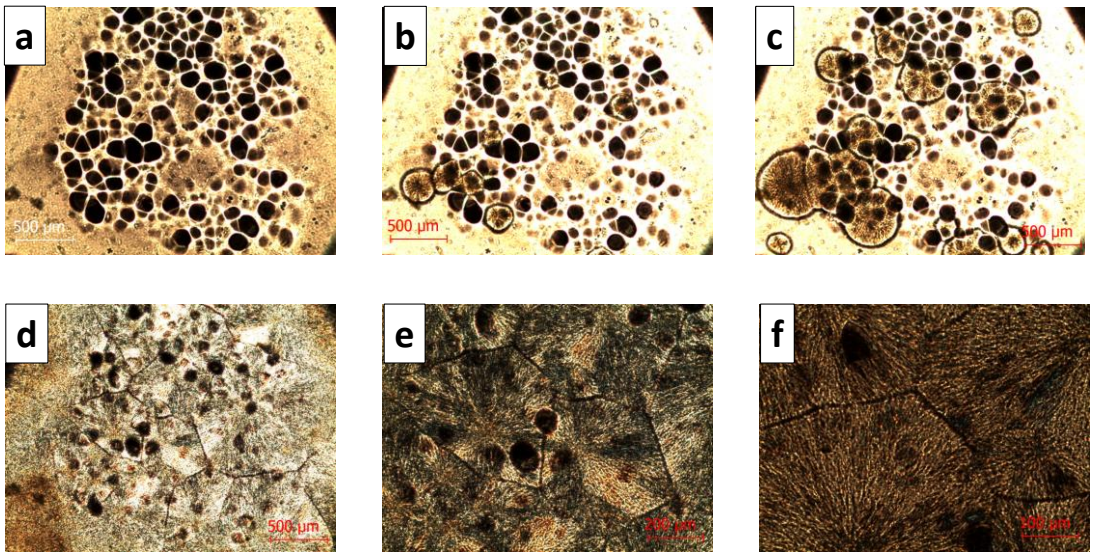

Figure 4.29. POM results of 20Li a) first nucleation, b) and c) growth of spherulites, d) and e) crystallization process f) dark boundary region (scale bar 500, 200, and 100 µm)

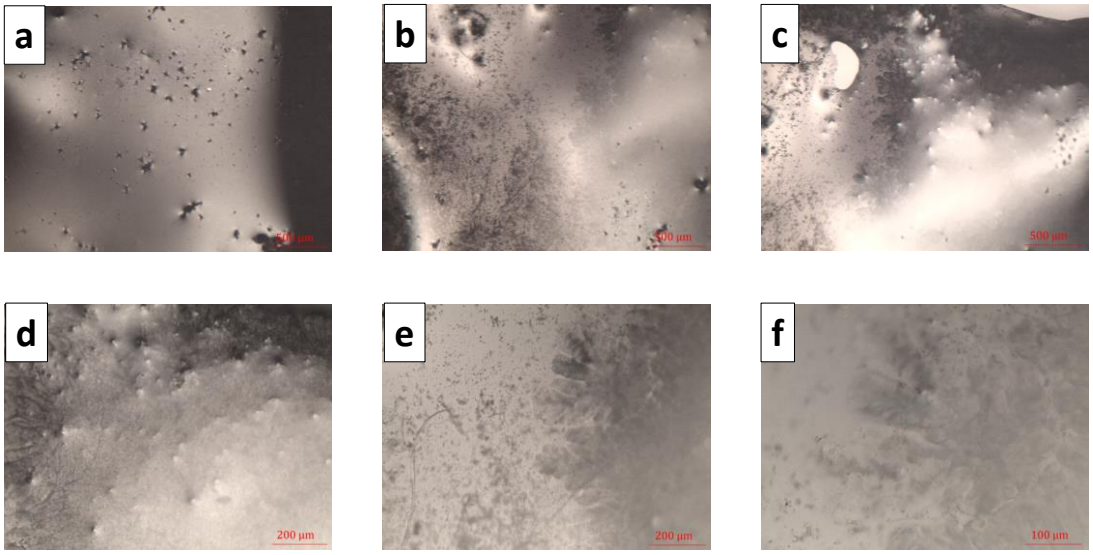

Figure 4.30. POM results of 2Mg-15Li a) first nucleation, b) and c) growth of spherulites, d) and e) crystallization process f) dark boundary region (scale bar 500, 200, and 100 µm)

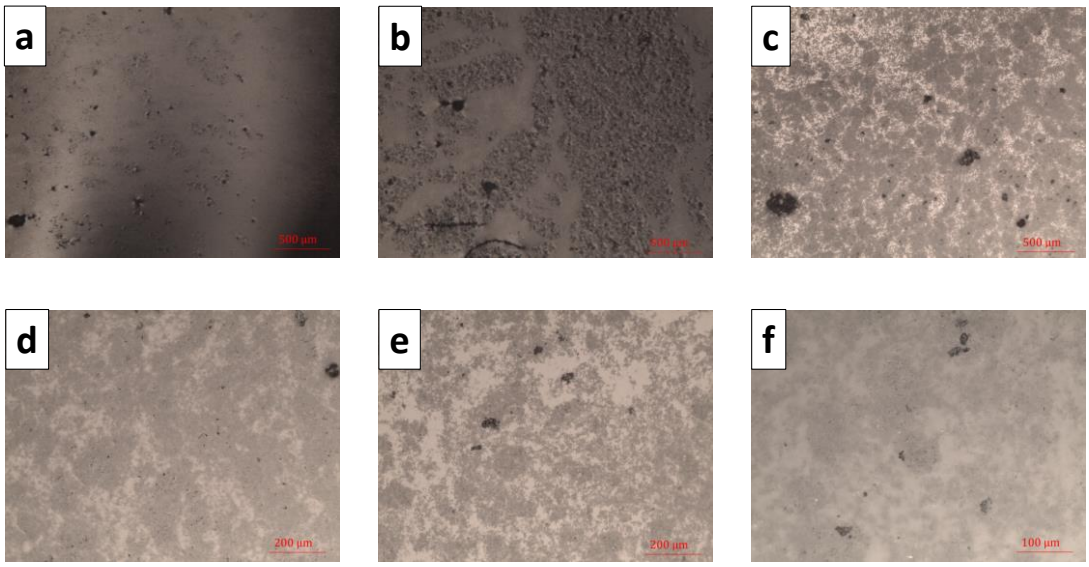

Figure 4.31. POM results of 5Mg-15Li a) first nucleation, b) and c) growth of spherulites, d) and e) crystallization process f) dark boundary region (scale bar 500, 200, and 100 μm)

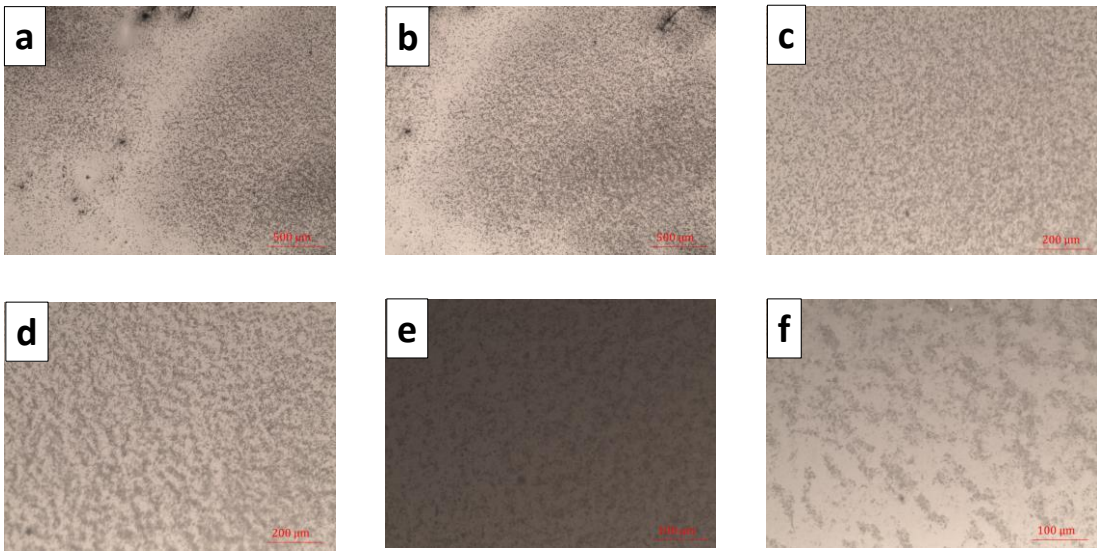

Figure 4.32. POM results of 2Mg-20Li a) first nucleation, b) and c) growth of spherulites, d) and e) crystallization process f) dark boundary region (scale bar 500, 200, and 100 μm)

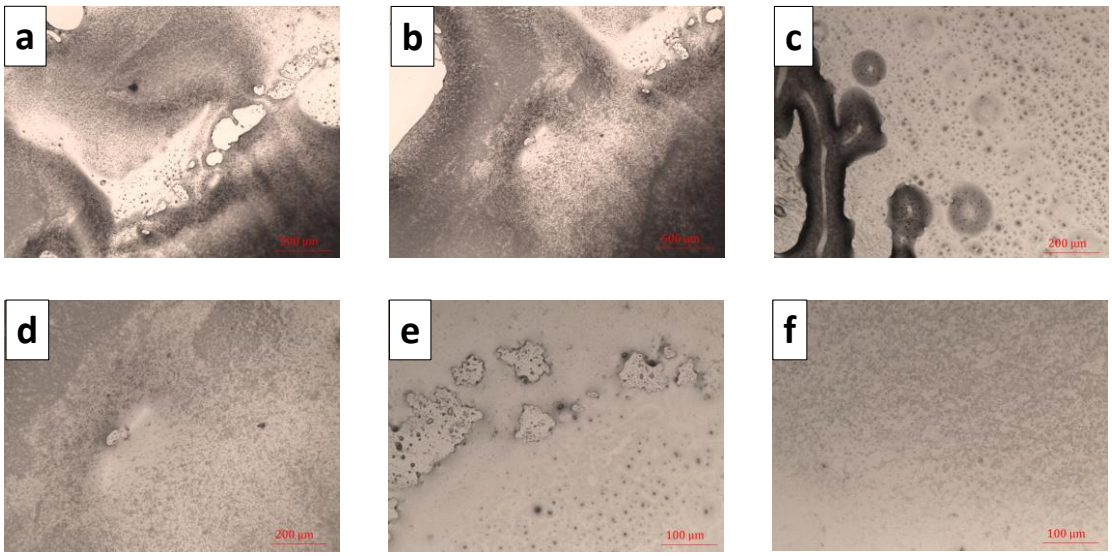

Figure 4.33. POM results of 5Mg-20Li a) first nucleation, b) and c) growth of spherulites, d) and e) crystallization process f) dark boundary region (scale bar 500, 200, and 100 μm)

4.13. EIS Analysis Results of PEO based NCPEs containing Nanosized MgBDC MOFs

The different amounts of PEO, lithium salt, and nanosized MgBDC MOF materials in PEO-based SPE and NCPE membranes prepared for making use in all-solid-state lithium polymer cells were previously given in Table 3.1. The ionic conductivity (σ) of them was studied at temperatures ranging from 30 to 60 ºC by taking into account geometry of them (width-length-thickness). The change of ionic conductivity as a function of inverse temperature for the PEO-based SPEs and NCPEs containing different amounts of lithium salt and MgBDC MOF is shown with the Arrhenius plots in Figure 4.34. The effect of the lithium salt and MgBDC MOF particle concentrations of ionic conductivity (σ) of PEO-based SPEs and NCPEs at different temperatures is given in Figures 4.35-38. Also, the numerical ionic conductivity values and thermal activation energy (E_a) values of PEO-based SPEs and NCPEs are shown in Table 4.7.

Ionic conductivity (σ) calculations were made using the equation (3.8) mentioned earlier in the physical and chemical characterization section.

$$\sigma = \frac{d}{Rb \times w \times t} \quad \textbf{(3.8)}$$

where σ (S/cm) is the ionic conductivity, d (cm) is a distance of two electrodes, R_b (ohm or Ω) is the bulk resistance taken from x-axis intersection of complicated AC impedance line, w (cm) in width and t (cm) is the thickness of the membrane.

The ionic conductivity (σ) of pure PEO polymer electrolyte is known to be about 10^{-9} S cm^{-1} at ambient temperature in literature (Polu and Rhee, 2017). As seen in Figure 4.34, it was determined that ionic conductivity (σ) of all the samples improved linearly with the increase of temperature and followed the Arrhenius type thermally activated process (Singh et all., 2017). The highest and lowest ionic conductivity at varying temperatures were determined as 5Mg-20Li and 20Li samples, respectively. It has already been supported by the literature that PEO-based solid electrolytes containing only lithium salt have lower ionic conductivity values (Graebe et al., 2017). The lowest ionic conductivity values for the 20Li sample were found to be 1.5×10^{-6} - 7.7×10^{-5} S/cm at temperatures between 30 and 60 ºC. The highest ionic conductivity values of sample 5Mg-20Li were found to be 2.85×10^{-5} and 3.26×10^{-4} S/cm at 30 and 60 ºC temperatures. The effects of LiTFSI salt and MgBDC MOF concentration on ionic conductivity of PEO-based SPEs and NCPEs at 30, 40, 50, and 60 ºC temperatures are demonstrated separately in Figures 4.35-38 and explained in more detail.

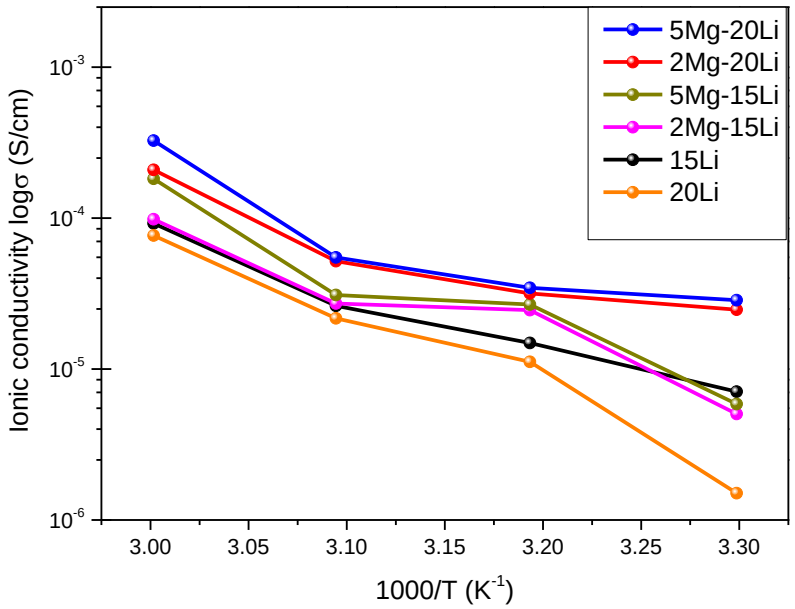

Figure 4.34. The ionic conductivity results of PEO based SPEs and NCPEs as a function of inverse temperature in the range from 30 to 60 °C (Arrhenius plot)

Figure 4.35 depicts the effects of LiTFSI salt and MgBDC MOF concentration on the ionic conductivity of PEO-based SPEs and NCPEs at ambient temperature (~30 ºC). As seen in the Figure, the ionic conductivity was reached from 10^{-9} to 10^{-6} S/cm by adding lithium salt at different concentrations to the PEO-based SPEs at 30 ºC. Ionic conductivity values of 15Li and 20Li samples were found to be 7.07×10^{-6} and 1.5×10^{-6} S cm^{-1}, respectively. Ionic conductivity of the sample 15Li, which is a PEO-based SPE containing 15 wt. % lithium salt was better than the sample 20Li, which is a PEO-based SPE containing 20 wt. % lithium salt. Due to environmental factors such as humidity and noise, the ionic conductivity of the sample 20Li may be lower. As is known, when LiTFSI salt is added to the polymer, it acts as a plasticizer. Thanks to the anions coming from the salt, it enables the polymer chains to move more freely and increases the amorphous structure and free volume of the polymer (Chaurasia et al., 2011; Toker et al., 2016). The increase in amorphous structure causes a decrease in crystallinity in polymer and this reduction in crystallinity contributes to the enhancement of the ionic conductivity of CPEs (Singh et al., 2017). It becomes easier to transform crystal structures into amorphous phases by rising the lithium salt concentration. The use of salt concentration in the literature is between 15 % and 20 %. The excessive use of lithium salt in polymer electrolytes may result in the formation

of viscous polymer electrolytes. This situation may decrease the ionic conductivity of PEO-based SPE owing to make the mobility of ions difficult (Mathew et al., 2019).

The ionic conductivity values of 2Mg-15Li and 5Mg-15Li samples, which are PEO-based NCPEs were found to be 5.04×10^{-6} and 5.86×10^{-6} S/cm, as shown in Figure 4.35, respectively. Although 2 and 5 wt. % nanosized MgBDC MOF filler were added to these PEO-based electrolytes containing 15 wt. % LiTFSI salt, the NCPEs could not sufficiently improve the ionic conductivity as indicated in Figure 4.35. Therefore, it can be said that the ionic conductivity values do not show a linear increase in the filler concentration for PEO-based SPEs containing 15 wt. % lithium salt. When 2 and 5 wt. % nanosized MgBDC MOF fillers were added to PEO-based electrolytes containing 20 wt. % LiTFSI salt, the ionic conductivity of them were increased outstandingly, and the ionic conductivity values of 2Mg-20Li and 5Mg-20Li samples were found to be 2.47×10^{-5} and 2.85×10^{-5} S cm^{-1} at ambient temperature, respectively as demonstrated in Figure 4.35. It was revealed that the increase of MgBDC MOF concentration in PEO-based SPE containing lithium salt at ambient temperature increases ionic conductivity and the positive effect of MgBDC MOF concentration on ionic conductivity. When the usage rate of filler rises, the dilution effect becomes dominant and this causes a decrease in ionic conductivity. Their low amount of use contributes to both fast ion transport and conductivity by interacting specifically with ceramic surfaces (Mathew et al., 2019; Suriyekumar et al., 2016; Angulakshmi et al., 2014). Therefore, the optimum MOF concentration was determined as 2% and 5% in this study. In some literature, the maximum filler usage concentration is given as 8-10% (Angulakshmi et al., 2014).

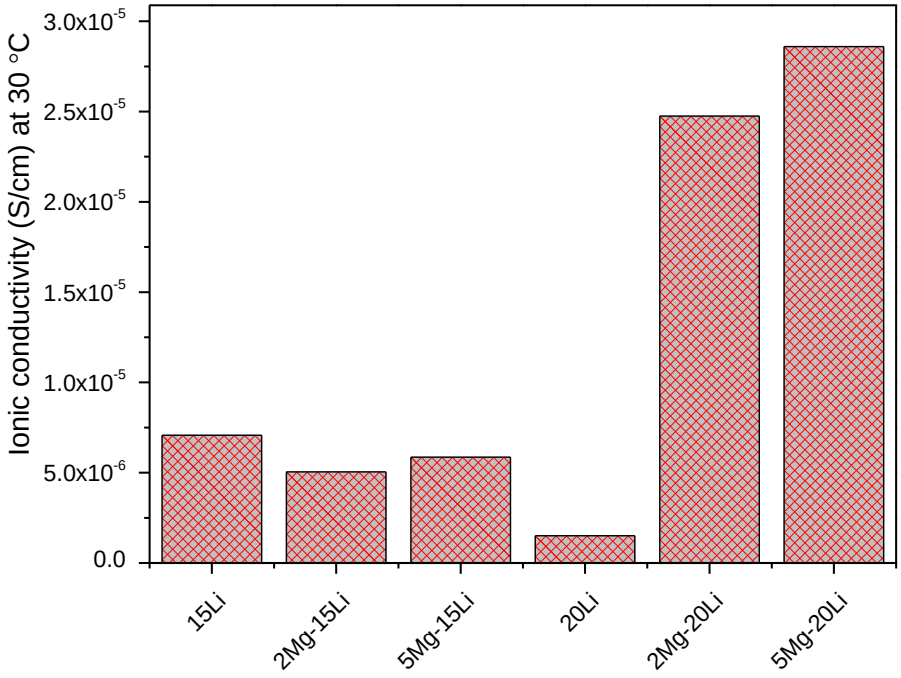

Figure 4.35. Effect of lithium salt and MgBDC MOF particle concentrations on ionic conductivities of PEO based SPEs and NCPEs at 30 °C temperature

There was an increase in the ionic conductivity in both15Li and 20Li samples. But, sample 15Li was a little bit higher than the sample at 40 ºC temperature as indicated in Figure 4.36. The ionic conductivity values of 15Li and 20Li samples were determined to be 1.48×10^{-5} and 1.11×10^{-5} S cm^{-1} at 40 ºC temperature, respectively. Ionic conductivity values of 15Li and 20Li samples came close to each other with the heat increase. The ionic conductivity values of 2Mg-15Li, 5Mg-15Li, 2Mg-20Li, and 5Mg-20Li samples were found to be 2.45×10^{-5}, 2.67×10^{-5}, 3.16×10^{-5} and 3.45×10^{-5} S cm^{-1} at 40 ºC temperature, respectively. Ionic conductivity of NCPEs enhanced with an increase in the amount of both Li salt and nano-sized MgBDC MOF with increasing heat.

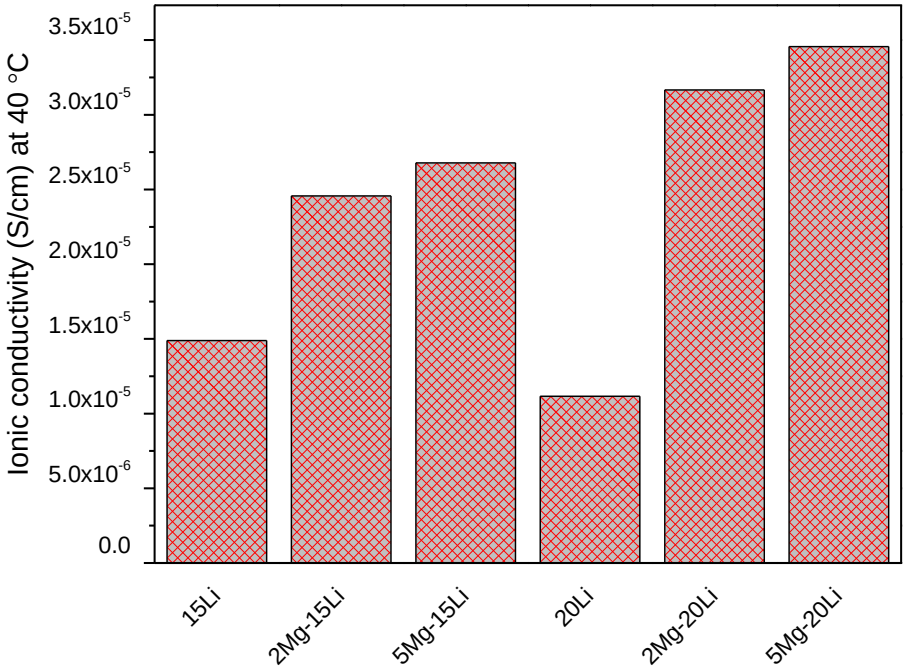

Figure 4.36. Effect of lithium salt and MgBDC MOF particle concentrations on ionic conductivities of PEO based SPEs and NCPEs at 40 °C temperature

Similarly, the ionic conductivity of 15Li and 20Li samples were also close to each other with an increase in temperature, as indicated in Figure 4.37 and ionic conductivity values of them were determined to be 2.62×10^{-5} and 2.16×10^{-5} S cm^{-1} at 50 ºC temperature, respectively. Ionic conductivity values of 2Mg-15Li, 5Mg-15Li, 2Mg-20Li, and 5Mg-20Li samples were determined to be 2.71×10^{-5}, 3.09×10^{-5}, 5.18×10^{-5} and 5.48×10^{-5} S cm^{-1}, respectively. As can be seen, it was identified that ionic conductivity went up continuously with an increase in amount LiTFSI salt and nanosized MgBDC MOF, and also with the rising temperature.

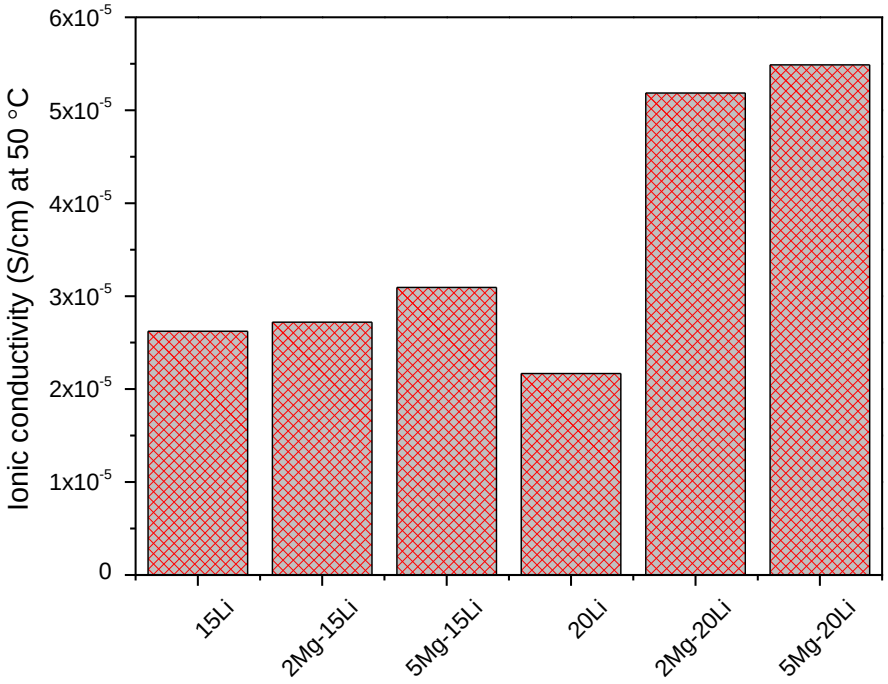

Figure 4.37. Effect of lithium salt and MgBDC MOF particle concentrations on ionic conductivities of PEO based SPEs and NCPEs at 50 °C temperature

The maximum ionic conductivity values for 15Li and 20Li samples were determined as 9.22×10^{-5} and 7.7×10^{-5} S cm^{-1}, at 60 ºC (high temp.), respectively. Besides, maximum ionic conductivity values for 2Mg-15Li, 5Mg-15Li, 2Mg-20Li, and 5Mg-20Li samples were found to be 9.81×10^{-5}, 1.82×10^{-4}, 2.08×10^{-4} and 3.26×10^{-4} S cm^{-1}, at high temperature, respectively. In PEO-based NCPEs, the highest ionic conductivity at 60 ºC was reached at amounts containing 5 wt. % MgBDC MOF and 20 wt. % LiTFSI salt. With increasing temperature, the viscosity of polymer electrolytes decreases at higher temperatures and the mobility of ions making is easier. Due to this increase in ionic mobility, a significant contribution is made to ionic conductivity and there is an important increase (Singh et al., 2017, Singh, V. K. and Singh, R. K, 2015). It can be said that this raise in conductivity is closely related to the reduction in viscosity at high temperatures, which causes an increase in ionic mobility. In other words, this improvement in the ionic conductivity is depending on increasing ionic mobility and concentration of carrier ions (Nagajothi et al., 2017; Jinisha et al., 2017). Of course, the interaction between the MgBDC MOF filler and the lithium salt

also caused the mobility of ions and thus a raise in ionic conductivity. Using filler may cause a rise in free volume, which can be directly associated by increasing in ionic conductivity (Stephan et al., 2009). Between Lewis acid groups of the supplementary MgBDC MOF structures and the lithium, cations occur a competition for complex formation with alkoxides of the PEO chains and TFSI anions of the Li salt. In the present case, owing to the specific mobilization of the polar surface groups of having a supplementary filler, there are structural changes on its surfaces. The Lewis acid-base interactivity is centered on electrolytic types, thereby reducing ionic pairing and providing Li salt to dissolve by forming a kind of "ion filling complex" (Suriyekumar et al., 2016; Angulakshmi et al., 2014). In addition to this, MgBDC MOF has been used as a filler material and there is a Lewis acid center of it. In this way, the chemical actions can occur with the anions of Li salt and cause a reduction in the crystallinity of the polymer host (Angulakshmi et al., 2014). Therefore, it can be said that the ionic conductivity value is related to the nature of the filler used. On the other hand, in a study, it was stated that the filler addition behaves like a solid plasticizer in the polymer matrix and therefore filler prevents the rearrangement of the PEO chain (Gerbaldi et al., 2014). In this way, the lithium salt is more easily dissociated and the mobility of Li ions is improved and thus contributes to the improvement of ionic conductivity. The thickness of polymer electrolytes can also be examined from Table 7.4 and equation (3.8) to affect the ionic conductivity. It has been observed that the ionic conductivity improves as the thickness decreases.

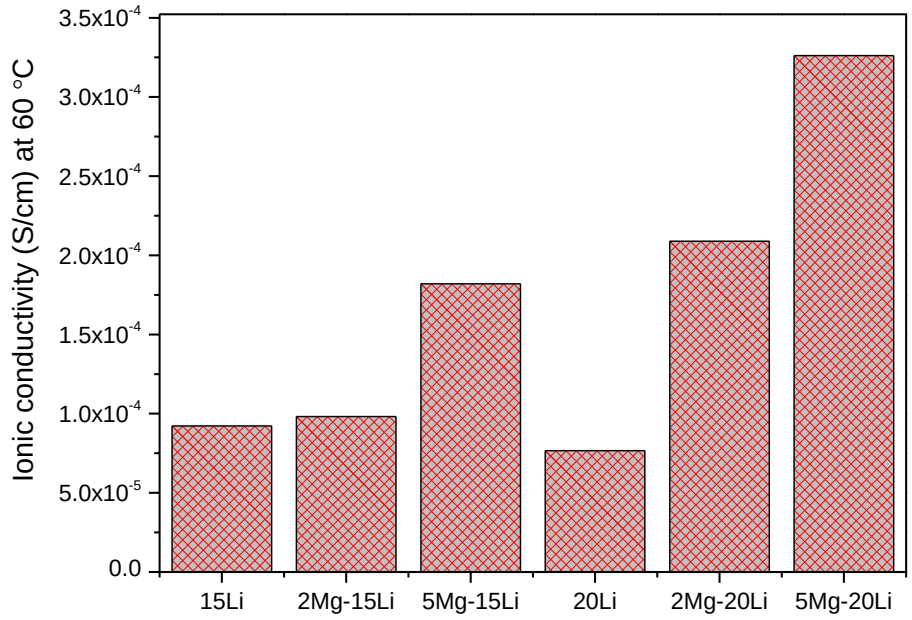

Figure 4.38. Effect of lithium salt and MgBDC MOF particle concentrations on ionic conductivities of PEO based SPEs and NCPEs at 60 °C temperature

As seen in Figure 4.34, it was determined that ionic conductivity(σ) of all samples went up linearly with increasing temperature and followed the Arrhenius type thermally activated process (Singh et all., 2017). The conductivity (σ)–temperature (T) plots show an Arrhenius type behavior throughout the temperature range. The linear diversity in log σ vs. 1000 T^{-1} plot can be expressed a thermally enabled procedure performed with this equation below (Jinisha et al., 2017),

$$\sigma = \sigma_0 \exp\left(\frac{-Ea}{kT}\right) \quad \textbf{(3.9)}$$

where σ_0, E_a, and k are referred to as pre-exponential coefficient, activation energy (J/mol), and Boltzmann constant, respectively.

Thermal activation energy [E_a] of all-polymer electrolytes has been computed from the slope of the Arrhenius plot (Figure 4.34) by using the 3.9 equation mentioned

earlier in the physical and chemical characterization section. As seen Table 4.7, the thermal energy [E_a] values for 15Li, 20Li, 2Mg-15Li, 5Mg-15Li, 2Mg-20Li and 5Mg-20Li samples were determined to be 0.239 eV, 0.291 eV, 0.209 eV, 0.201 eV, 0.182 eV and 0.162 eV, respectively. According to these results, the 5Mg-20Li sample with the highest ionic conductivity value of 2.85×10^{-5} S/cm at room temperature and 3.26×10^{-4} S/cm at high temperature had the lowest activation energy value of 0.162 eV. In the literature, the thermal activation energy [E_a] has corresponded to a combination of the energy of defect formation and transport (Mohamed et al., 2003; Latif et al., 2006). Thus, it can be said that the energy needed to makes easier the transport of ions by providing a conductive medium is through the thermal activation energy [E_a] (Latif et al., 2006; Jinisha et al., 2017). For the 5Mg-20Li sample, which is PEO-based NCPE consisting of MgBDC MOF, it can be said that the softening and melting of the crystal phase of PEO and the decrease in its crystallinity cause a decrease in the thermal activation energy and an increase in ionic conductivity. DSC results confirmed the 5Mg-20Li sample in terms of melting and crystallinity results. It was the sample that decreased the melting point (T_m) the most and the crystallinity value the most. The degree of crystallization (X_c%) reduced and the decrease in crystallinity was thought to help significantly to enhance the ionic conductivity of NCPEs. In addition, this decrease in activation energy [E_a] in NCPEs may be related to the increased ionic transport and the increase in the number of mobile charge carriers (Sing et al., 2017).

Table 4.7. The ionic conductivity values at different temperatures and thermal activation energy of PEO based SPEs and NCPEs

Sample code	Thickness (cm)	Ionic conductivity at 30 ºC (S/cm)	Ionic conductivity at 40 ºC (S/cm)	Ionic conductivity at 50 ºC (S/cm)	Ionic conductivity at 60 ºC (S/cm)	Thermal Activation energy [E_a] (eV)
15Li	0.013	7.07×10^{-6}	1.48×10^{-5}	2.62×10^{-5}	9.22×10^{-5}	0.239
20Li	0.015	1.5×10^{-6}	1.11×10^{-5}	2.16×10^{-5}	7.7×10^{-5}	0.291
2Mg-15Li	0.009	5.04×10^{-6}	2.45×10^{-5}	2.71×10^{-5}	9.81×10^{-5}	0.209
5Mg-15Li	0.008	5.86×10^{-6}	2.67×10^{-5}	3.09×10^{-5}	1.82×10^{-4}	0.201
2Mg-20Li	0.009	2.47×10^{-5}	3.16×10^{-5}	5.18×10^{-5}	2.08×10^{-4}	0.182
5Mg-20Li	0.008	2.85×10^{-5}	3.45×10^{-5}	5.48×10^{-5}	3.26×10^{-4}	0.162

It is known that ideal E_a values predicted for all suitable SPE membranes used in lithium-ion battery applications change from 0.1 eV to 0.2 eV (Jinisha et al., 2017). For this reason, all-polymer electrolytes have been successfully produced in this study and these are among the suitable thermal actuation energy values.

Angulakshmi et al. (2014) synthesized Mg–BTC MOFs *via* the electrochemical method and they penetrated MgBTC based MOF to polymer electrolytes based containing LiTFSI salt. 10 wt. It was used at concentrations of 10 % Mg–BTC MOF and 15% LiTFSI for PEO-based electrolyte production and ionic conductivity measurement were performed in the glove box. Ionic conductivity of MgBTC MOF-based polymer electrolyte changed from ~10^{-4} S cm^{-1} to ~10^{-3} S cm^{-1} between 20 and 70 °C. The thermal activation energy of its was computed as 0.6 keV.

Yuan et al., (2013) produced nanosized Zn–BDC-based MOF-5 *via* the solvothermal method, and MOF-5 was successfully incorporated into PEO–LiTFSI electrolyte. It was also shown that electrochemical properties of PEO–LiTFSI electrolyte consisting of Zn–BDC based MOF-5 enhanced in the lithium-ion battery. It was used at amounts of 10 % MOF-5 and 15% LiTFSI for polymer electrolyte production and the ionic conductivity measurement was carried on in the glove box. The highest ion conductivity of the MOF-5 based composite polymer electrolyte was reported to be 3.16×10^{-5} S cm^{-1} at 25 °C.

Ni-BTC-based MOF was synthesized by using the solvothermal method, and it was integrated with a polymer electrolyte consisting of LiTFSI. It was reported that the included Ni-BTC-based MOF made a tremendous contribution in improving mechanical, thermal, and ionic conductivity features of polymer electrolytes. It was used at amounts of 10 % $Ni_3(BTC)_2$ MOF and 15% LiTFSI for polymer electrolyte production and the ionic conductivity measurement was made in an argon-filled glove box that contained below 1 ppm oxygen and humidity. It was informed that the highest ionic conductivity of Ni-BTC MOF-based CPE membranes was changed from 1.4×10^{-4} to 4.5×10^{-3} S cm^{-1} at 30 and 70°C temperatures (Suriyakumar et al., 2016).

In another work, Mathew et al. (2019) were synthesized micro-sized Mg–BDC and Mg–BTC MOFs at room temperature using the dropwise method. After the synthesis, these micro-sized MOFs were mixture separately in a polymer solution as an admixture for various amounts of LiTFSI salt and polymer-based micro composite

films were prepared. The maximum ionic conductivity of CPE prepared in the amount of 10% MgBDC MOF and 10% LiTFSI was found to be 7.02×10^{-4} S cm^{-1} at high temperature (70°C).

Wang et al. (2017), used three different types of fillers (one active filler; $Li_{1.3}Al_{0.3}Ti_{1.7}(PO_4)_3$ and two passive admixtures; TiO_2 and fumed silica) and in the PEO polymer matrix to prepare PEO-based NCPEs and their effects on ionic conductivity were studied. The lithium-ion conductivity value of PEO/$LiClO_4$ with 10 wt % $Li_{1.3}Al_{0.3}Ti_{1.7}(PO_4)_3$ found 1.70×10^{-4} S cm^{-1} at ambient temperature, which is an active filler. PEO−$LiClO_4$−NCPE system containing active filler showed higher ionic conductivity than PEO−$LiClO_4$−NCPE system containing passive fillers and also there was a stronger increase in the transport of lithium cations.

In another study, PEO-based NCPE films were produced by adding 10 wt % nano chitosan as a filler to the PEO matrix containing ionic liquid. The ionic conductivity value of 10^{-2} S/cm is very high due to the ionic liquid and nanofiller. On the other hand, cycling voltammetry (CV) and linear sweep voltammetry (LSV) analyses showed that the prepared electrolytes had excellent electrochemical stability of 3.9 V (Karuppasamy et al., 2016).

In all of the studies mentioned above, 10 wt. % filler was used for composite polymer electrolyte production. When the concentration of filler is 10 wt. % and above used in the production of composite polymer film, the viscosity of polymer membrane rises. For this reason, the ionic conductivity value decreases in CPE (Matsushita et al., 2000). Also, due to the high concentration of filler material, an excessive charge may accumulate on the CPE surface. The lithium-ion motion is blocked because of the electrostatic attraction force and can therefore cause a reduction in ionic conductivity.

To summarize the results of ionic conductivity in this study, it can be said that it has a remarkable improvement in ionic conductivity of both PEO-based SPE and NCPE samples at high temperatures. It was reached from 10^{-6} to 10^{-4} S/cm by adding LiTFSI salt and MgBDC MOF nanoparticle at different concentrations to the PEO-based SPEs and NCPEs at room temperature and high temperature. An increasement in ionic conductivity by order of one magnitude was examined upon admixture of (15 and 20 wt. %) lithium salt in the PEO matrix with increasing temperature. After adding (2 and 5 wt. %) MgBDC MOF to PEO-LiTFSI based polymer electrolytes, a

remarkable enhancement in ionic conductivity by order of two magnitudes was determined with increasing temperature. 5Mg-20Li sample, that is, PEO-based NCPE containing 5 wt % MgBDC MOF and 20 wt % LiTFSI, the ionic conductivity of its was outstandingly increased at room and high temperature (30 and 60 ºC) compare to other samples. It can be said that the ionic conductivity may be affected by factors such as concentration of filler and lithium salt, temperature, thickness, and environmental factors. It was understood that the ionic conductivity of PEO-based electrolytes was affected by an increase in the amount of both nanosized MgBDC MOF, LiTFSI salt, and also the rising temperature. It has been clearly understood that when the temperature is increased to 80 ºC, the ionic conductivity could reach up to 10^{-3} S cm^{-1}. How the fillers affect ionic conductivity on the transport properties of Li^+ cations in polymer electrolytes has been studied. These can be explained as follows:

a- The fillers act as plasticizers and improve the structure of the amorphous phase in polymer, reducing polymer crystallinity and thus increasing the conductivity (Scrosati et al., 2000a; Chung et al., 2001)

b- They act as crosslinking centers to increase ionic conductivity with polymer fraction and lithium salt anions (LiX^-). When fillers are used with polymer fraction and lithium salt anions, they can act as crosslinking centers to increase ionic conductivity. Thus, it can form conductive channels on the filling surface that improve conductivity (Zhou and Fedkiw, 2004).

c- Fillers break down ion agglomeration when they come together with acidic surface groups and anions or basic surface groups and cations to form a complex. So, Li^+ or X^- ions can move freely. This status improves salt dissociation and leads to a rise in charge carrier numbers. Hence, it gives rise to enhance in conductivity (Marcinek et al., 2000).

d- Fillers rise ion movement by supplying extra areas for movement of Li^+ or X^- ions because of the Lewis acid-base interactivities with surface groups and Li salt. Thereby, they contribute to the enhancement of ionic conductivity (Jayathilaka et al., 2002).

e- Fillers can temporarily cross-link the polymer chain by Lewis acid-base interactivities, which can cause polymer materials to harden. On the other hand, it may have lower conductivity than composite electrolytes without

fillers since it may prevent the transport of lithium cations (Zhou and Fedkiw, 2004).

f- Inert fillers can reduce conductivity due to the volume dilution effect (Fan et al., 1998).

5. CONCLUSIONS AND SUGGESTIONS

In this work, nanosized MgBDC MOFs were successfully synthesized *via* anodic dissolution of Mg^{+2} ions into the reaction medium by using the EC method without metal salts. After nanosized MgBDC MOF structures were synthesized, the yield % calculation was made and then characterization processes of them. Molecular bonding, thermal strength, crystal phase, microstructure, surface topography, and surface area analyzes were performed on nanosized MgBDC MOF structures. After the characterization of these, their homogeneous distribution of nanosized MgBDC MOF structures incorporated into the PEO-LiTFSI matrix was performed in a controlled manner by using the solution casting method. ATR FT-IR, TGA, DSC, XRD, SEM/EDS, POM, and EIS measurements were made for NCPEs composed of nanosized MgBDC MOF structures. The potential field application of NCPEs based MgBDC MOF was determined in this work. To summarize the results obtained, it can be expressed as follows:

1) The high-efficiency nanosized structures were synthesized by using BDC organic ligand and magnesium ribbons *via* the EC method. The yield (%) calculation of nanosized MgBDC MOFs was found to be 81 %. In the research of previous studies, nanoscale MgBDC MOF synthesis has not been done by the EC method. For this reason, it can be said that the synthesis of the EC method yield is quite high.

2) Based on FT-IR results, the vibration modes of the carboxyl functional groups from BDC appeared in a certain number of waves depending on the frequency. Likewise, the existence of Mg–O groups was determined by the vibration modes. The reasonable results were obtained where the Mg^{2+} ion and the BDC components were coordinated with each other, the bonds absorbed each other and as desired.

3) The endothermic-exothermic reactions, thermal degradations, and weight losses were determined with the temperature increase in nanosized MgBDC MOF material based on TGA analysis results. The endothermic reactions occurred by taking heat energy at 190, 645, and 930 °C, and three

endothermic peaks were observed in these temperature regions, respectively. The water and OH groups were removed from this structure between 60-200 °C. The first thermal decomposition and the first weight loss of 13% occurred from 60 to 200 °C. These groups are attributed as a result of the chemical reactions of the solvents and precursors used in the structure. It is seen that MgBDC based MOF nanomaterials burned out at temperatures between 150 and 250°C. DMF molecules were completely removed from the structure when the temperature reached 235°C. Many exothermic reactions took place between 200 and 550 °C. Thermogram curves continued in a stable line up to 550 °C. After the temperature of 550 ° C, all volatile substances in the MOF structure were removed. Then second thermal decomposition observed broke down due to the endothermic peak occurred at 645 °C. As a result, the MOF structure decomposed and the second weight loss of 37.5% occurred between 590 and 660 °C with temperature increase. The BDC organic ligand, which was established as a strong coordination bridge with magnesium ions, was removed structure in the temperatures range of 590-660 °C. The thermogram curves also progressed in a stable line in temperature between 660 and 905 °C. The third thermal decomposition and the third weight loss of 18.7% took place in the temperature range of 905 and 932 °C. The weight loss occurred mostly between 590 and 660 °C temperatures. Consequently, it was confirmed by TGA analysis that nanosized MgBDC MOF materials had high stability.

4) According to the XRD results of nanosized MgBDC MOF structures, the sharp peaks that are observed at 2θ values of 9.6°, 14.5°, 29.7°, 34.2°, 38.8°, and 42.05° correspond to crystalline planes such as (220), (420), (201), (202), (101) and (200), respectively. XDR pattern of nanosized MgBDC MOF is in good agreement with previously simulated XRD peaks. Based on the crystallographic data, the highly crystalline structure and purity of nanosized MgBDC MOF were confirmed. The relative intensity of the second peak that is located at 2θ value of 14.5° (420) is the highest among all the peaks. The peak splitting at 2θ values of 9.5° and 14.5° was not observed, thereby saving the crystal structure of nanosized MgBDC MOF.

The other characteristic peaks of MgBDC MOF nanostructures were observed at 2θ values of 44.6°, 46.1°, 49.9°, and 58.7°. According to the quantitative analysis results of XRD data, it was determined that nanosized MgBDC MOF and brucite phase ($Mg(OH)_2$) contains the ratio of 96% and 4%, respectively. The brucite phase, that is, $Mg(OH)_2$ has the hexagonal structure crystal system and the characteristic reflection of its has appeared at 2θ values of 38,8° (101). XRD crystallographic data results and crystal structure of nanosized MgBDC MOF are compatible with the literature.

5) Based on SEM analysis findings, the morphological structure of the powdered MgBDC MOF nanoparticles has been found to have a spherical and smooth structure. The grain sizes of these structures change in the range of 10-25 nm. It was observed that the morphological structure of MgBDC MOF nanoparticles obtained from a drop of dilute methanol solution was in the form of plates and their grain sizes varied in the range of about 20 nm. When examined in previous publications, MgBDC based MOF structures were not prepared using the EC method and therefore these structures are very important in terms of obtaining very low nanoscales. It can be said that the smooth, pore-free, and nano-sized microstructures observed with SEM analysis are quite successful. The homogeneous, regular, and uniform structures of powdered MgBDC nanoparticles were determined by STEM technique. The chemical compounds of nanosized MgBDC MOF were studied via EDS regional, EDS mapping, and EDS spectrum analyses. Based on EDS regional and mapping analysis results, it was verified that nanosized Mg-based MOF nanoparticles are homogeneous distribution. The presence and high purity of Mg, C, and O atoms were confirmed by EDS mapping and EDS spectrum analyses of nanosized MgBDC MOF structures.

6) The surface roughness of nanosized MgBDC MOF structures was studied by AFM analysis. MgBDC MOF nanoparticles were very well dispersed on the substrate. Based on AFM tapping mode images, it was observed that MgBDC MOF nanoparticles had homogeneous structure, regular distribution, and spherical shape. It has also been found that their dimensions range from 30 to 50 nm. The uniform distribution of them on the surface can

be related to good nucleation sites for their controlled growth. The AFM results were consistent with the SEM results and the morphological features and grain structures supported each other.

7) Based on BET results, total surface area (S_{BET}), pore volume (V_{pore}), and average pore size radius of nanosized MgBDC MOF particles were found to be 23.132 $m^2\ g^{-1}$, 0.057 $cm^3\ g^{-1,}$ and ~50 nm, respectively. As regards these results, the surface area of these MgBDC MOF nanoparticles was found to be lower value compared to other previous studies. This situation is related to the structural properties of MOF materials, as well as being affected by starting materials, variety of solvent, concentrations, synthesis techniques. Because MOF materials were synthesized by the solvothermal method using DEF solution in one of the previous studies. On the other hand, higher surface areas were obtained by applying nitrogen under atmospheric pressure at 30 and 400 °C higher heat. In this study, MOF nanostructures were produced by EC method using DMF solvent, and BET analysis was applied at -196 °C under nitrogen atmospheric pressure.

8) ATR FT-IR spectrum results were examined the molecular bonds of pure PEO, pure LiTFSI, PEO–LiTFSI electrolytes, and PEO-based NCPEs containing nanosized MgBDC MOF in the region of 4000–400 cm^{-1}, respectively. The FT-IR results of them are described below, respectively:

» The characteristic vibration modes of pure PEO and pure LiTFSI at various wavenumbers are observed. The results of pure PEO are consistent with the literature and it was confirmed the existence of PEO crystallinity. It was verified in this study that the peaks from previous studies for pure LiTFSI salt have approximately the same wavenumbers.

» When lithium salt was combined with PEO material, the polymer-lithium salt complex (EO/Li^+) has been formed. Due to this complexation, the Li^+ cation and the five ether oxygens of PEO were affected by each other and the Li^+ cations moved towards the polymer matrix by hopping movement. The vibration modes from PEO and lithium salt were changed in terms of

intensity, shape, and position. The original peaks of pure PEO and pure LiTFSI have shifted, decreased, and broadened. The center of the band of PEO changed because of the sulfur-methylene ($S\text{-}CH_3$) bond from the imide anion ($TFSI^-$). Similarly, the absorption peaks of pure LiTFSI salt were expanded and shifted due to $C–SO_2–N$ bonds, and their intensities were decreased. The disappearances, increases, or decreases of peaks in the FT-IR spectrum is an expected situation. This situation could be explained that these bands bonded with organic compounds from PEO. The FT-IR vibrational spectra of the PEO-LiTFSI system have considerably spread and so, it can be indicated that the crystal structure of PEO decreases and turns into an amorphous structure by the addition of LiTFSI salt. Many shifts occurred in bands of PEO due to the strong Li^+ ion complexation with PEO. These shifts can be explained by the that the Li^+ ion acts in the polymer matrix by hopping mechanism. The decrease of peaks in the FT-IR spectrum is an expected situation. This situation can be explained that these bands bonded with organic compounds from TFSI anions. Also, there is related to the proportion of lithium salt added to PEO. Correspondingly, it can be said that as the content of salt increases, it absorbs more and bonds better. As a result, 20Li samples, which are PEO-based SPE containing 20 wt % lithium salt may be more an amorphous and proper material in the PEO-LiTFSI system.

» When nanosized MgBDC MOF material was incorporated with the PEO-LiTFSI system, the intensities, positions, and shapes of the $TFSI^-$, PEO and MgBDC MOF changed. The observed vibration modes in PEO-based NCPEs shifted, decreased, broadened, disappeared, and increased. This case can be explained that these bands bonded with $C–SO_2–N$ bonds from PEO and lithium salt. This means that the organic components are bounded to the structure or absorbed as desired. On the other hand, as a result of the adding of MgBDC MOF into the PEO-LiTFSI matrix may be occurred the constitution of complexation in the system. So, a polymer-magnesium complex (EO/Mg^{2+}) can be formed. The previously amorphized structures with the adding of lithium salt were slightly crystallized again due to the mixture of MgBDC MOF to PEO-LiTFSI matrix. This case is related to the

concentration of MgBDC MOF added to the PEO-LiTFSI matrix. Correspondingly, it can be said that as the amount of MgBDC MOF increases, the structure becomes more crystalline property. As the use of MgBDC MOF is effective in crystallizing the material, the amount of MgBDC MOF is important. Therefore, the amount of MgBDC MOF used in NCPEs production was determined as the optimum ratio of 2 and 5 wt. %. According to FT-IR analysis results, it can be said that PEO-based NCPE containing 5 wt. % MgBDC MOF and 20 wt. % LiTFSI salt used is more suitable for semi-crystalline material. As a result, it can be stated that the obtained structures turned to semi-crystalline polymer materials. In addition to this, it can be said that more absorption and bonding were observed in the structure due to the rise in the amount of both MgBDC MOF and Li salt. In other words, ATR FT-IR analysis was pioneered that the ionic conductivity values of the 5Mg-20Li sample could exhibit better performance.

9) According to the TGA analysis results, the endothermic-exothermic reactions, thermal degradations, and weight losses were observed with the temperature increase for pure PEO, PEO-based SPEs, and NCPEs. After adding LiTFSI salt into the PEO matrix, the irreversible thermal decompositions took place at about 368-399°C and 202-393 °C for PEO-based SPEs consisting of 15 wt. % and 20 wt. % LiTFSI salt, respectively. When the blending of nanosized MgBDC MOF filler to PEO-LiTFSI system, the thermal stability of PEO-based NCPEs improved and the thermal decompositions of them occurred at about 360-390 °C. The total average weight loss of them was found to be 78.5 % at temperatures between 390 and 560°C. It has been seen that the thermal stability of PEO-based NCPEs has reached above 360 °C. The $T_{d,\,95\%}$ values of PEO-based NCPEs were found to be shorter than PEO. Because of the solvent decomposition, it might also be possible for some contaminations to occur at extreme temperatures. Therefore, there may be a situation with the solvent used. The $T_{d,\,85\%}$ values of PEO-based NCPEs increased with the addition of 2 and 5 wt. % nanosized MgBDC MOF structures to PEO-LiTFSI system. The $T_{d,\,85\%}$ values of 2Mg-15Li, 5Mg-15Li, 2Mg-20Li were obtained at temperatures 389, 392, 390°C, respectively. However, $T_{d,\,85\%}$ values of 5Mg-20Li sample was found to be

about 363°C. The 5Mg-20Li sample started thermal decomposition earlier according to other samples. The $T_{d,\ max}$ values of 2Mg-20Li and 5Mg-20Li samples were found to be at 430 and 427 °C, respectively and these were the highest values. These values are extremely important for ionic conductivity measurements. It has given films a strong barrier effect in terms of thermal degradation by the addition of nanosized MBDC MOF to the PEO-LiTFSI system. The improved thermal stability of NCPEs has corresponded to the "shielding effect".

10) Based on DSC analysis, the results of pure PEO, PEO-LiTFSI, and PEO-based NCPEs containing MgBDC MOF samples were explained. The T_m, T_g, ΔH_m, and X_c % were computed from DSC curves. The T_m of pure PEO, 15Li, and 20Li samples was found at 66.5, 66.28, and 62.55 °C, respectively. The T_m values of 2Mg-15Li, 5Mg-15Li, 2Mg-20Li, 5Mg-20Li samples were obtained at temperatures 58.74, 59.13, 50.94, and 50.09 °C, respectively. As it was also understood from these values, the intensity of pure PEO melting peak continuously decreased as the amount of lithium salt and nanosized MgBDC MOF increased. So, the addition of LiTFSI salt and nanosized MgBDC MOF structures into the PEO substance strongly restricted crystallization and decreased the amount of crystalline phase in the PEO structure. In other words, the decrease in T_m value improves the amorphous property of the samples. On the other hand, after the incorporation of lithium salt and MgBDC MOF filler into the PEO matrix, the position and area of the PEO melting peak changed. The T_g values of pure PEO, 15Li and 20Li polymer electrolytes were observed at temperatures -53.58, -33.27 and -34.94°C, respectively ($T_{g15Li} > T_{g20Li} > T_{gPEO}$). It can be seen that T_g increases on the incorporation of lithium salt into polymer electrolyte film with a corresponding decrease in T_m value. An increase of about 20 and 18°C was determined for T_g values of 15Li and 20Li PEO-based polymer electrolyte samples. After adding nanosized MgBDC MOF filler into the PEO-LiTFSI system, T_g values of PEO-based NCPEs decreased slightly. The T_g values of 2Mg-15Li, 5Mg-15Li, 2Mg-20Li, 5Mg-20Li samples were found at temperatures -38.56, -35.32, -38.21 and -39.05 °C, respectively. According to these results, the Tg value order of magnitude is as follows:

$T_{g15Li} > T_{g20Li} > T_{g5Mg\text{-}15Li} > T_{g2Mg\text{-}20Li} > T_{g2Mg\text{-}15Li} > T_{g5Mg\text{-}20Li} > T_{gPEO}$.

It was determined that T_g values of NCPEs increased compared to pure PEO electrolytes. However, it was observed that their T_g values decreased slightly compared to the PEO-LiTFSI system. A decrease was observed at temperatures between approximately 2 and 5°C in T_g values of NCPEs due to the crystal structure of MgBDC MOF. The addition of nanosized MgBDC MOF filler into the PEO-LiTFSI system helped in increasing the free volume and local chain flexibility by lowering the T_g value. The decrease in the T_g value of NCPEs electrolyte film showed that it improved the flexibility of the polymer chain. Also, this change in T_g value can be corresponded to the amorphization due to the mixture of LiTFSI salt into PEO and the MOF filler interaction within the PEO matrix. To summarize, the T_g value decreased in MgBDC MOF-doped nanocomposite polymer electrolytes was the result of the interaction of oxygen in the ethylene oxide part with the Lewis acidic regions in the metal-organic frameworks. This EO/Mg^{2+} interaction between ethylene oxide and magnesium chains has improved the mobility of the amorphous part of PEO by nanosized MgBDC MOF fillers. Thus, the free volume and chain elasticity were increased by lowering T_g. In a sense, it can be said that there is a 2.5% free volume increase in polymer materials. The H_m and X_c values of pure PEO, PEO-based SPEs and NCPEs are compared. The T_m and X_c values of polymer electrolyte films dramatically decreased when 20 wt. % LiTFSI salt was combined with PEO. The LiTFSI salt has a strong electron-withdrawing group (SO_2CF_3) and the salt dissolution occurred because –SO_2–N–SO_2– the functional group from the $TFSI^-$ anion exhibited high elasticity. As in previous studies, it was estimated that the X_c % can decrease when lithium salt is incorporated into the PEO structure. The mixing of nanosized MgBDC MOF structures into the PEO-LiTFSI system decreased both the T_m and X_c of polymer electrolytes. The X_c % decreased as the amount of lithium salt and nanosized MgBDC MOF increased. The T_g values of the NCPEs were decreased by adding nanosized MgBDC MOF to the PEO-LiTFSI system. In addition to this, it was contributed to increasing free volume and chain flexibility. The mobility of polymer chains can be improved by increasing chain flexibility. A decrease in the T_g value can help the easy movement of the ions, and as a result, the ionic conductivity is

expected to increase. For this reason, the intermolecular force between LiTFSI salt, nanosized MgBDC MOF, and the C–O–C group of PEO caused the ionic conductivity of the polymer electrolyte films to increase. The ΔH_m and X_c values reduce systematically as a function of lithium salt and nanosized MgBDC MOF addition to PEO substance. Based on the data, the X_c % calculated for each sample indicated that after the addition of nanosized MgBDC MOF filler into the PEO-LiTFSI system there was a significant increase in the amorphous phase. The 2Mg-20Li and 5Mg-20Li samples reduce ΔH_m and X_c more than 2Mg-15Li and 5Mg-15Li samples. The decrease of X_c % value with the addition of nanosized MgBDC MOF and LiTFSI salt was explained by two possible reasons: the first one, it may be related to the EO/Li^+ by coordination of ether-oxygen from PEO with lithium ions. The second one may be due to the EO/Mg^{2+} interaction between the cations from magnesium ions and the ether-oxygen components from PEO. The nanosized MgBDC MOF and LiTFSI salt prevented crystalline growth, and it reduced the number of PEO chains that form the crystallization regions in PEO-LiTFSI-MgBDC MOF hybrids. Therefore, the X_c % reduction and the decrease in crystallinity were thought to help significantly to enhance the ionic conductivity of NCPEs.

11) Looking at XRD patterns of pure PEO, PEO-based SPEs and NCPEs were observed at 2θ values. When LiTFSI salt was added to the polymer material, it has been observed that the intensity of the peaks decreased significantly due to molecular interactions between the lithium salt and PEO. As a result of this interaction, polymer-lithium salt complexation occurred, and the helical structure of the polymer was disrupted to form free lithium ions in the system. In addition to this, polymer-lithium salt complexation led to small shifts in 2θ values of main PEO peaks. The anion-cation (EO/Mg^{2+}) interaction between MgBDC MOF and polymer can be like the (EO/Li^+) interaction between the lithium salt and polymer. Therefore, MgBDC MOF may have prevented the formation of the PEO crystal package. This case may be related to the reduction in PEO crystallinity due to the penetration of MgBDC MOF into the PEO-LiTFSI system. This behavior can lead to an increase in the ionic conductivity of PEO electrolytes by the distortion of

PEO chain reassembly. On the other hand, XRD results of NCPs were parallel to each other by DSC analysis, and the crystal structure of polymers was confirmed.

12) Microstructures of pure PEO, PEO-based SPEs, and NCPEs were investigated by SEM technique. When LiTFSI salt was combined with pure PEO, it was observed that the size of the spherulites was decreased. After adding LiTFSI salt into PEO, the aggregations occurred and formed a soft form, such as foam. This was explained as the "breathing mode" in literature. In addition to this, it was determined that the EO/Li^+ complexation forms a crystalline complex by coordinating the ether oxygen. On the surface of polymer electrolytes containing lithium salt were observed some small pores. This case has corresponded to nonhomogenous evaporation of solvent during the casting of the films. By the penetration of nanosized MgBDC MOF materials into the PEO-LiTFSI system, it was observed that the nanomaterials were homogeneously and well distributed. Also, they have obtained a smooth surface morphology and are embedded in the polymer. The spherical structure of MgBDC MOF nanoparticles was determined and it was observed that their sizes changed between 30–50 nm. The sizes of the MgBDC MOF-based polymer electrolytes were observed a little bit larger than the MgBDC MOF powder, however, they were less aggregated. This may be related to the solution casting conditions of the PEO electrolyte and possible physical interactions between PEO and surface functional groups of MgBDC MOF. In summary, pure PEO has semi-crystalline spherulites, the dispersion and foam-like appearance of the lithium salt in PEO, the spherical shape of MgBDC MOF, and its homogeneous distribution in PEO and the variation of its nanoscale dimensions have been confirmed by SEM and the literature.

* The chemical compounds of PEO-based NCPEs containing 5 wt. % MgBDC MOF nanoparticles and 15 wt% lithium salt was studied *via* EDS regional, mapping, and spectrum analyses. Based on these results, SEM images complied with EDS results of PEO-based NCPEs containing MgBDC MOF. As previously mentioned, EDS regional, mapping, and

spectrum analysis results of MgBDC MOF nanoparticles supported the high purity of MgBDC MOF nanoparticles in which Mg, carbon (C), and oxygen (O) are present. The sulfur (S) and fluorine (F) elements came from $TFSI^-$ anions and thus their presence in the polymer membrane was confirmed. Based on EDS regional and mapping analysis results, it was verified that MgBDC MOF nanoparticles are homogeneous distribution in the PEO-LiTFSI system. In the EDS spectrum, PEO-based NCPE gave a strong peak of Mg element, and the presence of atoms such as C, O, F, S, and Mg has been verified. In previous studies, using nanoparticle MOFs as filler in PEO-LiTFSI electrolytes enhanced the ionic conductivity, mechanical and electrochemical stability due to the ordered nanoporous and hybrid structure of the metal-organic framework. In this respect, it can be said that SEM/EDS analysis results can improve ionic conductivity.

13) The polarized optical microphotographs of pure PEO, PEO-based SPEs, and NCPEs at the beginning of crystallization and after crystallization were studied by the POM analysis technique. According to the POM analysis results, the nucleation and gradual growth of spherulites in polymer electrolyte systems are explained for all polymer electrolytes. As in previous studies, the first nucleation centers become visible in pure PEO. The fact that pure PEO has a homogeneous, crystalline spherulitic structure, regular spherical structure of pure PEO. Also, the isotropic spherical three-dimensional shape of its has been confirmed in this study. The lamellar crystalline nature of pure PEO along with dark boundaries has been indicated the amorphous content in the polymer. So, this study was consistent with previous studies. After the complexing PEO with LiTFSI salt, the first nucleation centers become visible like pure PEO. In the PEO-Li salt system, the dark boundaries expanded more and the spherical patterns changed significantly. The spherulitic structure of pure PEO became nonhomogeneous. This has been attributed to be related to the density of high nucleation centers. The imide salt itself performed as a nucleation substance in the PEO-LiTFSI salt system. In this case, the spherulitic occurred relatively early collision with each other, due to the high density of nucleation centers. Therefore, this process caused to limitation of the size of

the spherulites, and consequently three-dimensional grain-like structures resulted. After the collision of the spherulites, their growth also got slower. It has been stated that the imide salt aglomerated on the crystallization side can function as a plasticizer. For this reason, this situation case explains that the amorphous content in the PEO-LiTFSI system has significantly increased and hence it has decreased crystallinity in the material. After nanosized MgBDC MOF structures were incorporated into the PEO-LiTFSI system, first nucleation centers were not captured as in the pure PEO and PEO-LiTFSI system. As can be seen from optical microphotographs, there has been a change in light intensity. Because of the presence of 2 and 5 wt.% nanosized MgBDC MOF, the crystallization process was prevented, and thus the specific spherulite texture of pure PEO was completely broken down. In addition to this, the spherulite sizes with PEO-based NCPEs containing nanosized MgBDC MOF structures have changed a lot, and t it has been determined to be much smaller than the pure PEO and PEO-LiTFSI system. Also, the spherulites have turned into the anisotropic structure and non-spherical shapes. Also, the spherulites turned into the anisotropic structure and non-spherical shapes:

* This case may be related to the EO/Mg^{2+} interaction between the cations from magnesium ions and the ether-oxygen components from PEO material.
* It can be related to the EO/Li^{+} interaction that occurs between anions from lithium ions and ether-oxygen coordination in PEO material.

In the light of all these, it has been observed that the number of PEO chains forming the crystallization regions in PEO-based NCPEs has decreased. Based on POM image results, it can be said that the 5Mg-20 Li sample has a better distribution inside PEO-LiTFSI film than the other samples. This sample may be a more amorphous structure. The nanosized MgBDC MOF substance and lithium salt have prevented crystalline growth. The reduction in crystallinity of the polymer complexation has been confirmed as discussed earlier in DSC and XRD results. So, the decrease in crystallinity of its provide enhancement in the ionic conductivity of NCPE films.

14) The ionic conductivity (σ) of PEO-based SPE and NCPE was measured at various temperatures. The ionic conductivity (σ) of PEO-based SPE and NCPE samples increased linearly with the increase of temperature and followed the Arrhenius type thermally activated process. There was a remarkable improvement in ionic conductivity of both PEO-based SPE and NCPE samples at room and high temperatures. As seen in the results, the ionic conductivity was increased from 10^{-9} to 10^{-4} S/cm with a controlled temperature increasing from 30 to 60 ºC by adding different concentrations of lithium salt and nanosized MgBDC MOF to PEO-based electrolytes. An increase in ionic conductivity of one order magnitude was examined upon the addition of (15 and 20 wt. %) lithium salt in the PEO matrix with increasing temperature. After adding (2 and 5 wt. %) MgBDC MOF to PEO-LiTFSI based polymer electrolytes, a remarkable enhancement in ionic conductivity of two order magnitude was determined with increasing temperature. As is seen from these results, 5Mg-20Li sample exhibited the highest ionic conductivity value of 2.85×10^{-5} - 3.26×10^{-4} S/cm, and 20Li sample had the lowest ionic conductivity value of 1.5×10^{-6} - 7.7×10^{-5} S/cm at 30 and 60 ºC. When the 20Li sample was compared to other samples, the ionic conductivity of the 20Li sample found a lower value. The LiTFSI salt acted as a plasticizer inside the polymer, and therefore the anions from the lithium salt provided the polymer chains to move more freely and increased the amorphous structure and free volume of the polymer. The increase in amorphous structure caused a decrease in crystallinity in polymer and this decrease in crystallinity contributed to the enhancement of the ionic conductivity of CPEs. The structure of polymer electrolytes became easier to transform crystal structures into amorphous phases by increasing the salt concentration. But, the excessive use of lithium salt in polymer electrolytes may have caused the formation of viscous polymer electrolytes. This situation decreased the ionic conductivity of the PEO-based SPE containing 20 wt. % LiTFSI as it made the mobility of ions difficult. Although 2 wt. % and 5 wt. % nanosized MgBDC MOF as a filler was added to the PEO-LiTFSI system containing 15 wt. % LiTFSI, the effect of MgBDC MOF on ionic conductivity could not be observed at room temperature. But, it has been observed that the ionic conductivity increased with the increase in

temperature for NCPEs containing 15 % LiTFSI. When 2 and 5 wt. % nanosized MgBDC MOF fillers were added to PEO-based solid polymer electrolytes containing 20 wt. % LiTFSI salt, the ionic conductivity increased outstandingly at both room temperature and high temperature. It was revealed that the increase of MgBDC MOF concentration in PEO-based NCPEs increased the ionic conductivity. So, the increase of concentration of MgBDC MOF had a positive effect on ionic conductivity. However, when the excessive use of filler predominates the dilution effect and causes a decrease in ionic conductivity. So, the optimum MOF amount was determined as 2 wt. % to 5 wt. % in this study. Its use at low concentrations contributed to both fast ion transport and conductivity by interacting specifically with ceramic surfaces. Also, the viscosity of polymer electrolytes decreased because of high temperatures, and thereby, the mobility of ions became easier. Due to this increase in ionic mobility, a significant contribution was made to ionic conductivity. At the same time, this increase in ionic conductivity led to an increase in the concentration of carrier ions. There was a Lewis acid-base interaction between the MgBDC MOF filler and the lithium salt. This interaction also caused the mobility of ions and an increase in free volume. There was a decrease in the crystallinity of the polymer host due to the filler reacting with the anions of the lithium salt. This filler addition behaved like a solid plasticizer in the PEO matrix, and so the filler prevented the rearrangement of the PEO chain. In this way, the lithium salt was more easily dissociated and the mobility of Li ions was improved.

The ionic conductivity was affected by some parameters such as salt and filler concentration, temperature, thickness, and environmental factors. Sample 5Mg-20Li with the highest ionic conductivity at ambient and high temperature had the lowest activation energy value of 0.162 eV. The energy required to make easier the transport of ions by providing a conductive ambient was supplied from the thermal activation energy [Ea]. In sample 5Mg-20Li, the treatments such as the softening, melting reduction in its crystallinity of PEO crystal structure caused a decrease in the thermal activation energy and an increase in ionic conductivity. DSC analysis results

confirmed the 5Mg-20Li sample in terms of melting and crystallinity results. It was the sample that decreased the melting point and crystallization degree (X_c %) the most. The reduction in crystallinity helped importantly to enhance the ionic conductivity of NCPEs. It has also been confirmed by XRD and POM analysis results in terms of crystal phase structure. In addition, this decrease in activation energy [Ea] in NCPEs was directly linked to the increased ionic transport and the rise in the mobile charge carrier numbers.

The estimated ideal thermal activation energy values for all proper SPE membranes used in lithium-ion battery application fields change between 0.1 eV and 0.2 eV. Thermal activation energy values of PEO-based SPEs and NCPEs produced in this study are between the optimum values. Therefore, both PEO-based NCPEs and SPEs have been successfully produced and these are among the ideal ionic conductivity and thermal activation energy values for favorable electrolyte materials used in Li-ion battery application areas. In this respect, PEO-based NCPEs can be used in lithium-ion battery application areas. Moreover, these electrolytes can take their place as a new candidate among nanocomposite polymer electrolytes in terms of containing nanoscale MOF in the production of all-solid-state Li-polymer electrolyte batteries purposed for use at high temperature.

Suggestions for research to be done after the study

In the first step of this thesis, nanosized MgBDC MOF structures were successfully synthesized *via* the EC method without metal salts. XRD, FT-IR, SEM / EDS, STEM, AFM, TGA, and BET analyzes were performed on nanosized MgBDC MOF particles. In the second step, PEO-based SPE films and PEO-based NCPEs containing nanosized MgBDC MOF films were produced by using the solution casting method. ATR FT-IR, TGA, DC, SEM / EDS, POM, and EIS analyzes of these films have been successfully performed. The suggestions for research to be made after the study are summarized below:

- In this thesis study, nanosized MgBDC MOF structures were synthesized by the electrochemical method. These structures can be synthesized by

combining BDC with BTC organic ligands, thus comparing the effect of the organic ligand on ionic conductivity.

- In this study, solid PEO-based nanocomposite polymer electrolytes containing nanosized MgBDC MOF were produced. The cyclic voltammetry (CV) studies can be performed to learn the electrochemical stability window or operating voltage limit of nanocomposite polymer electrolytes by sandwiching nanocomposite polymer electrolytes between two stainless steel electrodes (SS/NCPE/SS).
- The nanocomposite polymer electrolytes can be placed between the lithium-coated stainless steel electrode and the other stainless steel electrode and formed into a sandwich coin cell (Li/NCPE/SS). Then, LSV measurement can be performed to determine the electrochemical equilibrium and highest voltage value.
- The nanocomposite polymer electrolyte is placed between two lithium-coated stainless steel electrodes, and a coin cell can be made into sandwiches (Li/NCPE/Li). Chronoamperometry analysis can be performed to obtain information about the identity of this cell, determine the Coulombic efficiency and rate capacity by calculating the lithium-ion transfer number (Li_t^+).
- Galvonastic charge/discharge and cyclic voltammetry (CV) analyses can be performed to investigate the electrochemical performance of NCPEs in solid-state Li/$FePO_4$/NCPE coin cells and to examine their compatibility in Li-ion batteries.
- In addition, solid-state Li/$FePO_4$/NCPE coin cells can be compared with the commercial 2032 lithium button cells in terms of electrochemical performance.
- Solid PEO-based nanocomposite polymer electrolytes produced in this thesis can be utilized as solid electrolyte material in rechargeable (secondary battery) Li-ion cells.
- Testing can be done on portable electronic devices such as automobile keys.
- Solid PEO-based nanocomposite polymer electrolytes produced in this study can be applied as a solid electrolyte membrane in supercapacitors for energy storage.

REFERENCES

Abraham, K. M., Jiang, Z. and Carroll, B. 1997. Highly Conductive PEO-like Polymer Electrolytes, *Chemistry of Materials*, 9:9, 1978–1988.

Addy, S. A. 2008. Electrochemical arsenic remediation for rural Bangladesh (No. LBNL-1405E). *Lawrence Berkeley National Lab.(LBNL)*, Berkeley, CA, United States.

Angulakshmi, N., Kumar, R. S., Kulandainathan, M. A. and Stephan, A. M. 2014. Composite polymer electrolytes encompassing metal organic frame works: a new strategy for all-solid-state lithium batteries. *The Journal of Physical Chemistry C*, 118:42, 24240-24247

Ansari, A., Ali, A. and Asif, M. 2018. Microwave-assisted MgO NP catalyzed one-pot multicomponent synthesis of polysubstituted steroidal pyridines. *New Journal of Chemistry*, 42:1, 184-197.

Appetecchi, G. B., Croce, F., Persi, L., Ronci, F. and Scrosati, B. 2000. Transport and interfacial properties of composite polymer electrolytes. *Electrochimica Acta*, 45:8-9, 1481-1490.

AricQ, A. S., Bruce, P., Scrosati, B., Tarascon, J. M. and Schalkwijc, W. V. 2005. Nanostructured materials for advanced energy conversion and storage devices, *Nature Materials*, 4, 366-377.

Armand, M. B., Bruce, P. G. Forsyth, M., Scrosat, B. and Wieczorek, W. 2011. *Energy Materials*, Edited by Duncan W. Bruce, Dermot O'Hare and Richard I. Walton, John Wiley & Sons, Ltd., 22-26, UK.

Aurbach, D., Ein-Eli, Y., Markovsky, B., Zaban, A., Luski, S., Carmeli, Y. and Yamin, H. 1995. The study of electrolyte solutions based on ethylene and diethyl carbonates for rechargeable Li batteries: II. graphite electrodes. *Journal of The Electrochemical Society*, 142:9, 2882.

Ausili, A., Sánchez, M. and Gómez-Fernández, J. C. 2015. Attenuated total reflectance infrared spectroscopy: A powerful method for the simultaneous study of structure and spatial orientation of lipids and membrane proteins. *Biomedical Spectroscopy and Imaging*, 4:2, 159-170.

Bakker, A., Lindgren, J. and Hermansson, K. 1996. Polymer electrolytes based on triblock-copoly (oxyethylene/oxypropylene/oxyethylene) systems. *Polymer*, 37:10, 1871-1878.

Balo, L., Gupta, H., Singh, V. K. and Singh, R. K. 2017. Flexible gel polymer electrolyte based on ionic liquid EMIMTFSI for rechargeable battery application. *Electrochimica Acta*, 230, 123-131.

Batten, S. R., Champness, N. R., Chen, X. M., Garcia-Martinez, J., Kitagawa, S., Öhrström, L., O'Keeffe, M., Suh, M. P. and Reedijk, J. 2012. Coordination polymers, metal-organic frameworks and the need for terminology guidelines. *CrystEngComm*, 14, 3001-3004.

Bhattacharyya, A. J. and Maier, J. 2004. Second phase effects on the conductivity of non-aqueous salt solutions:"soggy sand electrolytes". *Advanced Materials*, 16:9-10, 811-814.

Bian, Y., Xiong, N. and Zhu, G. 2018. Technology for the remediation of water pollution: A review on the fabrication of metal organic frameworks. *Processes*, 6:8, 122.

Biswas, A., Kim, M. B., Kim, S. Y., Yoon, T. U., Kim, S. I. and Bae, Y. S. 2016. A novel 3-D microporous magnesium-based metal–organic framework with open metal sites. *Royal Society Chemistry Advances*, 6:85, 81485-81490.

Borgel, V., Markevich, E., Aurbach, D., Semrau, G. and Schmidt, M. 2009. On the application of ionic liquids for rechargeable Li batteries: high voltage systems. *Journal of Power Sources*, 189:1, 331-336.

Borodin, O. and Smith, G. D. 2006. Mechanism of ion transport in amorphous poly (ethylene oxide)/LiTFSI from molecular dynamics simulations. *Macromolecules*, 39:4, 1620-1629.

Bruce, P. G. (Editor). 1995. *Solid State Electrochemistry*, Cambridge University Press, 344, Cambridge, UK.

Bruce, P. G., Scrosati, B. and Tarascon, J. M. 2008. Nanomaterials for rechargeable lithium batteries, *Angewandte Chemie International Edition*, 47, 2930–2946.

Burgaz, E. 2011. Poly (ethylene-oxide)/clay/silica nanocomposites: morphology and thermomechanical properties. *Polymer*, 52:22, 5118-5126.

Burgaz, E., Erciyes, A., Andac, M. and Andac, O. 2019. Synthesis and characterization of nano-sized metal organic framework-5 (MOF-5) by using consecutive combination of ultrasound and microwave irradiation methods. *Inorganica Chimica Acta*, 485, 118-124.

Burgaz, E., Yazici, M., Kapusuz, M., Alisir, S. H. and Ozcan, H. 2014. Prediction of thermal stability, crystallinity and thermomechanical properties of poly(ethylene oxide)/clay nanocomposites with artificial neural networks, *Thermochimica Acta*, 575, 159–166.

Chae, H. K., Siberio-Perez, D. Y., Kim, J., Go, Y., Eddaoudi, M., Matzger, A. J., O'Keeffe, M. and Yaghi, O.M. 2004. A route to high surface area, porosity and inclusion of large molecules in crystals. *Nature*, 427:6974, 523-527.

Chakraborty, A. and Acharya, H. 2018. Facile synthesis of MgAl-layered double hydroxide supported metal organic framework nanocomposite for adsorptive removal of methyl orange dye. *Colloid and Interface Science Communications*, 24, 35-39.

Chaurasia, S. K., Singh, R. K. and Chandra, S. 2011. Structural and transport studies on polymeric membranes of PEO containing ionic liquid, EMIM-TY: evidence of complexation. *Solid State Ionics*, 183:1, 32-39.

Chen, B., Wang, X., Zhang, Q., Xi, X., Cai, J., Qi, H., Shi, S., Wang, J., Yuan D. and Fang, M. 2010. Synthesis and characterization of the interpenetrated MOF-5. *Journal of Materials Chemistry*, 20:18, 3758-3767.

Chen, C., Kim, J., Yang, D. A. and Ahn, W. S. 2011. Carbon dioxide adsorption over zeolite-like metal organic frameworks (ZMOFs) having a sod topology: Structure and ion-exchange effect. *Chemical Engineering Journal*, 168:3, 1134-1139.

Cheng, C. Y., Fu, S. J., Yang, C. J., Chen, W. H., Lin, K. J., Lee, G. H. and Wang, Y. 2003. NCHU-3: A crystalline inorganic–organic hybrid molecular sieve with extra-large cages. *Angewandte Chemie International Edition*, 42:17, 1937-1940.

Choi, J. S., Son, W. J., Kim, J. and Ahn, W. S. 2008. Metal–organic framework MOF-5 prepared by microwave heating: factors to be considered. *Microporous and Mesoporous Materials*, 116:1-3, 727-731.

Christie, A. M., Lilley, S. J., Staunton, E., Andreev, Y. G. and Bruce, P. G. 2005. Increasing the conductivity of crystalline polymer electrolytes. *Nature*, 433:7021, 50-53.

Chung, S. H., Wang, Y., Persi, L., Croce, F., Greenbaum, S. G., Scrosati, B. and Plichta, E. 2001. Enhancement of ion transport in polymer electrolytes by addition ofnanoscale inorganic oxides, *Journal of Power Sources*, 97-98, 644-648.

Coleman, J. N., Khan, U., Blaua, W. J. and Gun'ko, Y. K. 2006. Small but strong: A review of the mechanical properties of carbon nanotube–polymer composites, *Carbon*, 44, 1624-1652.

Croce, F. and Scrosati, B. 2003. Advanced membrane technology. *Annals of the New York Academy of Sciences*, 984, 194.

Croce, F., Curini, R., Martinelli, A., Persi, L., Ronci, F., Scrosati, B. and Caminiti, R. 1999. Physical and chemical properties of nanocomposite polymer electrolytes. *The Journal of Physical Chemistry B*, 103:48, 10632-10638.

Croce, F., Sacchetti, S. and Scrosati, B. 2006b. Advanced, lithium batteries based on high-performance composite polymer electrolytes. *Journal of Power Sources*, 162:1, 685-689.

Croce, F., Settimi, L. and Scrosati, B. 2006a. Superacid ZrO2-added, composite polymer electrolytes with improved transport properties. *Electrochemistry communications*, 8:2, 364-368.

Damhus, T., Hartshorn, R. M. and Hutton, A. T. 2005. Nomenclature of inorganic chemistry: IUPAC recommendations 2005. *Chemistry International*, 27:6. https://doi.org/10.1515/ci.2005.27.6.25

Davies, R. P., Less, R. J., Lickiss, P. D. and White, A. J. 2007. Framework materials assembled from magnesium carboxylate building units. *Dalton Transactions*, 24, 2528-2535.

Deepa, M., Agnihotry, S. A., Gupta, D. and Chandra, R. 2004. Ion-pairing effects and ion–solvent–polymer interactions in $LiN(CF_3SO_2)_2$–PC–PMMA electrolytes: a FTIR study. *Electrochimica Acta*, 49:3, 373-383.

Deepa, M., Sharma, N., Agnihotry, S. A. and Chandra, R. 2002. FTIR investigations on ion–ion interactions in liquid and gel polymeric electrolytes: $LiCF_3SO_3$-PC-PMMA. *Journal of Materials Science*, 37:9, 1759-1765.

Dhaouadi, H., Chaabane, H. and Touati, F. 2011. $Mg(OH)_2$ nanorods synthesized by a facile hydrothermal method in the presence of CTAB. *Nano-Micro Letters*, 3:3, 153-159.

Dhawa, T., Chattopadhyay, S., De, G. and Mahanty, S. 2017. In situ Mg/MgO-embedded mesoporous carbon derived from magnesium 1,4-benzenedicarboxylate metal organic framework as sustainable Li–S battery cathode support. *ACS Omega*, 2:10, 6481-6491.

Dudley, J. T., Wilkinson, D. P., Thomas, G., LeVae, R., Woo, S., Blom, H., Horvath J., Juzkow M. W., Denis B., Juric P., Aghakian, P and Dahn, J. R. 1991. Conductivity of electrolytes for rechargeable lithium batteries. *Journal of power sources*, 35:1, 59-82.

Eddaoudi, M., Kim, J., Rosi, N., Vodak, D., Wachter, J., O'Keeffe, M. and Yaghi, O. M. 2002. Systematic design of pore size and functionality in isoreticular MOFs and their application in methane storage. *Science*, 295:5554, 469-472.

Evans, J., Vincent, C. A. and Bruce, P. G. 1987. Electrochemical measurement of transference numbers in polymer electrolytes. *Polymer*, 28:13, 2324-2328.

Fan, J., Raghavan, S. R., Yu, X. Y., Khan, S. A., Fedkiw, P. S., Hou, J. and Baker, G. L. 1998. Composite polymer electrolytes using surface-modified fumed silicas: conductivity and rheology. *Solid State Ionics*, 111:1-2, 117-123.

Férey, G., Mellot-Draznieks, C., Serre, C., Millange, F., Dutour, J., Surblé, S. and Margiolaki, I. 2005. A chromium terephthalate-based solid with unusually large pore volumes and surface area. *Science*, 309:5743, 2040-2042.

Fry, A.J. 1989. *Synthetic Organic Electrochemistry*, 2nd Edition; John Wiley, 326-327, London, UK.

Fu, X., Yu, D., Zhou, J., Li, S., Gao, X., Han, Y., Fen, X. and Wang, B. 2016. Inorganic and organic hybrid solid electrolytes for lithium-ion batteries. *CrystEngComm*, 18, 4236-4258.

Furukawa, H., Ko, N., Go, Y. B., Aratani, N., Choi, S. B., Choi, E., Yazaydin, A. Ö., Snurr, R. Q., O'Keeffe, M., Kim, J. and Yaghi, O. M. 2010. Ultrahigh porosity in metal-organic frameworks. *Science*, 329:5990, 424-428.

Gadjourova, Z., Andreev, Y. G., Tunstall, D. P. and Bruce, P. G. 2001. Ionic conductivity in crystalline polymer electrolytes. *Nature*, 412:6846, 520-523.

Gascon, J., Aktay, U., Hernandez-Alonso, M. D., van Klink, G. P. and Kapteijn, F. 2009. Amino-based metal-organic frameworks as stable, highly active basic catalysts. *Journal of Catalysis*, 261:1, 75-87.

Gawas, U. B., Mandrekar, V. K. and Majik, M. S. 2019. Structural analysis of proteins using X-ray diffraction technique. *In Advances in Biological Science Research*. Academic Press, 69-84, London, UK.

Gerbaldi, C., Nair, J. R., Kulandainathan, M. A., Kumar, R. S, Ferrara, C., Mustarelli, P. and Stephan, A. M. 2014. Innovative high performing metal organic framework (MOF)-laden nanocomposite polymer electrolytes for all-solid-state lithium batteries. *Journal of Materials Chemistry A*, 2, 9948-9954.

Gnanaraj, J. S., Levi, M. D., Levi, E., Salitra, G., Aurbach, D., Fischer, J. E. and Claye, A. 2001. Comparison between the electrochemical behavior of disordered carbons and graphite electrodes in connection with their structure. *Journal of the Electrochemical Society*, 148:6, A525.

Goodenough, J. B. and Kim, Y. 2010. Challenges for rechargeable Li batteries. *Chemistry of Materials*, 22, 587-603.

Graebe, H., Netz, A., Baesch, S., Haerdtner, V. and Kwade, A. 2017. A Solvent-Free Electrode Coating Technique for All Solid State Lithium Ion Batteries. *ECS Transactions*, 77:11, 393-401.

Gray, F. M. 1997. *Polymer electrolytes*, The Royal Society of Chemistry, 175, Cambridge, UK.

Grey, F. and Armand, M. 1999. *In handbook of battery materials* (Editor:J. O. Besenhard), Wiley-VCH, 499, Weinheim, Germany.

Gschwander, S., Haussmann, T., Hagelstein, G., Barreneche, C., Ferrer, G., Cabeza, L., Gonzalo Diarce, Wolfgang Hohenauer, Daniel Lager, Alenka Ristic, Christoph Rathgeber, Harald Mehling, Conchita Peñalosa and Hennemann, P. 2015, Standardization of PCM characterization via DSC. In Proceedings of SHC 2015 International Conference on Solar Heating and Cooling for Buildings and Industry, December 2-4, Full paper, 2-4, İstanbul, Turkey.

Gupta, H., Balo, L., Singh, V. K., Chaurasia, S. K. and Singh, R. K. 2016. Effect of phosphonium based ionic liquid on structural, electrochemical and thermal behaviour of polymer poly (ethylene oxide) containing salt lithium bis (trifluoromethylsulfonyl) imide. *Royal Society Chemistry Advances*, 6:91, 87878-87887.

Guyomard, D. and Tarascon, J. M. 1995. High voltage stable liquid electrolytes for Li1+ xMn2O4/carbon rocking-chair lithium batteries. *Journal of Power Sources*, 54:1, 92-98.

Hema, M., Selvasekerapandian, S., Hirankumar, G., Sakunthala, A., Arunkumar, D. and Nithya, H. 2009. Structural and thermal studies of PVA: NH4I. *Journal of Physics and Chemistry of Solids*, 70:7, 1098-1103.

Hofmann, A., Schulz, M. and Hanemann, T. 2013. Effect of conducting salts in ionic liquid based electrolytes: viscosity, conductivity, and Li-ion cell studies. *Int. J. Electrochem. Sci*, 8, 10170-10189.

Horike, S., Umeyama, D. and Kitagawa, S. 2013. Ion conductivity and transport by porous coordination polymers and metal–organic frameworks. *Accounts of Chemical Research*, 46:11, 2376-2384.

Huang, L. W., Yang, C. J. and Lin, K. J. 2002. Toward the design and synthesis of lithium-ion intercalation into a coordination π–π framework host. *Chemistry–A European Journal*, 8:2, 396-400.

Huang, Z .L., Wang, L. P., Mou, C. X. and Li, J. Z. 2014. Magnesium terephthalate as an organic anode material for Sodium ion batteries. *Acta Physico-Chimica Sinica*, 30:10, 1787-1793.

Hulvey, Z., Sava, D. A., Eckert, J. and Cheetham, A. K. 2011. Hydrogen storage in a highly interpenetrated and partially fluorinated metal− organic framework. *Inorganic chemistry*, 50:2, 403-405.

Isakov, D., Martins, A. M., de Matos Gomes, E., Bdikin, I., Guimaraes, A., Dekola, T., Almedia, B., Neves, N.M., Reis, R.L. and Macedo, F. 2009. Synthesis of polymer-based triglycine sulfate nanofibres by electrospinning. *Journal of Physics D: Applied Physics*, 42:20, 205403.

Janiak, C. and Vieth, J. K. 2010. MOFs, MILs and more: concepts, properties and applications for porous coordination networks (PCNs). *New Journal of Chemistry*, 34:11, 2366-2388.

Jayathilaka, P. A. R. D., Dissanayake, M. A. K. L., Albinsson, I. and Mellander, B. E. 2002. Effect of nano-porous Al2O3 on thermal, dielectric and transport properties of the $(PEO)_9$LiTFSI polymer electrolyte system. *Electrochimica Acta*, 47:20, 3257-3268.

Jiang, Y. X., Xu, J. M., Zhuang, Q. C., Jin, L. Y. and Sun, S. G. 2008. A novel PEO-based composite solid-state polymer electrolyte with methyl group-functionalized SBA-15 filler for rechargeable lithium batteries, *Journal of Solid State Electrochemistry*, 12, 353-361.

Jinisha, B., Anilkumar, K. M. Manoj, M., Pradeep, V. S. and Jayalekshmi, S. 2017. Development of a novel type of solid polymer electrolyte for solid state lithium battery applications based on lithium enriched poly (ethyleneoxide) (PEO)/poly (vinyl pyrrolidone) (PVP) blend polymer, *Electrochimica Acta*, 235, 210-222.

Kaduk, J. A. 2002. Terephthalate salts of dipositive cations. *Acta Crystallographica Section B: Structural Science*, 58:5, 815-822.

Karan, S., Banerjee, D., Datta, A., Goswami, A. and Majumder, D. D. 2015. Shape based characterization of nanoparticles–a fuzzy mathematical approach. *In Proc Indian Natn Sci Acad*., 81:5, 1183-1192.

Karuppasamy, K., Rhee, H. W., Reddy, P. A., Gupta, D., Mitu, L., Polu, A. R. and Shajan, X. S. 2016. Ionic liquid incorporated nanocomposite polymer electrolytes for rechargeable lithium ion battery: A way to achieve improved electrochemical and interfacial properties. *Journal of Industrial and Engineering Chemistry*, 40, 168-176.

Kataoka, K., Nagata, H. and Akimoto, J. 2018. Lithium-ion conducting oxide single crystal as solid electrolyte for advanced lithium battery application, *Scientific reports*, 8, 1-9.

Kato, Y., Hori, S., Saito, T., Suzuki, K., Hirayama, M., Mitsui, A., Yonemura, M., Ib, H. and Kanno, R. 2016. High-power all-solid-state batteries using sulfide superionic conductors, *Nature Energy*, 1, 1-7.

Khan, N. A. and Jhung, S. H. 2015. Synthesis of metal-organic frameworks (MOFs) with microwave or ultrasound: rapid reaction, phase-selectivity, and size reduction. *Coordination Chemistry Reviews*, 285, 11-23.

Khuyen, N. Q., Zondaka, Z., Harjo, M., Torop, J., Tamm, T. and Kiefer, R. 2019. Comparative analysis of fluorinated anions for polypyrrole linear actuator electrolytes. *Polymers*, 11:5, 849.

Kitagawa, Kitaura, S. R. and Noro, S. I. 2004. Functional porous coordination polymers. *Angewandte Chemie International Edition*, 43, 2334-2375.

Kumar, K. K., Ravi, M., Pavani, Y., Bhavani, S., Sharma, A. K. and Rao, V. N. 2014. Investigations on PEO/PVP/NaBr complexed polymer blend electrolytes for electrochemical cell applications. *Journal of Membrane Science*, 454, 200-211.

Kumar, K. N., Sivaiah, K. and Buddhudu, S. 2014. Structural, thermal and optical properties of Tb^{3+}, Eu^{3+} and co-doped (Tb^{3++} Eu^{3+}): PEO+ PVP polymer films. *Journal of Luminescence*, 147, 316-323.

Kumar, P.N., Sasikala, U., Sekhar, P.C. and Sharma, A.K. 2013. Enhancement of electrical conductivity and ion transport in plasticized polymer blend electrolytes (PEO/PEMA) by addition of nanoscale inorganic oxides, *Asian Journal of Chemistry*, 25, 111-113.

Kumar, R. S. 2014. Studies on the Electrochemical Synthesis of Metal Organic Frameworks and Its Multifarious Applications. Doctorate Thesis, Bharathidasan University Electrochemical Process Engineering Central Electrochemical Research Institute, 149, India.

Kumar, Y., Hashmi, S. A. and Pandey, G .P. (2011). Lithium ion transport and ion–polymer interaction in PEO based polymer electrolyte plasticized with ionic liquid. *Solid State Ionics*, 201:1, 73-80.

Labrèche, C., Lévesque, I. and Prud'homme, J. 1996. An appraisal of tetraethylsulfamide as plasticizer for poly(ethylene oxide)−$LiN(CF_3SO_2)_2$ rubbery electrolytes, *Macromolecules*, 29, 7795–7801.

Latif, F., Aziz, M., Katun, N., & Yahya, M. Z. 2006. The role and impact of rubber in poly (methyl methacrylate)/lithium triflate electrolyte. *Journal of Power Sources*, 159:2, 1401-1404.

Lee, H. S, Yang, X. Q. McBreen, J., Xu, Z. S., Skotheim, T. A. and Okamoto, Y. 1994. Ionic conductivity of a polymer electrolyte with modified carbonate as a plasticizer for poly(ethylene oxide), *Journal of Electrochemical Society*, 141, 886−889.

Leyva-Porras, C., Cruz-Alcantar, P., Espinosa-Solís, V., Martínez-Guerra, E., Piñón-Balderrama, C. I., Compean Martínez, I. and Saavedra-Leos, M. Z. 2020. Application of differential scanning calorimetry (DSC) and modulated differential scanning calorimetry (MDSC) in food and drug industries. *Polymers*, 12:1, 5.

Li, H., Eddaoudi, M., O'Keeffe, M. and Yaghi, O. M. 1999. Design and synthesis of an exceptionally stable and highly porous metal-organic framework. *Nature*, 402, 276.

Li, J., Huang, X. and Chen, L. 2000. X-ray diffraction and vibrational spectroscopic studies on PAN-LiTFSI polymer electrolytes. *Journal of The Electrochemical Society*, 147:7, 2653.

Li, X., Cheng, F., Zhang, S. and Chen, J. 2006. Shape-controlled synthesis and lithium-storage study of metal-organic frameworks Zn_4O(1,3,5-benzenetribenzoate)$_2$. *Journal of power sources*, 160:1, 542-547.

Lightfoot, P. Mehta, M. A. and Bruce, P.G. 1993. Crystal structure of the polymer electrolyte poly(ethylene oxide)$_3$:$LiCF_3SO_3$, *Science*, 262, 883-885.

Lin, D., Liu, W., Liu, Y., Lee, H. R., Hsu, P. C., Liu, K. and Cui, Y. 2016. High ionic conductivity of composite solid polymer electrolyte via in situ synthesis of monodispersed SiO2 nanospheres in poly (ethylene oxide). *Nano letters*, 16(1), 459-465.

Livage, C., Egger, C. and Ferey, G. 2001. Hydrothermal versus nonhydrothermal synthesis for the preparation of organic−inorganic solids: the example of cobalt (II) succinate. *Chemistry of materials*, 13:2, 410-414.

Loiseau, T., Lecroq, L., Volkringer, C., Marrot, J., Férey, G., Haouas, M., Taulelle,.F., Bourrelly, S., Llewellyn, P.L. and Latroche, M. 2006. MIL-96, a porous aluminum trimesate 3D structure constructed from a hexagonal network of 18-membered rings and μ 3-oxo-centered trinuclear units. *Journal of the American Chemical Society*, 128:31, 10223-10230.

Ma, L., Abney, C. and Lin, W. 2009. Enantioselective catalysis with homochiral metal–organic frameworks. Chemical Society Reviews, 38:5, 1248-1256.

Ma, M., Zacher, D., Zhang, X., Fischer, R. A. and Metzler-Nolte, N. 2011. A method for the preparation of highly porous, nanosized crystals of isoreticular metal−organic frameworks. *Crystal Growth & Design*, 11:1, 185-189.

Marcinek, M., Zalewska, A., Żukowska, G. and Wieczorek, W. 2000. Composite electrolytes based on low molecular weight polyglycols. *Solid State Ionics*, 136, 1175-1179.

Martinez Joaristi, A., Juan-Alcañiz, J., Serra-Crespo, P., Kapteijn, F. and Gascon, J. 2012. Electrochemical synthesis of some archetypical Zn^{2+}, Cu^{2+}, and Al^{3+} metal organic frameworks. *Crystal Growth & Design*, 12:7, 3489-3498.

Marzantowicz, M., Dygas, J. R., Krok, F., Łasińska, A., Florjańczyk, Z., Zygadło-Monikowska, E. and Affek, A. 2005. Crystallization and melting of PEO: LiTFSI polymer electrolytes investigated simultaneously by impedance spectroscopy and polarizing microscopy. *Electrochimica acta*, 50:19, 3969-3977.

Mathew, D. E., Gopi, S., Kathiresan, M., Stephan, A. M. and Thomas, S. 2019. Influence of MOF ligands on the electrochemical and interfacial properties of PEO-based electrolytes for all-solid-state lithium batteries. *Electrochimica Acta*, 319, 189-200.

Matsushita, K., Shimazaki, Y., Mehta, M. A. and Fujinami, T. 2000. Synthesis and characterization of aluminate polymer electrolytes and their blends with poly(ether)s. *Solid State Ionics*, 133:3-4, 295-301.

Meyer, W. H. 1998. Polymer electrolytes for lithium-ion batteries. *Advanced materials*, 10:6, 439-448.

Mohamad, A. A., Mohamed, N. S., Yahya, M. Z. A., Othman, R., Ramesh, S., Alias, Y. and Arof, A. K. 2003. Ionic conductivity studies of poly (vinyl alcohol) alkaline solid polymer electrolyte and its use in nickel–zinc cells. *Solid State Ionics*, 156:1-2, 171-177.

Mohapatra, S. R., Thakur, A. K. and Choudhary, R. N. P. 2009. Effect of nanoscopic confinement on improvement in ion conduction and stability properties of an intercalated polymer nanocomposite electrolyte for energy storage applications. *Journal of Power Sources*, 191:2, 601-613. S

Nagajothi, A. J., Kannan, R. and Rajashabala, S. 2017. Studies on electrochemical properties of poly (ethylene oxide)-based gel polymer electrolytes with the effect of chitosan for lithium–sulfur batteries. *Polymer Bulletin*, 74:12, 4887-4897.

Nagajothi, A. J., Kannan, R. and Rajashabala, S. 2018. Preparation and characterization of PEO-based composite gel-polymer electrolytes complexed with lithium trifluoro methane sulfonate. *Materials Science-Poland*, 36:2, 185-192.

Newman, G. H., Francis, R. W., Gaines, L. H. and Rao, B. M. L. 1980. Hazard investigations of LiClO4/dioxolane electrolyte. *Journal of The Electrochemical Society*, 127:9, 2025.

Pachfule, P., Das, R., Poddar, P. and Banerjee, R. 2011. Solvothermal synthesis, structure, and properties of metal organic framework isomers derived from a partially fluorinated link. *Crystal Growth & Design*, 11:4, 1215-1222.

Paek, S. M., Yoo, E., Honma, I. 2009. Enhanced cyclic performance and lithium storage capacity of SnO_2/graphene nanoporous electrodes with three-dimensionally delaminated flexible structure. *Nano letters*, 9:1, 72-75.

Park, K. S., Ni, Z., Côté, A. P., Choi, J. Y., Huang, R., Uribe-Romo, F. J., Chae, H. K., O'Keeffe, M. and Yaghi, O. M. 2006. Exceptional chemical and thermal stability of zeolitic imidazolate frameworks. *Proceedings of the National Academy of Sciences*, 103, 10186-10191.

Pashkevich, M. 2015. Ultrafast light-induced magnetization dynamics in Co/garnet heterostructures. Doctoral dissertation, PhD dissertation, University of Bialystok, Faculty of Physics, 130, Poland.

Persi, L., Croce, F., Scrosati, B., Plichta, E. and Hendrickson, M. A. 2002. Poly (ethylene oxide)-Based, nanocomposite electrolytes as improved separators for rechargeable lithium polymer batteries: the case, *Journal of the Electrochemical Society*, 149:2, A212-A216.

Petit, C. and Bandosz, T. J. 2010. Enhanced adsorption of ammonia on metal-organic framework/graphite oxide composites: analysis of surface interactions. *Advanced Functional Materials*, 20:1, 111-118.C.

Pitawal, H. M. J. C., Dissanayake, M. A. K. L. and Seneviratne, V. A. 2007. Combined effect of Al_2O_3 nano-fillers and EC plasticizer on ionic conductivity enhancement in the solid polymer electrolyte $(PEO)_9LiTf$, *Solid State Ionics*, 178, 885-888.

Poizot, P. L. S. G., Laruelle, S., Grugeon, S., Dupont, L. and Tarascon, J. M. 2000. Nano-sized transition-metal oxides as negative-electrode materials for lithium-ion batteries. *Nature*, 407:6803, 496-499.

Polu, A. R. and Rhee, H. W. 2015. Nanocomposite solid polymer electrolytes based on poly (ethylene oxide)/POSS-PEG (n= 13.3) hybrid nanoparticles for lithium ion batteries. *Journal of Industrial and Engineering Chemistry*, 31, 323-329.

Polu, A. R. and Rhee, H. W. 2017. Ionic liquid doped PEO-based solid polymer electrolytes for lithium-ion polymer batteries. *International Journal of Hydrogen Energy*, 42:10, 7212-7219.

Prasanth, R., Shubha, N., Hng, H. H. and Srinivasan, M. 2014. Effect of poly(ethylene oxide) on ionic conductivity and electrochemical properties of poly(vinylidenefluoride) based polymer gel electrolytes prepared by electrospinning for lithium ion batteries, *Journal of Power Sources*, 245, 283-291.

Rajendran, S., Kannan, R. and Mahendran, O. 2001. Ionic conductivity studies in poly (methylmethacrylate)–polyethlene oxide hybrid polymer electrolytes with lithium salts. *Journal of Power Sources*, 96:2, 406-410.

Rajendran, S., Mahalingam, T. and Kannan, R. 2000. Experimental investigations on PAN–PEO hybrid polymer electrolytes. *Solid State Ionics*, 130:1-2, 143-148.

Ramesh, S., Yuen, T. F. and Shen, C. J. 2008. Conductivity and FTIR studies on PEO–LiX [X: CF_3SO^{3-}, SO_4^{2-}] polymer electrolytes. *Spectrochimica Acta Part A: Molecular and Biomolecular Spectroscopy*, 69:2, 670-675.

Reddy, M. J., Chu, P. P. and Rao, U. S. 2006. Study of multiple interactions in mesoporous composite PEO electrolytes. *Journal of Power Sources*, 158:1, 614-619.

Rosi, N. L., Eckert, J., Eddaoudi, M., Vodak, D. T., Kim, J., O'Keeffe, M. and Yaghi, O. M. 2003. Hydrogen storage in microporous metal-organic frameworks. *Science*, 300:5622, 1127-1129. N.L.

Rowsell, J. L., Spencer, E. C., Eckert, J., Howard, J. A. and Yaghi, O. M. 2005. Gas adsorption sites in a large-pore metal-organic framework. *Science*, 309:5739, 1350-1354.

Sabouni, R., Kazemian, H. and Rohani, S. 2010. A novel combined manufacturing technique for rapid production of IRMOF-1 using ultrasound and microwave energies. *Chemical Engineering Journal*, 165:3, 966-973.

Safarifard, V. and Morsali, A. 2015. Applications of ultrasound to the synthesis of nanoscale metal–organic coordination polymers. *Coordination Chemistry Reviews*, 292, 1-14.

Salminen, J.P., Prausnitz, J. and Newman, J. 2006. Studies of ionic liquids in lithium-ion battery test systems. *ECS Transactions*, 1:26, 107.

Saoud, K. M., Saeed, S., Al-Soubaihi, R. M. and Bertino, M. F. 2014. Microwave assisted preparation of magnesium hydroxide nano-sheets. *American Journal of Nanomaterials*, 2:2, 21-25.

Sargazi, G., Afzali, D., Ebrahimi, A. K., Badoei-dalfard, A., Malekabadi, S.and Karami, Z. 2018. Ultrasound assisted reverse micelle efficient synthesis of new Ta-MOF@ Fe3O4 core/shell nanostructures as a novel candidate for lipase immobilization. *Materials Science and Engineering: C*, 93, 768-775.

Sato, T., Maruo, T., Marukane, S. and Takagi, K. 2004. Ionic liquids containing carbonate solvent as electrolytes for lithium ion cells. *Journal of Power Sources*, 138:1-2, 253-261.

Schedy, A., Quarthal, D. and Oetken, M. 2018. Graphene–exciting insights into the synthesis and chemistry of the miracle material of the 21st century and its implementation in chemistry lessons for the first time. *World*, 6:1, 43-53.

Scrosati, B. 2005. Power sources for portable electronics and hybrid cars: lithium batteries and fuel cells. *The Chemical Record*, 5:5, 286-297.

Scrosati, B. and Vincent, C. A. 2000b. Polymer electrolytes: the key to lithium polymer batteries. *Mrs Bulletin*, 25:3, 28-30.

Scrosati, B., Croce, F., Persi, L. 2000a. Impedance spectroscopy study of peo-based nanocomposite polymer electrolytes, *Journal of The Electrochemical Society*, 14, 1718-1721

Scrosati, W. A. V. S. B. 2002. *Advances in lithium-ion batteries*. Springer Science & Business Media, Kluwer Academic/Plenum, 186, New York, USA.

Sel, K., Demirci, S., Meydan, E., Yildiz, S., Ozturk, O. F., Al-Lohedan, H. and Sahiner, N. 2015. Benign preparation of metal–organic frameworks of trimesic acid and Cu, Co or Ni for potential sensor applications. *Journal of Electronic Materials*, 44, 136-143.

Sheldon, M. H., Glasse, M. D., Latham, R. J. and Linford, R. G. 1989. The effect of plasticiser on zinc polymer electrolytes, *Solid State Ionics*, 34, 135−138.

Siegel, J. and Saukko, P. (Editors) 2013. *In Encyclopedia of Forensic Sciences* (Second Edition). Academic Press, 493, USA.

Singh, V. K., Balo, L., Gupta, H., Singh, S. K. and Singh, R. K. 2017. Solid polymer electrolytes based on Li+/ionic liquid for lithium secondary batteries. *Journal of Solid State Electrochemistry*, 21:6, 1713-1723.

Singh, V. K., Singh, R. K. 2015. Development of ion conducting polymer gel electrolyte membranes based on polymer PVdF-HFP, BMIMTFSI ionic liquid and the Li-salt with improved electrical, thermal and structural properties. *Journal of Materials Chemistry C*, 3:28, 7305-7318.

Smith, K. A. 2010. Electrochemical control of lithium-ion batteries, *IEEE Control Systems*, 30:2, 18-25.

Stassen, I., Styles, M., Van Assche, T., Campagnol, N., Fransaer, J., Denayer, J., Tan, J. C., Falcaro, P., De Vos, D. and Ameloot, R. 2015. Electrochemical film deposition of the zirconium metal–organic framework UiO-66 and application in a miniaturized sorbent trap. *Chemistry of Materials*, 27:5, 1801-1807.

Staunton, E., Andreev, Y. G. and Bruce, P. G. 2007. Factors influencing the conductivity of crystalline polymer electrolytes. *Faraday Discussions*, 134, 143-156.

Stephan, A. M. 2006. Review on gel polymer electrolytes for lithium batteries. *European polymer journal*, 42:1, 21-42.

Stephan, A. M., Kumar, T. P., Kulandainathan, M. A. and Lakshmi, N. A. (2009). Chitin-incorporated poly (ethylene oxide)-based nanocomposite electrolytes for lithium batteries. The Journal of Physical Chemistry B, 113(7), 1963-1971.

Stoeva, Z., Martin-Litas, I., Staunton, E., Andreev, Y. G. and Bruce, P. G. 2003. Ionic conductivity in the crystalline polymer electrolytes PEO_6:$LiXF_6$, X = P, As, Sb. *Journal of the American Chemical Society*, 125, 4619–4626.

Strawhecker, K. E. and Manias, E. 2003. Crystallization behavior of poly (ethylene oxide) in the presence of Na^+ montmorillonite fillers. *Chemistry of Materials*, 15:4, 844-849.

Suriyakumar, S., Kanagaraj, M., Angulakshmi, N., Kathiresan, M., Nahm, K. S., Walkowiak, M., Wasi´nski, K., P´ołrolniczak, P. and Manuel Stephan, A. 2016. Charge–discharge studies of all-solid-state Li/$LiFePO_4$ cells with PEO-based composite electrolytes encompassing metal organic frameworks. *Royal Society Chemistry Advances*, 6, 97180−97186.

Takata, K. I., Morita, M., Matsuda, Y. and Matsui, K. 1985. Cycling characteristics of secondary Li electrode in LiBF4/mixed ether electrolytes. *Journal of The Electrochemical Society*, 132:1, 126.

Tang, C., Hackenberg, K., Fu, Q., Ajayan, P. M. and Ardebili, H. 2012. High Ion Conducting Polymer Nanocomposite Electrolytes Using Hybrid Nanofillers. *Nano Letters*, 12, 1152-1156.

Tang, Z., Wang, J., Chen, Q., He, W., Shen, C., Mao, X. X. and Zhang, J. 2000. A novel PEO-based composite polymer electrolyte with absorptive glass mat for Li-ion batteries. *Electrochimica Acta*, 52:24, 6638-6643.

Tarascon, J. M., and Guyomard, D. 1994. New electrolyte compositions stable over the 0 to 5 V voltage range and compatible with the Li1+ xMn2O4/carbon Li-ion cells. *Solid State Ionics*, 69:3-4, 293-305.

Tarascon, J. M. and Armand, M. 2001. Issues and challenges facing rechargeable lithium batteries. *Nature*, 414, 359-367.

Tokur, M., Algul, H., Ozcan, S., Cetinkaya, T., Uysal, M., Guler, M. O. and Akbulut, H. 2016. Stability effect of polymer-based additives on EMITFSI-LiTFSI electrolyte in lithium-air battery. *Solid State Ionics*, 286, 51-56.

Tranchemontagne, D. J., Hunt, J. R. and Yaghi, O. M. 2008. Room temperature synthesis of metal-organic frameworks: MOF-5, MOF-74, MOF-177, MOF-199, and IRMOF-0. *Tetrahedron*, 64:36, 8553-8557.

Uchida, I. and Sato, H. 1995. Preparation of Binder-Free, thin film LiCoO2 and its electrochemical responses in a propylene carbonate solution. *Journal of the Electrochemical Society*, 142:9, L139.

Ue, M. 1994. Mobility and ionic association of lithium and quaternary ammonium salts in propylene carbonate and γ-butyrolactone. *Journal of the electrochemical society,* 141:12, 3336.

Ue, M., Takeda, M., Takehara, M., and Mori, S. 1997. Electrochemical properties of quaternary ammonium salts for electrochemical capacitors. *Journal of the Electrochemical Society,* 144:8, 2684.

Ullah Rather, S. 2014. Synthesis, characterization, and hydrogen uptake studies of magnesium nanoparticles by solution reduction method. *Materials Research Bulletin*, 60, 556-561.

Uma, T., Mahalingam, T. and Stimming, U. 2005. Solid polymer electrolytes based on poly (vinylchloride)–lithium sulfate. *Materials Chemistry and Physics*, 90:2-3, 239-244.

Vélez, J. F., Aparicio, M. and Mosa, J. 2016. Covalent silica-PEO-LiTFSI hybrid solid electrolytes via sol-gel for Li-ion battery applications. *Electrochimica Acta*, 213, 831-841.

Vu, A. T., Jiang, S., Ho, K., Lee, J. B. and Lee, C. H. 2015. Mesoporous magnesium oxide and its composites: Preparation, characterization, and removal of 2-chloroethyl ethyl sulfide. *Chemical Engineering Journal*, 269, 82-93.

Wang, W., Yi, E., Fici, A. J., Laine, R.M. and Kieffer, J. 2017. Lithium Ion Conducting Poly(ethylene oxide)-Based Solid Electrolytes Containing Active or Passive Ceramic Nanoparticles, *Journal of Physical Chemistry C,* 121, 5, 2563–2573.

Webber, A. 1991. Conductivity and viscosity of solutions of $LiCF_3SO_3$, $Li(CF_3SO_2)_2N$, and their Mixtures. *Journal of the Electrochemical Society*, 138:9, 2586.

Wen, S. J., Richardson, T. J., Ghantous, D. I., Striebel, K. A., Ross, P. N. and Cairns, E. J. 1996. FTIR characterization of PEO+ LiN $(CF_3SO_2)_2$ electrolytes. *Journal of Electroanalytical Chemistry*, 408:1-2, 113-118.

Wilson, G. J., Hollenkamp, A. F. and Pandolfo, A. G. 2007. Resolving ambiguous naming for an ionic liquid anion. *Chemistry international*, 29:4, 16.

Wright, P. V. 1976. An anomalous transition to a lower activation energy for dc electrical conduction above the glass-transition temperature. *Journal of Polymer Science: Polymer Physics Edition*, 14:5, 955-957.

Wu, A., Lu, F., Sun, P., Qiao, X., Gao, X. and Zheng, L. 2017. Low-molecular-weight supramolecular ionogel based on host–guest interaction. *Langmuir*, 33:49, 13982-13989.

Xiong, H. M., Zhao, X. and Chen, J. S. 2001. New polymer−inorganic nanocomposites: PEO−ZnO and PEO−ZnO−LiClO4 Films, *Journal of Physical Chemistry B*, 105, 10169-10174.

Xu, K. 2004. Nonaqueous liquid electrolytes for lithium-based rechargeable batteries. *Chemical Reviews*, 104:10, 4303-4418.

Xu, W., Li, G., Li, W. and Zhang, H. 2016. Facile room temperature synthesis of metal-organic frameworks from newly synthesized copper/zinc hydroxide and their application in adsorptive desulfurization. *RSC Advances*, 6:44, 37530-37534.

Yadav, D. K., Ganesan, V., Sonkar, P. K., Gupta, R. and Rastogi, P. K. 2016. Electrochemical investigation of gold nanoparticles incorporated zinc based metal-organic framework for selective recognition of nitrite and nitrobenzene. *Electrochimica Acta*, 200, 276-282.

Yaghi, O. M., Li, G. and Li, H. 1995. Selective binding and removal of guests in a microporous metal–organic framework. *Nature*, 378:6558, 703-706.

Yang, L., Kinoshita, S., Yamada, T., Kanda, S., Kitagawa, H., Tokunaga, M., Ishimoto, T., Ogura, T., Nagumo, R., Miyamoto, A. and Koyama, M. 2010. A Metal–Organic Framework as an Electrocatalyst for Ethanol Oxidation. *Angewandte Chemie*, 122, 5476-5479.

Yang, X. Q., Lee, H. S., Hanson, L., McBreen, J. and Okamoto, Y. 1995. Development of a new plasticizer for poly(ethylene oxide)-based polymer electrolyte and the investigation of their ion-pair dissociation effect, *Journal of Power Sources*, 54, 198−204.

Yoshihara, T., Tadokoro, H. and Murahashi, S. 1964. Normal vibrations of the polymer molecules of helical conformation. IV. polyethylene oxide and polyethylene-d 4 oxide. *The Journal of Chemical Physics*, 41:9, 2902-2911.

Yoshimoto, N., Shirai, T. and Morita, M. 2005. A novel polymeric gel electrolyte systems containing magnesium salt with ionic liquid. *Electrochimica Acta*, 50:19, 3866-3871.

Yuan, C., Li, J., Han, P., Lai, Y., Zhang, Z. and Liu, J. 2013. Enhanced electrochemical performance of poly (ethylene oxide) based composite polymer electrolyte by incorporation of nano-sized metal-organic framework. *Journal of Power Sources*, 240, 653-658.

Zhang, L., Wu, H. B., Madhavi, S., Hng, H. H. and Lou, X. W. 2012. Formation of Fe_2O_3 microboxes with hierarchical shell structures from metal–organic frameworks and their lithium storage properties. *Journal of the American Chemical Society*, 134:42, 17388-17391.

Zhou, J. and Fedkiw, P. S. 2004. Ionic conductivity of composite electrolytes based on oligo (ethylene oxide) and fumed oxides. *Solid State Ionics*, 166:3-4, 275-293.

BIOGRAPHY

She graduated from Ege University, Department of Leather Engineering in July 2012 year after finishing from Kocasinan Super High School in 2006 year,. Then, she got master's degrees from Dokuz Eylül University, Department of Nanoscience and Nanoengineering in January 2016 and from Ege University, Department of Leather Engineering in January 2018 year. She started her doctorate at Ondokuz Mayıs University, Institute of Graduate Studies, Department of Nanoscience and Nanotechnology, and also worked as a research assistant. She is fluent in English. Her basic interests are reading books, doing sports, listening to music, watching TV series, movies, and documentaries.

Contact detail

ORCID ID: https://orcid.org/0000-0002-7615-6402

Institutions Worked Previously

Engineer Cadet: Yateks Leather Factory (2012 Fall Semester)

Research Assistant: Ondokuz Mayıs University Institute of Science Department of Nanoscience and Nanotechnology (2016-2019)

Publications Related to Ph.D. Thesis

Articles published in international peer-reviewed journals:

1. Burgaz, E., **Erciyes, A**., Andac, M. and Andac, O. 2019. Synthesis and characterization of nano sized metal organic framework-5 (MOF-5) by using consecutive combination of ultrasound and microwave irradiation methods. *Inorganica Chimica Acta (SCI)*, 485, 118-124.

Papers presented at international scientific meetings and published in proceedings:

1. Burgaz, E., **Erciyes**, **A.**, Andac, M. and Andac, O. 2019. Electrochemical synthesis of copper based nano-sized metal organic frameworks by using different organic ligands. *Uluslararası 19 Mayıs Multidisipliner Çalışmalar Kongresi*, 17-19 Mayıs, Samsun.

2. Burgaz, E., **Erciyes**, **A.**, Andac, M. and Andac, O. 2019. Structure-property relationships of poly (etylene oxide) nanocomposite electrolytes consisting of copper-based metal organic frameworks. *Uluslararası 19 Mayıs Multidisipliner Çalışmalar Kongresi*, 17-19 Mayıs, Samsun.

3. Erciyes, A., Burgaz, E., Andac, M. and Andac, O. 2018. Preparation of polymer electrolyte films using two different types of ionic liquids. *The International Conference on Materials Science Mechanical and Automation Engineerings and Technology (IMSMATEC'18)*, April 10-12, Çesme/Izmir.

4. Erciyes, A., Burgaz, E., Andac, M. and Andac, O. 2018. Preparation and characterization of PEO based polymer electrolyte membranes containing a new ionic liquid. *The International Conference on Materials Science Mechanical and Automation Engineerings and Technology (IMSMATEC'18)*, April 10-12, Çesme/Izmir.

5. Erciyes, A., Burgaz, E., Andac, M. and Andac, O and Kendirlioglu, C. 2017. Preparation and characterization of nano-sized Mg-based metal organic frameworks by using the electrochemical method. *13th Nanoscience and Nanotechnology Conference*, 22-25 October, Antalya.

6. Erciyes, A., Burgaz, E., Andac, M. and Andac, O. 2017. Preparation and characterization of nano-sized copper based metal organic frameworks by using the electrochemical method. *3rd International Porous and Powder Materials Symposium and Exhibition (PPM 2017)*, 12-15 September, Aydın.

7. Erciyes, A., Burgaz, E., Andac, M. and Andac O. and Kendirlioglu, C. 2017. Synthesis and characterization of different types of nanosized metal organic frameworks and their applications to polymer nanocomposites. *2nd International Defense Industry Symposium*, 6-8 April, Kırıkkale.

Awards, Incentives, Scholarships

1. 3. İstanbul Uluslararası Buluş Fuarında [3rd Istanbul International Inventions Fair (ISIF'18)], Katı Polimer Elektrolit Nanokompoziti İhtiva Eden Lityum Polimer Pil adlı buluş ile ikincilik ödülü (Eylül, 2018).
2. Nano-Boyutlu Metal Organik Kafes (Nano-Boyutlu MOF) Yapıları ve İyonik Sıvı İçeren Katı Poli(Etilen Oksit) Nano-Kompozit Elektrolit Malzeme Sentezi ve Karakterizsayonu, TÜBİTAK 1001 projesi, Bursiyer: 01/05/2016-01/05/2018.
3. Katı nanokompozit elektrolit ve katı nanokompozit elektroliti ihtiva eden lityum polimer pil" An application was made to the Turkish Patent and Trademark Office on 3.09.2018. (Engin Burgaz, Müberra Andaç, Ömer Andaç, **Ayşe Erciyes**, Caner Kendirlioğlu) (PATENT)

   Application Number: TR2018/12534